Bulletin 141 2020

GENESIS AND EXPLORATION POTENTIAL FOR LATE CRETACEOUS VEINS OF THE BIG FOOT MINING DISTRICT, JEFFERSON COUNTY, MONTANA

Stanley L. Korzeb

Montana Bureau of Mines and Geology, Butte, Montana

MBMG
Montana Bureau of Mines and Geology

Cover photo: The Big Four mine, the largest producer in the district, located on State Creek road.

Bulletin 141 2020

GENESIS AND EXPLORATION POTENTIAL FOR LATE CRETACEOUS VEINS OF THE BIG FOOT MINING DISTRICT, JEFFERSON COUNTY, MONTANA

Stanley L. Korzeb

Montana Bureau of Mines and Geology, Butte, Montana

MBMG
Montana Bureau of Mines and Geology

TABLE OF CONTENTS

FIGURES

TABLES

ABSTRACT

The Big Foot veins are hosted by the Butte Granite and have characteristics of both epithermal and mesothermal veins. Age dating indicates the veins developed 73.8 ± 0.12 to 75.3 ± 0.25 Ma, about the same time aplite intruded the Butte Granite at 74.5 ± 0.6 Ma. Vein age dates indicate vein emplacement was contemporaneous with a late-stage aplite intrusion of the 74.5 ± 0.9 to 76.28 ± 0.14 Ma Butte Granite. Four types of wall-rock alteration developed during quartz vein emplacement: propylitic, carbonate, silicic–illite, and argillic–illite. Silicic–illite and argillic–illite alteration occur throughout the district, whereas propylitic and carbonate alteration occur at two and one locations, respectively. The most common alteration minerals are K–illite, illite–smectite, dickite, montmorillonite, muscovite, and schorl. The schorl occurs in the silicic–illite alteration as needles included in quartz and fracture fillings. Anomalous trace elements from the altered wall rocks and quartz veins Ag, As, Pb, Sb, and Zn are characteristic of epithermal systems, and Au, Cd, Co, Cu, Mn, and Mo are characteristic of modern back arc geothermal fields.

Cathodoluminescence revealed six quartz generations and two episodes of microbrecciation. The granite wall rock was microbrecciated during alteration. The first three quartz generations show evidence of dissolution and overgrowths and were later microbrecciated. A fourth generation of quartz stringers with sulfide minerals filled open spaces in the microbrecciated quartz. The fourth generation of quartz stringers partially replaced early quartz generations. A fifth quartz generation and sulfide mineralization crystallized simultaneously in open spaces generated by microbrecciation. A final sixth quartz generation, which is barren of sulfides, filled remaining open spaces.

The veins formed at a lithostatic pressure of 2 kb, reflecting the 7 to 8 km crystallization depth for the Butte Granite. Pressure corrected fluid inclusion homogenization temperatures range from 310º to 508ºC and average 430ºC. Some fluid inclusions revealed liquid CO_2, and others had halite daughter minerals; salinities for all 181 inclusions ranged from 0.2 to 38.1 wt% NaCl eq. There is no fluid inclusion evidence that indicates boiling, but decompression of the hydrothermal fluid took place as indicated by microbrecciation of the quartz veins and host wall rock. This caused CO_2 loss, decreasing temperatures, and increasing salinities from fluid loss.

Sulfur and oxygen isotopes indicate the veins originated from a magmatic-derived hydrothermal fluid. Sulfur isotopes have a wide range, from -0.7‰ to 16.6‰, but all the samples with the exception of one range from -0.7‰ to 5.2‰, with a single outlier at a $\delta^{34}S$ value of 16.6‰. Equilibrium temperatures calculated for sphalerite–galena $\delta^{34}S$ pairs gave a temperature range of 304.2º to 578.6ºC, which overlaps the pressure-corrected fluid inclusion temperatures. Oxygen isotopes for vein quartz range from 11.0‰ to 12.3‰, and calculated $\delta^{18}O$ compositions for the hydrothermal fluids range from 6.5‰ to 9.0‰. Calculated oxygen isotopes suggest the hydrothermal fluids originated from an I type granitoid pluton. Vein quartz $\delta^{18}O$ and sulfide mineral $\delta^{34}S$ show the hydrothermal fluids were influenced by crustal rocks assimilated into an I type granitoid pluton.

Based on the depth of formation, lithostatic pressure, fluid inclusion, and stable isotope data, the veins fit the mesothermal classification. The similarities in ages between the veins and aplite imply the veins formed from a hydrothermal system established during the time of aplite intrusion, although their relation to a porphyry system cannot be ruled out. Oxygen and sulfur isotopes suggest the hydrothermal fluids originated from a cooling felsic intrusion that assimilated crustal rocks. The hydrothermal fluids underwent periods of pressure changes between lithostatic and hydrostatic and decompression; this generated microbreccias in the vein quartz and granite host. Decompression caused temperature, salinity, and pH changes and loss of CO_2 leading to quartz dissolution and overgrowths, as well as sulfide mineralization. The veins crystallized from a high- to low-temperature, variable salinity hydrothermal fluid at a lithostatic pressure of 2 kb, similar to conditions related to deep porphyry systems.

INTRODUCTION

The Big Foot mining district is located 15 mi (24 km) north of Whitehall, and 9 mi (14.5 km) south of Boulder in Jefferson County (fig. 1). The seven mines in the district with past production are accessible from State Creek Road and are located in the Deer Lodge National Forest (fig. 2). The district covers about 30 mi^2 (48 km^2) and is located in the Late Cretaceous Boulder Batholith, near its eastern contact with the comagmatic Elkhorn Mountains volcanic field (Klepper and others, 1957).

The district was chosen for this investigation because it was not studied in detail by past investigations, it could have potential for future minerals exploration or undiscovered resources for critical elements, and the genesis of mineral resources hosted by the Butte Granite is not fully understood. Elliot and others (1993) assessed the district as having a high potential for the occurrence of undiscovered porphyry/stockwork copper–molybdenum–tungsten deposits and disseminated/stockwork gold and silver deposits at depth. Their assessment was based on data from previous published and unpublished sources and studies consisting of geologic mapping, geochemical and geophysical surveys, remote sensing, and geochronologic studies. Past mining had limited production for gold, silver, copper, lead, and zinc from narrow vein deposits.

The goal of the current investigation was to assess the future exploration potential and update and generate modern geologic data on the known mineral resources. Data generated from the geologic mapping done by Olson and others (2016) was expanded with new data sets for the known narrow vein mineral resources. From the geologic data, a genetic model of the mineral resources was determined, a geologic model constructed, the ore deposit classified, and future exploration potential assessed.

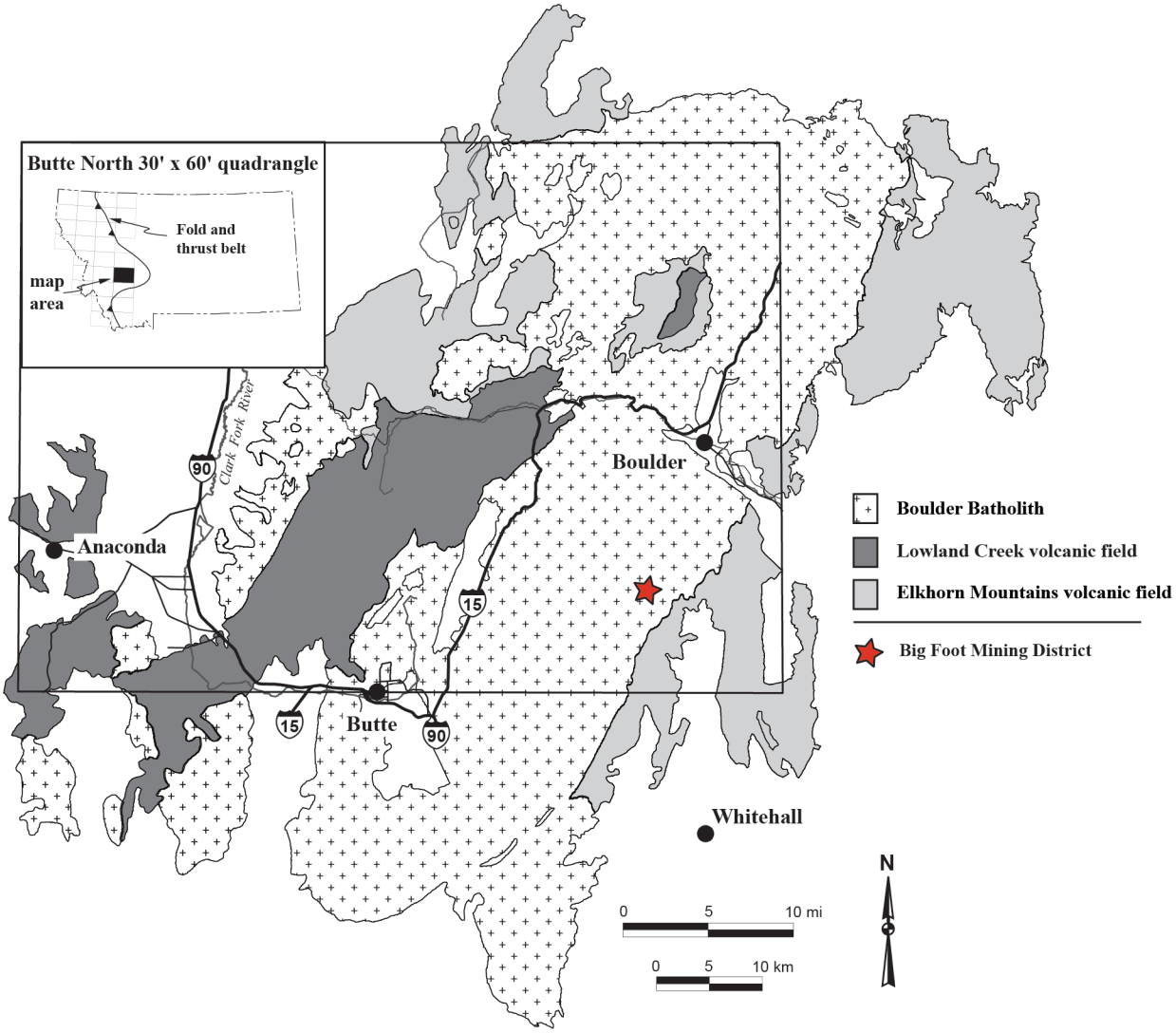

Figure 1. Generalized geologic map of the Boulder Batholith showing location of the Big Foot mining district.

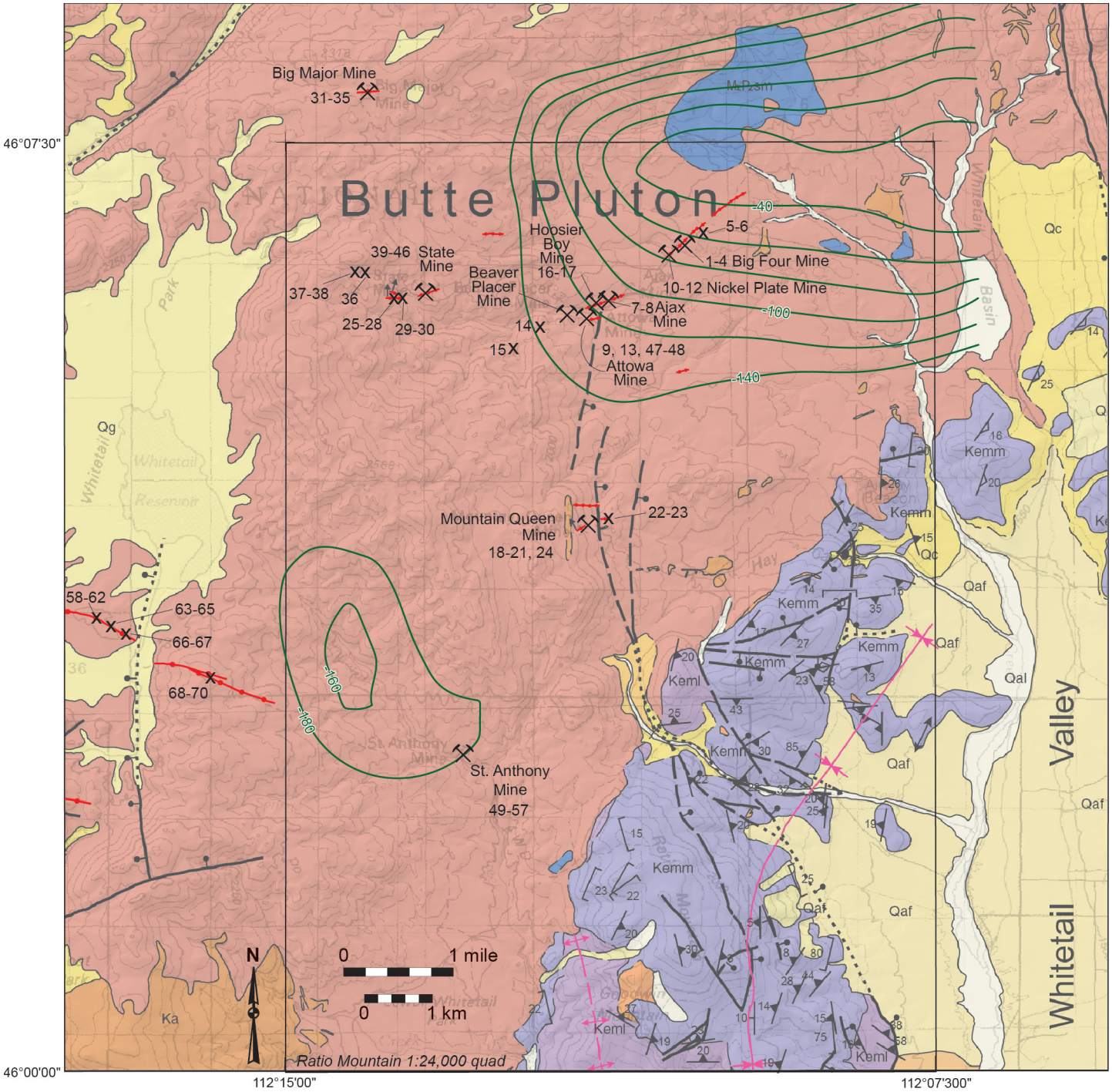

Base geologic map from Butte North 1:100,000 scale quadrangle (published as MBMG 715).

LEGEND

- Aeriomagnetic low anomaly reduced to pole (north). Contour interval -20 nt (nanoteslas). From Hanna and others (1994).
- Mine
- Prospect
- Vein

Qal	Alluvium
Qc	Colluvium
Qg	Glacial deposits
Qaf	Alluvial fan
Kemm	Rhyolite (Elkhorn Mountains Volcanic Field)
Keml	Dacite (Elkhorn Mountains Volcanic Field)
Ka	Aplite and alaskite
Kg	Granite
MzPzsm	Metamorphosed sedimentary rocks

Figure 2. Geologic map of the Big Foot mining district showing sample and major mine locations and aeromagnetic low anomalies. Box outlines Ratio Mountain 7.5' quadrangle (Olson and others, 2016).

METHODS

Methods used for this investigation involved sampling dumps and ore stockpiles of the existing mines, because underground workings were inaccessible. Vein outcrops were mapped and sampled along with associated altered host rocks. Samples were analyzed for alteration types, fluid inclusions, stable isotopes, mineralogy, trace element and whole-rock geochemistry, near infrared and shortwave infrared spectroscopy, and cathodoluminescence imaging. Minerals were identified from thin sections, polished sections, hand samples, and SEM-EDS analysis. The analytical methods used are detailed in the results sections for each analysis type.

PREVIOUS INVESTIGATIONS

The first investigation of the Big Foot mining district was a preliminary geologic map of the southwest quarter of the Boulder 7.5´ quadrangle by Pinckney and Becraft (1961). Their geologic map included the Big Foot mining district veins. Olson and others (2016) mapped the geology of the Ratio Mountain 7.5´ quadrangle covering most of the Big Foot district. Olson and others (2016) mapped the veins, included a brief discussion of the hydrothermal mineral deposits, dated the veins at the State and Ajax mines using $^{40}Ar/^{39}Ar$ methods, and determined the depth of crystallization for the Butte Granite hosting the veins.

HISTORY

Mining history of the Big Foot district is summarized from records preserved in the MBMG archives and from Roby and others (1960). The earliest recorded activity took place in the 1880s at the Mountain Queen mine (fig. 2), which was worked for a short time before being closed. The mine reopened and operated sporadically from 1939 to 1956, producing 839 tons of ore. Records for the Summit mine show development in the 1880s when a 750-ft adit was driven on an E–W-trending shear zone. There is no recorded production from the Summit mine, and it was most likely closed shortly after the adit was driven. Interest in the property was renewed in 1951 when the Defense Minerals Exploration Administration issued a loan to the owner William Mulcahy for exploration and reopening the adit. Exploration activities continued through 1967, but the property was not developed into an operating mine.

Most production from the district (table 1) was generated from the Big Four group and the State mine. The Big Four group consists of six patented claims: Hoosier Boy, Big Four, Terror, Nickel Plate, Searchlight, and Ajax (fig. 2). The Big Four group produced 1,577 tons of ore from 1920 to 1945. Production was from a 100-ft shaft on the Ajax and Hoosier claims and from a 180-ft shaft on the Big Four claim, which had three levels at 40, 60, and 100 ft depths. By 1959, the shafts were no longer accessible. The State mine (fig. 2) produced the most gold from the district. Between 1905 and 1940, a total of 544 tons of ore yielded 384 oz of gold with a calculated grade of 0.7 oz/t gold. Workings consisted of numerous adits, one above the other at about 100-ft intervals developing an east–west vein.

Lyden (2013) reports placer mining was attempted along Big Foot Creek from 1934 to 1935. For the 2-yr period of operation, 0.54 oz of gold was recovered. The sources are suggested to be gold-bearing veins located at the State mine and other prospects.

Production ended in 1956 (table 1; Roby and others, 1960). The Uranium Corporation of America leased the State mine in 1956 for a period of 10 yr. There is no recorded production or exploration activities reported for the lease period. The lease expired in 1966 with control of the State mine returning to the original owners. No new activity was reported for the State mine after 1966. After production ended, activity in the district consisted of exploration at the Mountain Queen and State mines (fig. 2). At the Mountain Queen mine, from 1963 to 1984, activity consisted of reopening and assaying samples from the underground workings, identification of ore minerals, and geologic surface mapping. Activity ended with the death of the owner in 1984 and the property has remained idle since. Exploration at the State mine consisted of trenching across known vein exposures and surface sampling and assaying vein outcrops. At the time of this investigation, there was no exploration activity taking place within the district. Some patented mining claims are being used for recreation and construction of vacation homes or cabins.

REGIONAL GEOLOGY

The mining district is located on the east side of the Boulder Batholith west of the Elkhorn Mountains volcanic field and hosted by the Butte Granite (fig. 1). The Boulder Batholith and Elkhorn Mountains volcanic field (EMVF) formed concurrently during crustal shortening between 85 and 76 Ma near the end of Mesozoic Cordillera arc magmatism (Mahoney and others, 2015; Rutland and others, 1989). During continental arc magmatism, the first magmatic event was the eruption of the EMVF, which is preserved along the

Table 1. Production history for the Big Foot mining district from Roby and others, (1960).

Year	Ore (tons)	Gold (oz)	Silver (oz)	Copper (lbs)	Lead (lbs)	Zinc (lbs)
1902–1919	No production					
1920	78	98	486	1,001		
1921	63	63	711	1,178	3,858	
1922–1923	No production					
1924	18	7	164		3,390	
1925	No production					
1926	350	55	1,257	950	27,493	11,397
1927	20	29	16			
1928	106	23	584	660	24,019	13,612
1929	619	27	3,388	2,206	126,708	91.553
1930–1931	No production					
1932	33	26	14			
1933	102	80	537	250	19,405	
1934	34	30	512	50	2,162	
1935	9	4	57			
1936	112	59	581	1,946		
1937	35	7	181	91	2,000	
1938	20	14	116	255		
1939	26	29	249	212	1,213	
1940	68	17	204	451	280	
1941	33	5	38			
1942	46	28	464		10,000	3,300
1943–1944	No production					
1945	334	11	900	400	39,500	10,200
1946	No production					
1947	123	23	348	900	9,000	1,400
1948	343	62	1,853	2,200	47,200	5,900
1949–1955	No production					
1956	37	2	202		4,600	600
1957	No production					
TOTAL	**2,609**	**699**	**12,868**	**12,750**	**320,828**	**137,962**

west and east flanks of the Boulder Batholith (fig. 1). Based on regional rock exposures, Smedes (1966) estimated the original thickness of the EMVF sequence to be 4.6 km. Diorite stocks, dikes, and sills fed the EMVF eruptions, and some diorite bodies may represent volcanic rocks recrystallized during emplacement of the Boulder Batholith (Klepper and others, 1957). Activity in the EMVF started as fissure eruptions of andesitic lava (lower member) that overflowed the edges of a broad N35°E-trending regional syncline (Klepper and others, 1957; Smedes, 1966). A middle member consisting of two massive tuff and tuff breccia units overlies the early andesite beds on the west flank of the Boulder Batholith (Scarberry and others, 2019a; Scarberry, 2016). The middle member on the east side of the batholith consists of three dacite to rhyolite ignimbrite sheets capped by two thin pyroclastic units (Scarberry and others, 2019b). Conglomerates consisting of bedded and water-laid tuff and andesite, and mudstone form the top or upper member. Lenticular beds of fresh water limestone and andesite flows occur locally (Klepper and others, 1957).

The batholith is about 90 km long and 50 km wide and elongated in a northeast–southwest direction. Plutonic rocks composing the batholith are subdivided based on age dating into an early stage and younger Butte Granite stage (Berger and others, 2011). The Boulder Batholith is an amalgamation of plutons that began forming approximately 81 Ma and continued until approximately 74 Ma (Lund and others, 2002). Houston and Dilles (2013) suggested the Boulder Batholith within the Butte mining district crystallized at a depth of 6 to 9 km based on aluminum-in-hornblende barometry studies. Based on additional aluminum-in-hornblende barometry studies, the Butte Granite within the Big Foot district is reported by Olson and others (2016) to have crystallized at a pressure of 2.1 to 2.4 kb with a depth of 7 to 8 km similar to the Butte mining district. The early stage plutonic rocks span an interval of about 81 to 76 Ma and the Butte Granite stage emplaced about 75 to 74 Ma (Lund and others, 2002). Early stage magmas were emplaced concurrently with superjacent thrust faulting and related folding. The Butte Granite was likewise

structurally controlled and follows pre-Butte Granite thrust faulting (Berger and others, 2011). Intrusions of pegmatite, alaskite, and aplite dikes mark the close of Butte Granite magmatism (Berger and others, 2011). Sulfide-bearing quartz veins with east–west orientation developed in the northern half of the batholith after crystallization of the Butte Granite and dikes (Berger and others, 2011).

A combination of Laramide shortening, Eocene crustal extension, and Basin and Range faulting caused the EMVF and Boulder Batholith to be uplifted, eroded, and exhumed. Laramide crustal shortening occurred about 65 to 55 Ma followed by extension forming a graben across the Boulder Batholith. Steepening of the subducting Farallon plate under the North American plate caused back-arc volcanism to start during the early Eocene (Feely, 2003). Back-arc volcanism caused the eruption of the Lowland Creek volcanic field into a northeast–southwest-trending half graben traversing the Boulder Batholith (Sillitoe and others, 1985; Dudás and others, 2010). Eruption of the Lowland Creek volcanic field took place between 53 and 49 Ma (Dudás and others, 2010; Scarberry and others, 2015, 2019c, 2019d; Olson and others, 2017).

DISTRICT GEOLOGY

The entire district lies within the Butte Granite of the Boulder Batholith and is included in the 1:24,000-scale Ratio Mountain geologic map generated by Olson and others (2016; figs. 2, 3). Past producing sulfide-quartz veins <4 ft wide occupy east–west- to northeast-striking fractures. The Butte Granite pluton consists of medium- to coarse-grained biotite–hornblende granite (Olson and others, 2016). Alaskite and aplite dikes and sills cutting the Butte Granite mapped by Olson and others (2016) are the youngest intrusions in the district. Ages determined from U/Pb zircons for the Butte Granite range from 74.5 ± 0.9 Ma (Lund and others, 2002) to 76.28 ± 0.14 Ma (Martin and others, 1999). Olson and others (2016) determined a $^{40}Ar/^{39}Ar$ plateau age for the vein at the State mine of 75.2 ± 0.25 Ma (95% confidence) and a $^{40}Ar/^{39}Ar$ plateau age for the vein at the Ajax mine of 73.81 ± 0.12 Ma (95% confidence). The ages of the veins are about a million years younger than the oldest age for the host Butte Granite. Lithostatic pressure estimates for the intrusion of the Butte Granite based on hornblende compositions was determined to be 2.1 to 2.4 (± 0.2) kilo bars (kb) based on the calibration of Anderson and Smith (1995) suggesting emplacement depths of 7 to 8 km (Olson and others, 2016).

GEOPHYSICS

The USGS conducted a gravity and aeromagnetic survey of the Butte 1° x 2° quadrangle that covered the Big Foot mining district (Hanna and others, 1994). The aeromagnetic survey showed a magnetic low 6 mi long and 2 mi wide in the Butte Granite in the northeast part of the district (figs. 2, 3). The magnetic low encompasses the Big Four, Nickel Plate, Ajax, and Attowa mines and a major northeast-trending vein that extends through the center of the anomaly. Another magnetic low identified by Hanna and others (1994) is west of the St Anthony mine. This magnetic low is 2 mi long and 1 mi wide. Clusters of aplite and alaskite dikes were mapped by Olson and others (2016) within and adjacent to the magnetic lows (fig. 3). Hanna and others (1994) interpret the granite-hosted magnetic low anomalies as an underlying pluton altering the Butte Granite, using the Butte district as an example. During alteration of the host granite by a porphyry intrusion, such as in the Butte district, magnetite oxidizes to hematite. The oxidation of magnetite to hematite changes the oxidation state of iron from Fe^{2+} to Fe^{3+}, giving a negative magnetic response.

INFRARED SPECTROMETRY

Visible-near infrared (VNIR) and short-wave infrared (SWIR) spectrometry were conducted on the altered host rock and sulfide–quartz veins using a PANalytical TerraSpec Halo mineral analyzer. The PANalytical TerraSpec Halo mineral analyzer measures wavelengths from 350 to 2,500 nm and is used to quantify rock alteration. The mineral analyzer identifies phyllosilicate minerals, hydroxylated silicates, sulfates, carbonates, ammonium-bearing minerals and minerals with hydroxyl (OH) bonds (Shankar, 2015; Madubuike and others, 2016), and infrared scalers based on ratios of reflectance at diagnostic wavelengths. Scalers used for this investigation are the illite spectral maturity (ISM), aluminum hydroxide bonds (Al-OH), and iron hydroxide bonds (Fe-OH). The ISM scaler is a qualitative reflection of alteration temperature. ISM numbers below 1.0 indicate high temperature, and numbers greater than 1.0 indicate low temperature (Madubuike and others, 2016). Minerals with Al-OH bonds have compositional variations that show the chemistry of fluids at the time of alteration. The compositional variations cause wavelength shifts, indicating geochemical conditions at the time of alteration. Minerals with Fe-OH bonds have compositional variations that are reflected in wavelength shifts. The wavelength position of the Fe-OH scaler is

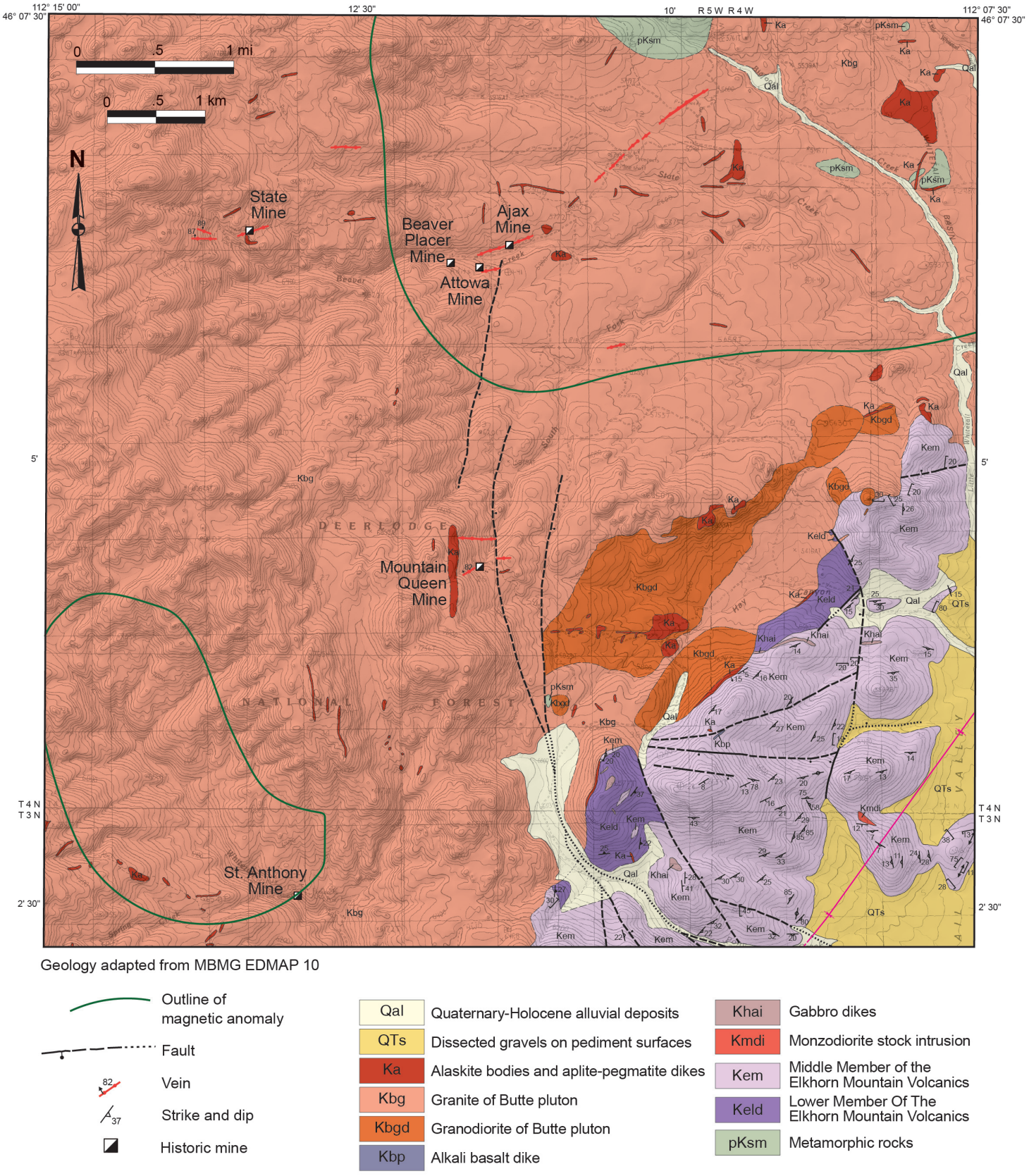

Figure 3. Geologic map modified from Olson and others (2016) of a portion of the Ratio Mountain 7.5' quadrangle EDMAP showing relationship of aplite and alaskite intrusions to area of aeromagnetic low anomaly.

a reflection of the geochemical conditions at the time of alteration.

RESULTS

Multiple infrared analysis was conducted on 42 altered granite and 28 quartz vein samples from throughout the district. Complete results are in appendices A and B. ISM values are plotted on a histogram (fig. 4) and show two alteration types related to temperature. Development of the quartz veins and silicification of the granite host develops silicic–illite alteration, with ISM scaler values varying from 0.162 to 0.976 nm, indicating high-temperature alteration (appendix B). Argillic–illite altered host rocks have ISM scaler values ranging from 1.006 nm to 3.918 nm, indicating low-temperature alteration (appendix A).

K–illite is the most common mineral identified in the altered wall-rock and quartz veins. Wavelengths from 2,196 to 2,208 nm characterize K–illite with octahedral Al contents close to muscovite (Yang and others, 2001). Phengite has longer wavelengths (>2,210) caused by substitution of Al by Mg and/or Fe (Yang and others, 2001). Yang and others (2001) report shorter wavelengths, close to 2,190, are characteristic of Na–illite. Quartz veins and silicic–illite alteration show a wide range of infrared wavelengths ranging from 2,189.2 to 2,215.2 nm (appendix B). The quartz veins and silicified granite histogram (fig. 5) shows infrared wavelengths falling between 2,196 and 2,209 nm, reflecting an abundance of K–illite. The next most abundant mineral is phengite, which is reflected in the 2,209 to 2,215 nm infrared wavelength (fig. 5). A few samples had infrared wavelengths below 2,196 nm (fig. 5), reflecting a minor presence of Na–illite. Argillic–illite altered granite has infrared wavelengths varying from 2,201.6 to 2,214.3 nm (appendix A). K–illite is the most common alteration mineral in the argillic–illite altered granite and is reflected by the distribution of infrared wavelengths of 2,200 to 2,209 nm (fig. 6). The argillic–illite histogram (fig. 6) also shows a range of 2,210 to 2,214 nm; this reflects the presence of phengite, the next most abundant alteration mineral.

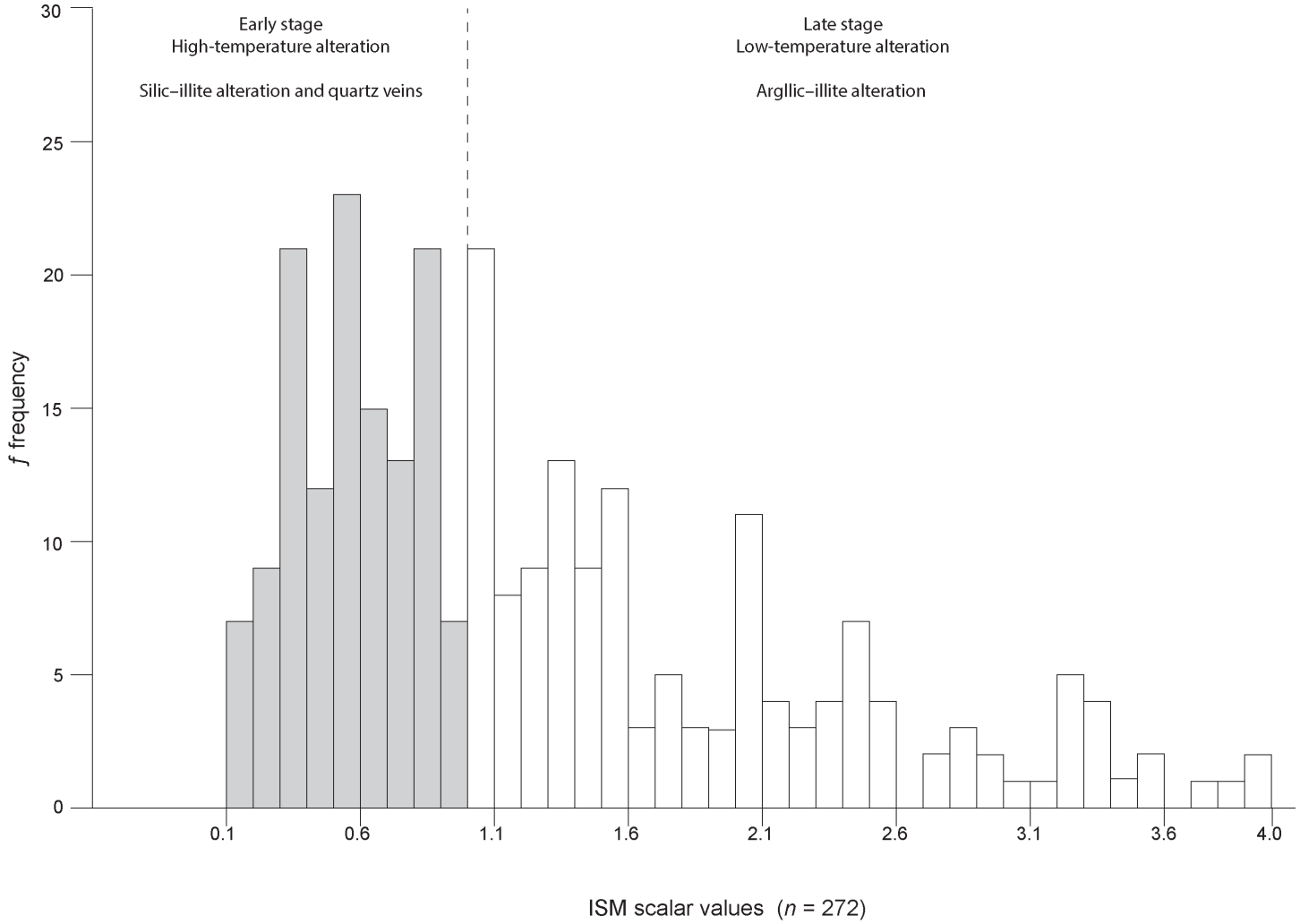

Figure 4. Histogram showing the distribution of illite spectral maturity (ISM) values indicating high temperature for silicic–illite alteration and low temperature for argillic–illite alteration.

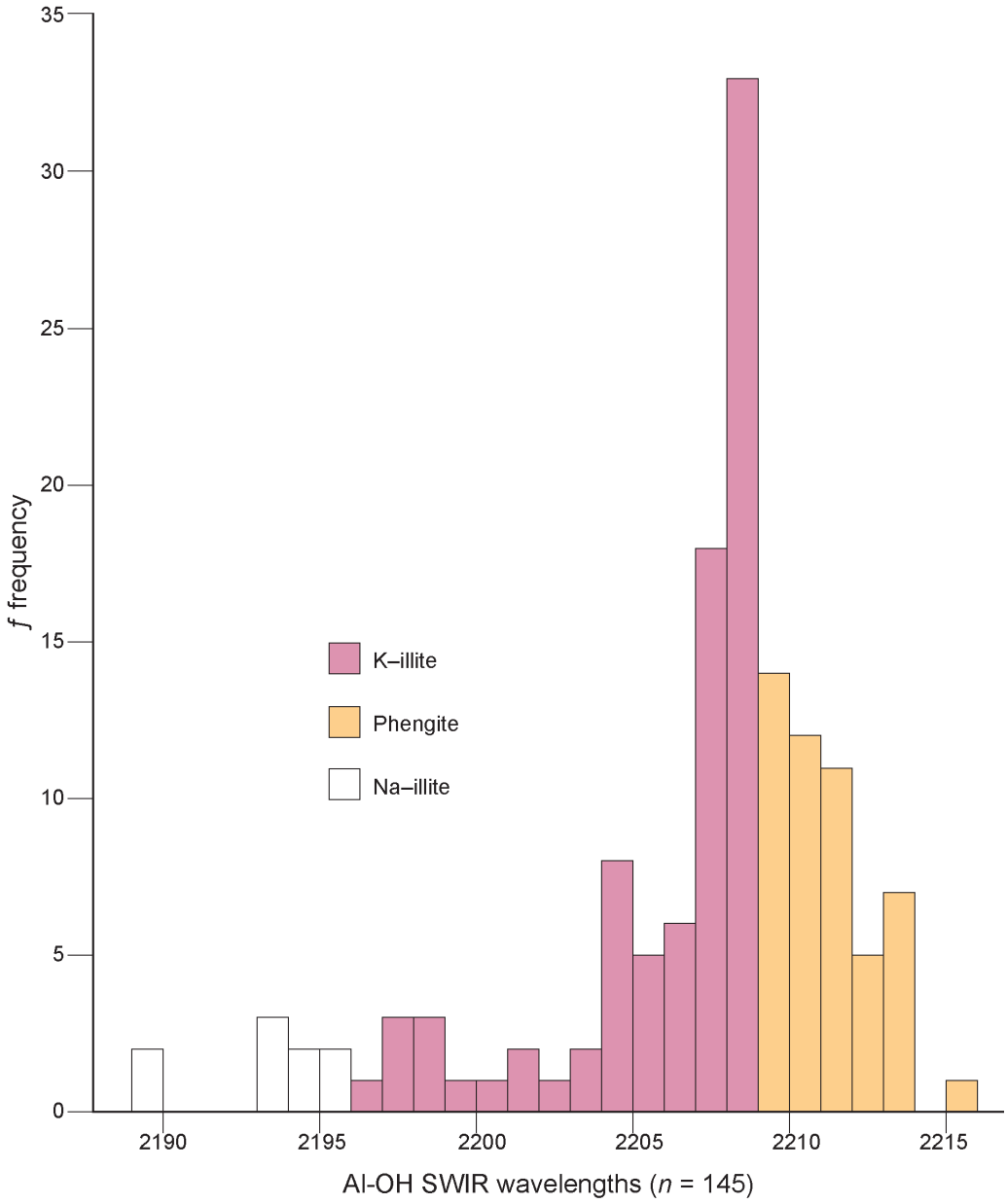

Figure 5. Histogram showing distribution of Al-OH shortwave infrared wavelengths for silicic–illite alteration.

The Fe-OH scaler has an infrared wavelength spectrum that ranges from 2,240 to 2,270 nm and is reported for minerals with Fe-OH bonds. The scaler is commonly a reflection of chlorite, annite, and phlogopite (Yang and others, 2001). The minerals usually associated with the Fe-OH scaler were rarely detected in the altered granite and quartz veins. Tourmaline (identified as schorl by SEM-EDS) was detected by infrared analysis in unaltered aplite, quartz veins, argillic–illite, and silicic–illite alteration. When detected, tourmaline yielded Fe-OH infrared wavelengths varying from 2,245.3 to 2,296.9 nm (appendices A, B). All the samples examined fall within the 2,240 to 2,270 nm infrared wavelength range reported by Yang and others (2001), with the exception of one sample that ranges from 2,296.0 to 2,296.9 nm.

WALL-ROCK ALTERATION TYPES

Hydrothermal fluids altered the Butte Granite along vein contacts. Altered wall rock extends from the vein contact into brecciated and fractured granite up to 5 ft distal from the veins. Field observations, examination of hand specimens and thin sections, and infrared spectral analysis identified propylitic, carbonate, silicic–illite, and argillic–illite alteration. Propylitic and carbonate alteration are not common but silicic–illite and argillic–illite alteration are widespread throughout the district.

Propylitic

Propylitic alteration is not common and was identified at two locations: the Big Major (sample location

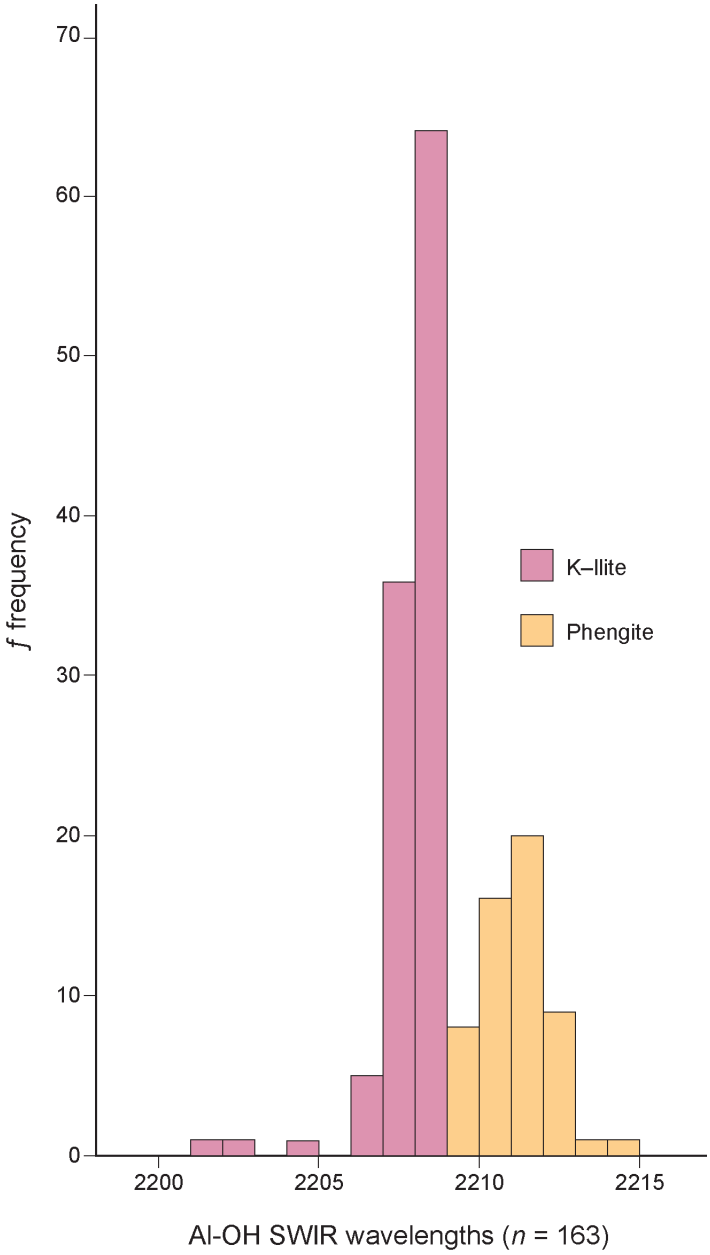

Figure 6. Histogram showing distribution for Al-OH shortwave infrared wavelengths for argillic–illite alteration.

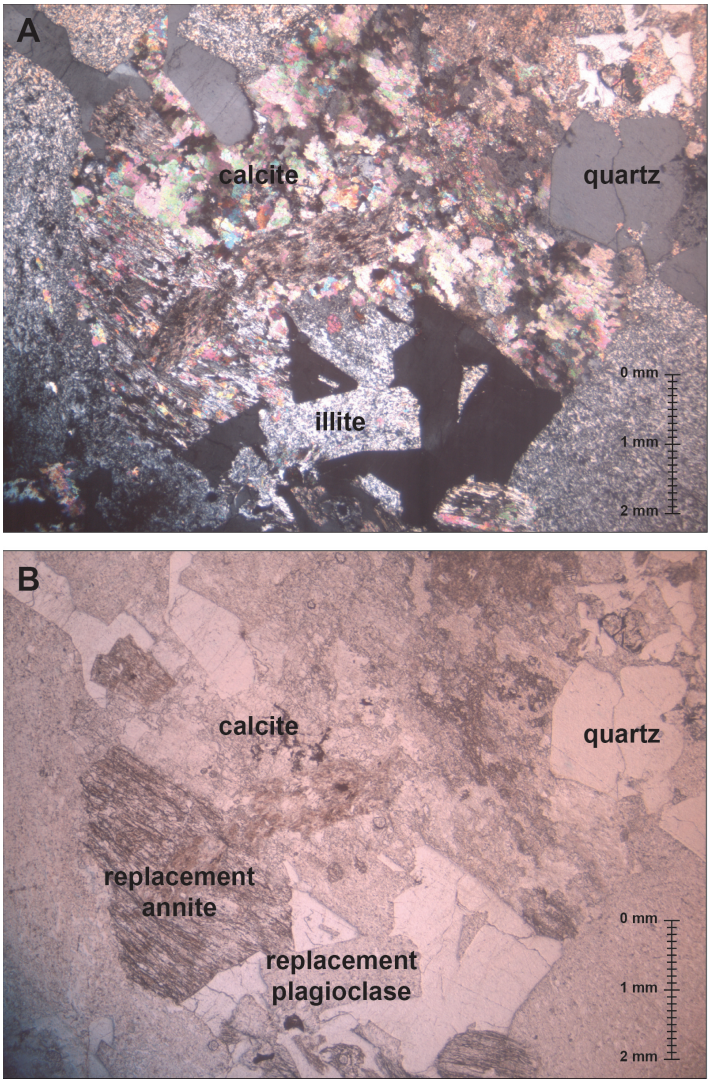

Figure 7. Propylitic alteration. Microphotograph A shows replacement of plagioclase, orthoclase, and annite with calcite, K–illite, and other clay minerals. Microphotograph B is the same image, showing remains of replaced annite and feldspars and anhedral quartz grains. Photograph A is under crossed polarizers and B is under plane-polarized light.

33) and St. Anthony mines (sample locations 49, 51, 56; fig. 2). In thin section, propylitic alteration is characterized by chlorite replacing biotite, minor epidote, and carbonate minerals, with quartz filling fractures and replacing feldspars (fig. 7). Minerals identified by VNIR-SWIR related to propylitic alteration are ankerite and dolomite. Other minerals identified by VNIR-SWIR are related to argillic–illite alteration overprinting propylitic alteration. In thin section, illite replaces plagioclase and fills fractures and open spaces with secondary quartz stringers and calcite. Schorl needles fill open spaces and are included in quartz stringers. The most common minerals related to argillic–illite alteration overprinting propylitic alteration identified by VNIR-SWIR are K–illite, muscovite, phengite (dioctahedral mica between muscovite–aluminoceladonite and muscovite–celadonite join), halloysite (kaolinite polymorph), hydrobiotite (smectite group), and rectorite (smectite group).

Carbonate

Carbonate alteration was only found at the Big Major mine (sample locations 34, 35; fig. 2). In thin section, carbonate alteration is characterized by brecciated and silicified granite with secondary quartz and calcite filling open spaces (fig. 8). Minerals identified by VNIR-SWIR are calcite, smithsonite, dolomite, K–illite, epidote, clinozoisite, muscovite, montmorillonite, kaoliniteWX (WX is well crystallized), ka-

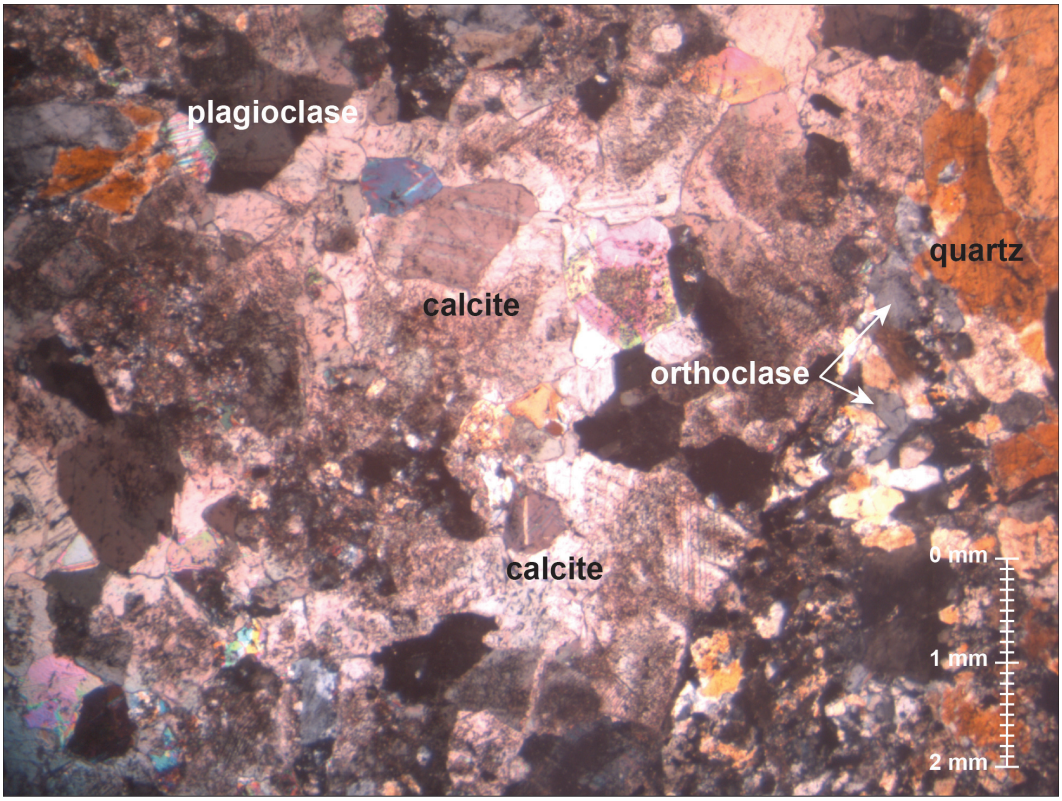

Figure 8. Carbonate alteration, microphotograph of carbonate altered granite showing calcite filling open spaces. Photo under crossed polarizers.

olinitePX (PX is poorly crystallized), and hematite. Weathering influenced the sample as indicated by the presence of hematite and poorly crystallized kaolinite. Argillic–illite alteration overprints carbonate alteration, indicated by K–illite replacing plagioclase and the presence of muscovite.

Silicic–Illite

Silicic–illite alteration is widespread throughout the district, contacting and grading into all quartz veins. Silicic–illite alteration is recognized by quartz filling open spaces and fractures in brecciated granite and replacing the granite host rock along vein margins, and complete replacement of granite breccia fragments trapped in quartz veins. In thin section, silicic–illite alteration is characterized by quartz with schorl needle inclusions, schorl filling open spaces in microbreccia and fractures, illite, and minor sulfide minerals filling fractures in brecciated granite (fig. 9). At locations where the granite is completely replaced, fractured primary anhedral quartz grains of the original granite occur as inclusions in hydrothermally deposited quartz veins. When granite is partially silicified, plagioclase is replaced by illite. Minor illite and calcite fills fractures in quartz veins. Hypogene minerals identified by VNIR-SWIR are K–illite, illite–smectite, chabazite, schorl, dickite, montmorillonite, muscovite, halloysite, and roscoelite. Secondary minerals are jarosite, goethite, vermiculite, and ferrihydrite.

Argillic–Illite

Argillic–Illite alteration is widespread throughout the district and is adjacent to all quartz veins. Abundant K–illite and other clay minerals replacing plagioclase and filling fractures in the host granite characterize argillic–illite alteration. In thin section, argillic–illite alteration shows illite partially to completely replacing feldspar crystals and annite along with clay minerals (fig. 10). Depending on the degree of alteration, primary quartz of the original granite remains in a clay–illite ground mass. Where argillic–illite alteration overprints silicic–illite alteration, fractures are filled with schorl and quartz stringers with minor sulfide minerals. The most common minerals identified by VNIR-SWIR, and found in all samples, include K–illite, illite/smectite, and phengite. Less common minerals include beidellite, palygorskite, nontronite, muscovite, dickite, kaoliniteWX (WX is well crystallized), roscoelite, rectorite, montmorillonite, magnesite, glaucophane, vermiculite, and chabazite. Secondary minerals related to weathering include ferrihydrite, jarosite, goethite, hematite, and kaolinitePX (PX is poorly crystallized).

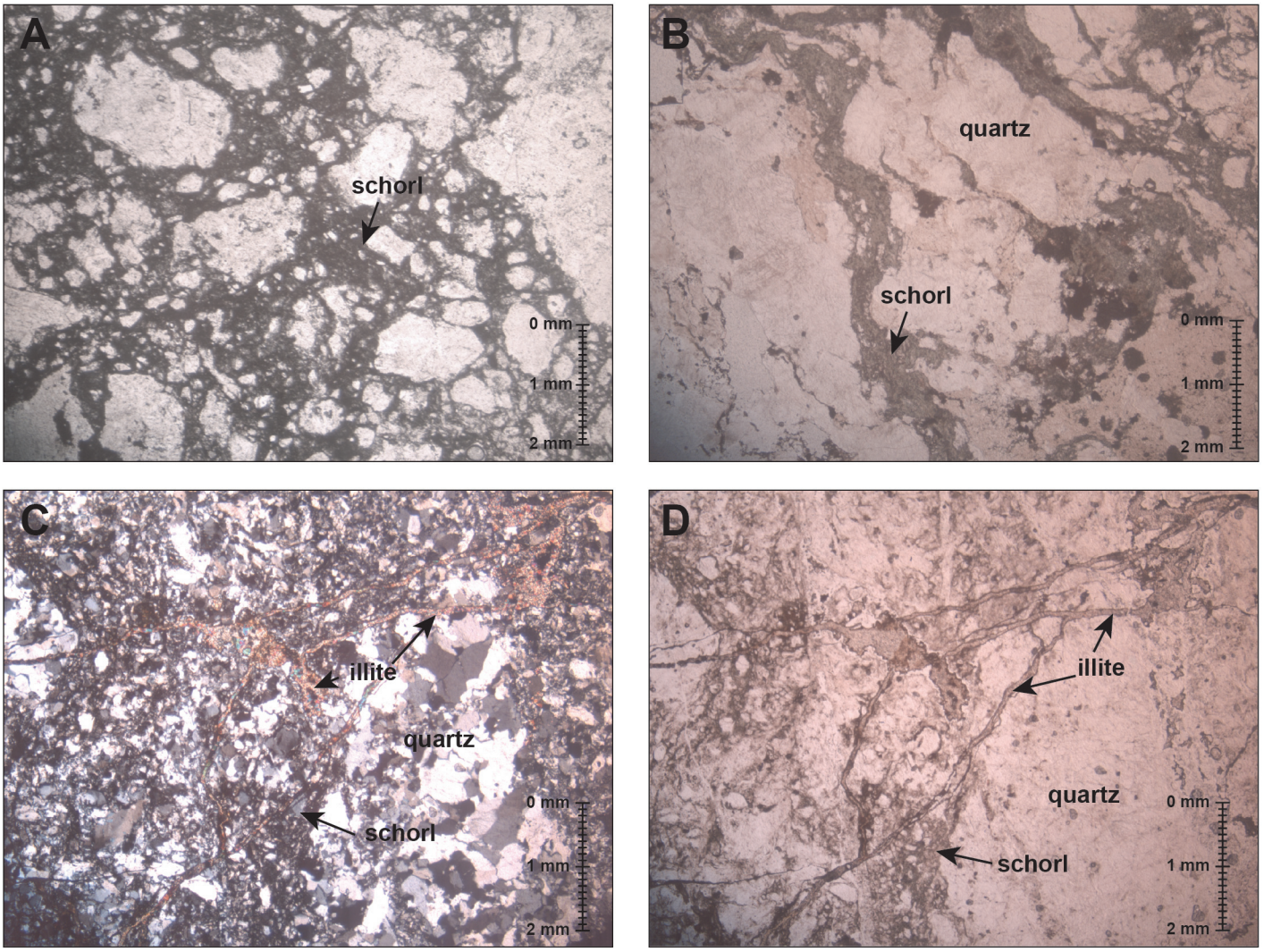

Figure 9. Silicic–illite alteration microphotographs showing microbrecciated granite with schorl filling fractures and open spaces, and replacement of granite with fine- to coarse-grained quartz. Microphotograph A shows schorl filling open spaces in brecciated and silicified granite. Microphotograph B shows schorl filling fractures in silicified granite. Microphotograph C shows replacement of host granite with fine- to coarse-grained quartz and illite filling fractures. Microphotograph D is the same image showing schorl filling open spaces in brecciated granite, coarse-grained quartz filling open spaces, and illite filling fractures. Photographs A, B, and D are under plane-polarized light and C is under crossed polarizers.

ALTERATION AND LITHO-GEOCHEMISTRY

Samples representing altered and unaltered granite were analyzed for trace elements and whole-rock oxides by ALS Minerals, Inc. Twenty samples were analyzed for 33 trace elements by four acid digestion ICP-AES and for whole-rock oxides by fusion/ICP-AES methods. ALS Minerals' procedure for whole-rock analysis consists of a lithium borate fusion prior to acid digestion followed by ICP-AES analysis. Results are given in weight percent oxide, shown in table 2. For trace element analysis, the sample is subject to a four acid digestion followed by an ICP-AES finish for 33 elements, with results reported in parts per million (ppm).

To delineate litho-geochemistry for unaltered and altered rocks, the Ishikawa alteration index (AI) and chlorite–carbonate–pyrite index (CCPI) was determined. Argillic–illite and chlorite alteration is defined by an AI between 50 and 100, with 100 representing complete replacement by sericite, illite, and/or chlorite (Large and others, 2001). The degree of chlorite alteration replacing albite, K-feldspar, and sericite is defined by the CCPI (Large and others, 2001). Large and others (2001) determined that pyrite, magnetite, or hematite enrichment, and Mg-Fe carbonate alteration have a positive effect on the CCPI. Primary composition variations of rock types and magmatic fractionation have a strong effect on the CCPI, resulting in different values for altered granite and aplite (Large and others, 2001).

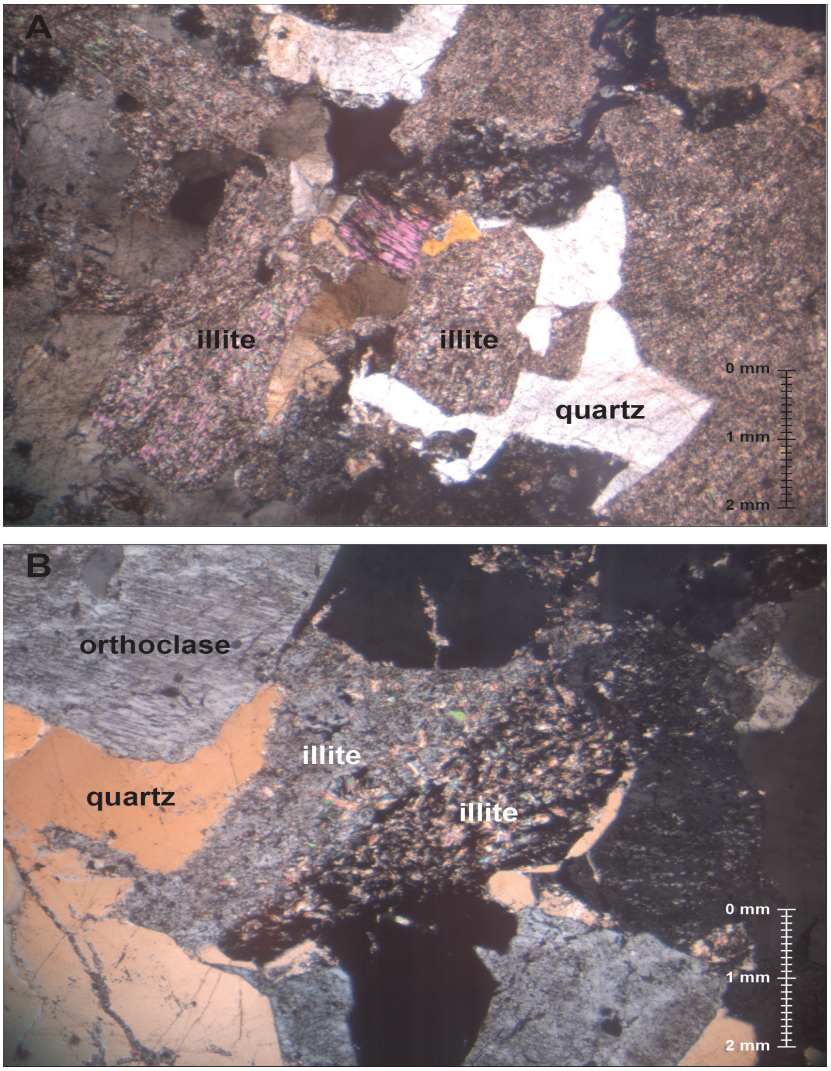

Figure 10. Argillic–illite alteration. Microphotograph A shows complete replacement of plagioclase, orthoclase, and annite with illite and other clay minerals. Microphotograph B shows partial replacement of orthoclase with illite. Both photographs are under crossed polarizers.

Table 2. Whole-rock analysis for altered and unaltered granite and aplite.

Sample No.	Alteration Type	SiO_2	Al_2O_3	Fe_2O_3	CaO	MgO	Na_2O	K_2O	TiO_2	MnO	P_2O_5
BF-3	Argillic–illite	69.2	14.59	5.47	0.26	1.04	0.36	8.54	0.58	0.08	0.15
BF-10	Silicic–illite	86.2	7.05	3.06	0.07	0.33	0.07	2.91	0.17	0.03	0.07
BF-11	Silicic–illite	78.4	13.60	2.46	0.06	0.59	0.06	5.25	0.53	0.01	0.11
BF-16	Argillic–illite	79.2	11.85	0.79	0.06	0.04	0.36	7.62	0.12	0.01	0.03
BF-22	Argillic–illite	77.5	12.80	1.97	0.06	0.31	0.12	6.72	0.50	0.01	0.08
BF-28	Aplite	77.3	12.18	1.39	0.70	0.11	2.78	5.44	0.12	0.03	0.01
BF-33	Granite	65.1	15.71	5.77	3.71	2.44	2.79	3.77	0.60	0.08	0.20
BF-33a	Propylitic	75.1	13.49	3.74	1.68	1.38	0.08	3.75	0.54	0.07	0.16
BF-34	Carbonate	73.1	2.83	1.25	22.31	0.19	0.04	0.17	0.21	0.32	0.06
BF-35	Carbonate	58.2	17.82	7.01	15.55	0.13	0.02	0.68	0.54	0.24	0.16
BF-38	Silicic–illite	97.2	1.30	1.56	0.08	0.14	0.07	0.12	0.04	0.01	0.03
BF-43	Granite	64.4	15.66	5.57	4.30	2.46	3.01	3.99	0.60	0.10	0.18
BF-44	Granite	82.0	8.58	4.07	0.48	0.61	1.90	1.63	0.36	0.11	0.12
BF-48	Argillic–illite	71.5	15.89	3.80	0.25	0.52	0.10	6.83	0.61	0.02	0.19
BF-49	Propylitic	74.4	11.08	4.66	3.31	1.73	0.30	4.22	0.35	0.13	0.12
BF-51	Propylitic	66.6	14.90	5.34	4.19	2.24	0.38	5.61	0.65	0.19	0.22
BF-56	Propylitic	62.7	13.63	7.28	7.03	3.08	0.05	5.26	0.62	0.36	0.21
BF-57	Granite	67.7	14.75	6.33	3.48	1.93	2.85	4.07	0.54	0.07	0.14
BF-62	Silicic–illite	90.4	4.85	3.62	0.09	0.82	0.33	0.06	0.05	0.02	0.02
BF-66	Silicic–illite	78.7	9.65	5.52	0.10	1.01	0.43	3.67	0.72	0.02	0.16

Note. Altered rock types are for granite host rock except sample 28, which is unaltered aplite. Analytical data normalized to 100% anhydrous but do not total 100% due to rounding. Analysis by ALS Minerals Inc. using the ALS analytical code ME-ICP 06 for whole-rock analysis.

Values for the AI and CCPI and corresponding alteration types are shown in table 3 and are plotted on an alteration box diagram (fig. 11). By plotting the CCPI against the AI, altered and unaltered granite cluster in separate fields. Silicic–illite alteration plots in two separate fields depending on degree of silicification. Argillic–illite alteration overlaps silicic–illite alteration and plots in a field on the right side of the diagram (fig. 11) near the sericite–illite edge and K-feldspar corner. The AI for silicic–illite and argillic–illite alteration varies from 67.7 to 98.0 (table 3), indicating near complete replacement of the feldspars by K–illite and phengite. Disseminated pyrite and magnetite occurs in the silicic–illite and argillic–illite altered granite and is reflected in the CCPI varying from 9.4 to 91.9 (table 3) depending on the degree of pyrite and magnetite enrichment.

Large and others (2001) noted that unaltered rocks will plot in the center of the box diagram at the location of unaltered granite (fig. 11). Aplite, having a different composition than granite, will have different CCPI values and plot in a separate field. Propylitic

Table 3. Alteration index (AI) and chlorite-carbonate pyrite index (CCPI) values with corresponding alteration types and sample numbers.

Sample Number	Rock Type	Alteration Type	AI	CCPI
BF-3	Granite	Argillic–sericitic	93.9	42.3
BF-10	Granite	Silicic–sericite	95.9	53.2
BF-11	Granite	Silicic–sericite	98.0	36.5
BF-16	Granite	Argillic–sericitic	94.8	9.4
BF-22	Granite	Argillic–sericitic	97.5	25.0
BF-28	Aplite	Unaltered	61.5	15.4
BF-33	Granite	Unaltered	48.6	55.6
BF-33a	Granite	Propylitic	74.5	57.2
BF-34	Granite	Carbonate	1.6	87.3
BF-35	Granite	Carbonate	4.9	91.1
BF-38	Granite	Silicic–sericite	63.4	90.0
BF-43	Granite	Unaltered	46.9	53.4
BF-44	Granite	Unaltered	48.5	57.0
BF-48	Granite	Argillic–sericitic	95.5	38.4
BF-49	Granite	Propylitic	62.2	58.6
BF-51	Granite	Propylitic	63.2	55.9
BF-56	Granite	Propylitic	54.1	66.1
BF-57	Granite	Unaltered	48.7	54.4
BF-62	Granite	Silicic–sericite	67.7	91.9
BF-66	Granite	Silicic–sericite	89.8	61.4

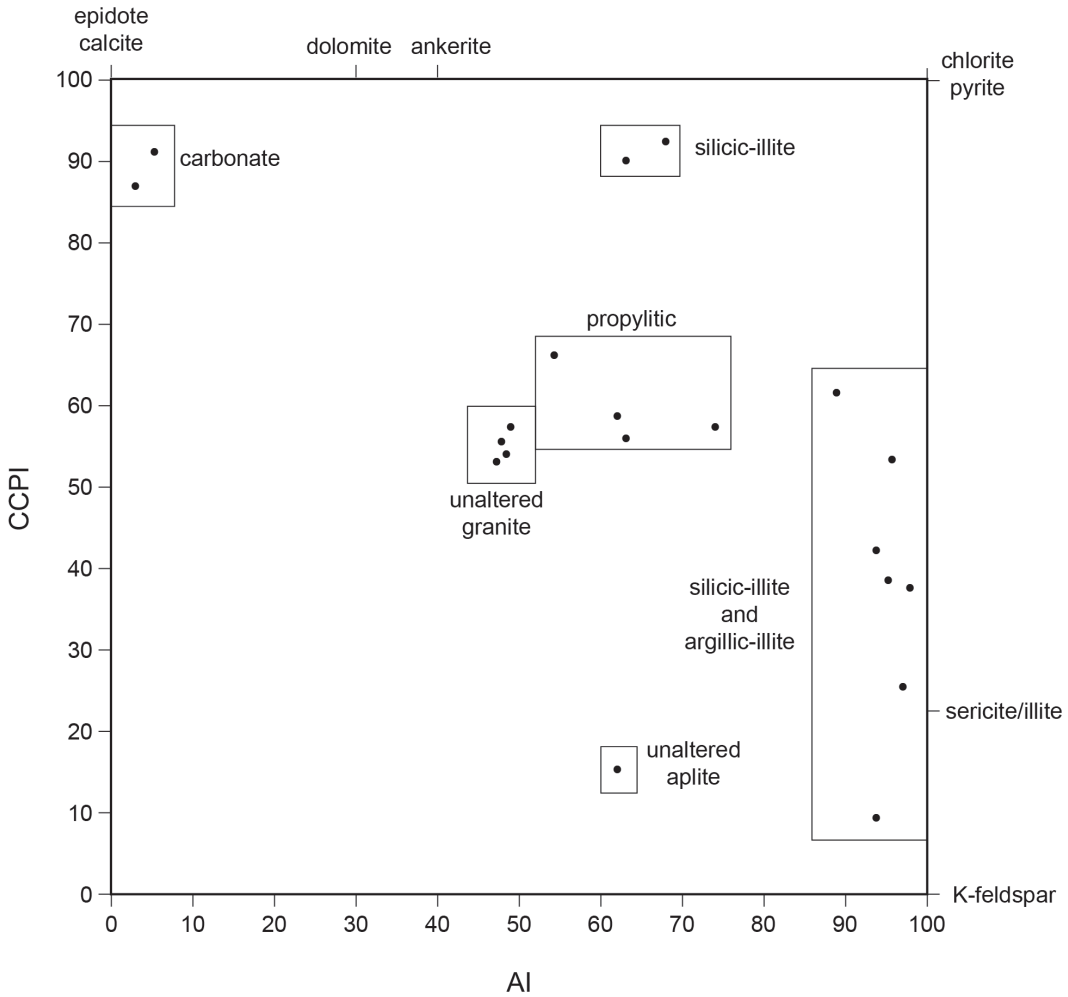

Figure 11. Alteration box diagram identifying and comparing different alteration types and corresponding alteration index (AI) and carbonate–chlorite–pyrite index (CCPI).

alteration plots adjacent to the granite field and has an AI ranging from 54.1 to 74.5 and CCPI ranging from 55.9 to 66.1. Propylitic alteration was weak, indicated by the propylitic field plotting near the center of the diagram and adjacent to the granite field (fig. 11). The wide range of AI values or propylitic alteration reflects overprinting of argillic–illite alteration.

Two silicic–illite altered samples, having SiO_2 >90 wt% and showing near complete replacement of the granite host by quartz, plot in a separate field near the top of the diagram. Due to the strong silicification, these samples lack K–illite and sericite, causing them to plot in a separate field between carbonate and chlorite–pyrite alteration. The CCPI reflects abundant disseminated pyrite that is often included within silicified host rocks. Carbonate alteration plots near the epidote–calcite corner, reflecting the abundant carbonate minerals within this alteration type.

Gains or losses of whole-rock oxide concentrations (table 2) caused by alteration of the host granite are plotted on an isocon diagram (fig. 12). The reference isocon was defined using TiO_2, SiO_2, and P_2O_5, given in tables 4–7 and plotted on an isocon diagram (fig. 12), which have little gains or losses between unaltered granite and propylitic alteration. Aluminum oxide has minor gains or losses between unaltered granite (UA), propylitic (PR), and agillic–illite (AI) alteration (tables 4, 5). The oxides defining the isocon reference line are nearly immobile, indicated by the C_{PR}/C_{UA} and C_{AI}/C_{UA} (slope of the isocon) being close to or equal to 1 and the $\Delta C/C_{UA}$ (gain or loss of oxide) having values equal to or approaching 0 (Grant, 2005). Kuwatani and others (2020) determined that an isocon slope equal to one and ΔC equal to zero define an immobile element and a reference isocon. Whole-rock oxides for silicic–illite and carbonate alteration have wide variations in gains and losses compared to unaltered granite and cannot be used to define a reference isocon for immobile oxides (tables 6, 7). Isocon analysis methods from Grant (2005) and Kuwatani and others (2020) were used to determine the isocon reference line on figure 12 and determine the gains and losses of whole-rock oxides. Analytical values too small to reasonably fit the isocon diagram were scaled up (tables 4–7).

The $\Delta C/C_{UA}$ and ΔC values for propylitic alteration oxides have both positive and negative numbers, indicating both losses and gains (table 4). The oxides used to define the reference isocon TiO_2 and P_2O_5 have $\Delta C/C_{UA}$ and ΔC values equal to 0.0, indicating they were immobile, and SiO_2 has a $\Delta C/C_{UA}$ value equal to -0.01, indicating a minor loss and minor mobility (table 4). The oxide with the greatest loss compared to unaltered granite was Na_2O, with a $\Delta C/C_{UA}$ value equal to -0.92 and ΔC value equal to -2.4 (table 4). On the isocon diagram (fig. 12), oxides with positive values plot above the isocon reference line and those with negative numbers plot below the isocon. For propylitic alteration, most oxides plot near or on the isocon reference line, indicating minor oxide enrichments or depletions compared to the other alteration types. The minor oxide gains and losses indicate minor mobilization of these oxides when the granite was propyliticly altered. The oxide with the most loss is Na_2O, which plots well below the isocon and has the same $\Delta C/C_{UA}$ value as argillic–illite alteration.

Argillic–illite alteration $\Delta C/C_{UA}$ and ΔC values for SiO_2, Al_2O_3, and K_2O are positive numbers (table 5) and plot above the isocon reference line (fig. 12). The $\Delta C/C_{UA}$ value for Al_2O_3 (0.01) approaches 0, indicating a minor gain compared to unaltered granite and minor mobility, and was used to further define the isocon reference line on figure 12. The rest of the oxides all have negative $\Delta C/C_{UA}$ and ΔC values and plot below the isocon (fig. 12), indicating a high degree of loss compared to unaltered granite. Compared to propylitic alteration, argillic–illite alteration whole-rock oxides have higher gains and losses, indicated by higher negative and positive $\Delta C/C_{UA}$ and ΔC values (tables 4, 5). The positive $\Delta C/C_{UA}$ value for K_2O could be related to the presence of illite and phengite in the argillic–illite altered granite. The positive $\Delta C/C_{UA}$ value for SiO_2 could be attributed to minor silicification of the argillic–illite altered granite. The rest of the oxides with negative $\Delta C/C_{UA}$ values (table 5) indicate they were lost during alteration and overprinting of propylitic alteration.

Silicic–illite alteration $\Delta C/C_{UA}$ and ΔC values for SiO_2 make it the only whole-rock oxide with a positive number (table 6) and that plots above the isocon (fig. 12). The high positive ΔC value could indicate SiO_2 (table 6) was mobilized from the hydrothermal fluids into the silicic–illite altered granite. The rest of the whole-rock oxides have negative $\Delta C/C_{UA}$ and ΔC values (table 6) and plot below the isocon (fig. 12), indicating a loss for these oxides compared to the host granite. Compared to propylitic and argillic–illite alteration, silcic–illite alteration has the highest losses in Al_2O_3, K_2O, and CaO, indicated by high negative $\Delta C/C_{UA}$ and ΔC values (table 6), reflecting a high degree of mobilization. Other whole-rock oxides TiO_2, P_2O_5, Fe_2O_3, MgO, MnO, and Na_2O have losses (table 6) compared to unaltered host granite.

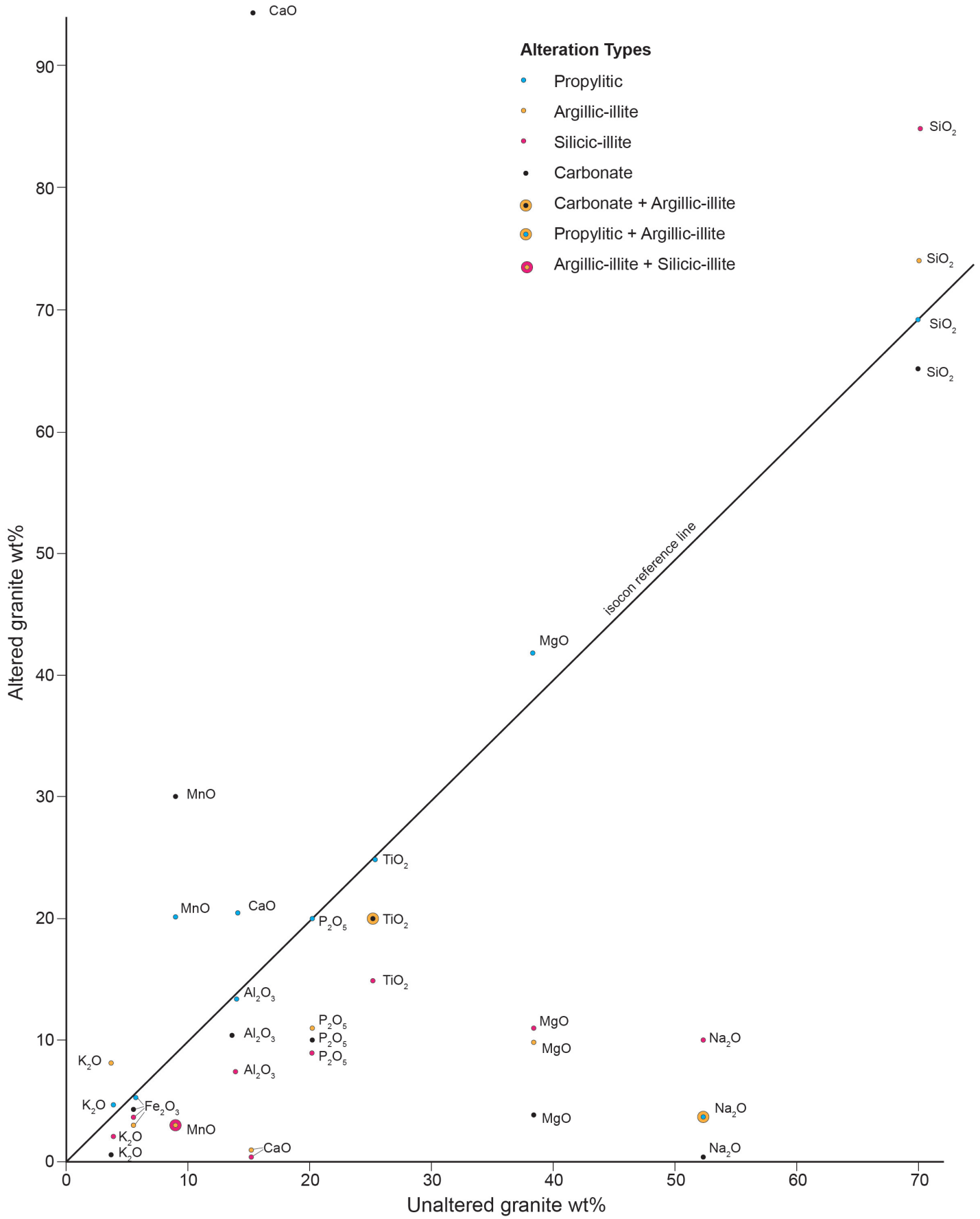

Figure 12. Isocon diagram of whole-rock oxides for propylitic, argillic–illite, silicic–illite, and carbonate alteration showing oxide losses (plotting below reference line) and gains (plotting above reference line) compared to the unaltered granite isocon reference line.

Table 4. Isocon analysis of whole-rock averages in weight percent for propylitic alteration.

Oxide	C_{UA}	C_{PR}	C_{PR}/C_{UA}	$\Delta C/C_{UA}$	ΔC	Scale	C_{UA} Scaled	C_{PR} Scaled
SiO_2	69.8	69.7	0.99	-0.01	-0.1			
Al_2O_3	13.7	13.3	0.97	-0.03	-0.4			
Fe_2O_3	5.4	5.3	0.98	-0.02	-0.1			
CaO	3.0	4.1	1.37	0.37	1.1	5	15	20.5
MgO	1.9	2.1	1.11	0.11	0.2	20	38	42
Na_2O	2.6	0.2	0.08	-0.92	-2.4	20	52	4
K_2O	3.4	4.7	1.38	0.38	1.31			
TiO_2	0.5	0.5	1.0	0.0	0.0	50	25	25
MnO	0.09	0.2	2.22	1.22	0.11	100	9	20
P_2O_5	0.2	0.2	1.0	0.0	0.0	100	20	20

Note. C_{UA}, component averages for unaltered granite; C_{PR}, component averages for propylitic alteration; C_{PR}/C_{UA}, slope of data points defining isocon; $\Delta C/C_{UA}$, gain or loss of oxides compared to unaltered granite: negative numbers indicate a loss, positive numbers indicate a gain; ΔC, gain or loss of oxides in wt%; scale, factor used to scale up whole-rock data to fit isocon plot; C_{UA} scaled, scaled components for unaltered granite; C_{PR} scaled, scaled components for propylitic alteration.

Table 5. Isocon analysis of whole-rock averages in weight percent for argillic–illite alteration.

Oxide	C_{UA}	C_{AI}	C_{AI}/C_{UA}	$\Delta C/C_{UA}$	ΔC	Scale	C_{UA} Scaled	C_{AI} Scaled
SiO_2	69.8	74.4	1.07	0.07	4.6			
Al_2O_3	13.7	13.8	1.01	0.01	0.1			
Fe_2O_3	5.4	3.0	0.56	-0.44	-2.4			
CaO	3.0	0.2	0.06	-0.94	-2.8	5	15	1
MgO	1.9	0.5	0.26	-0.74	-1.4	20	28	10
Na_2O	2.6	0.2	0.08	-0.92	-2.4	20	52	4
K_2O	3.4	7.4	2.18	1.18	4.0			
TiO_2	0.5	0.4	0.80	-0.2	-0.1	50	25	20
MnO	0.09	0.03	0.33	-0.67	-0.06	100	9	3
P_2O_5	0.2	0.11	0.55	-0.45	-0.09	100	20	11

Note. C_{UA}, component averages for unaltered granite; C_{AI}, component averages for argillic–illite alteration; C_{AI}/C_{UA}, slope of data points defining isocon; $\Delta C/C_{UA}$, gain or loss of oxides compared to unaltered granite: negative numbers indicate a loss, positive numbers indicate a gain; ΔC, gain or loss of oxides in wt %; scale, factor used to scale up whole-rock data to fit isocon plot; C_{UA} scaled, scaled components for unaltered granite; C_{AI} scaled, scaled components for argillic–illite alteration.

Table 6. Isocon analysis of whole-rock averages in weight percent for silicic–illite alteration.

Oxide	C_{UA}	C_{SI}	C_{SI}/C_{UA}	$\Delta C/C_{UA}$	ΔC	Scale	C_{UA} Scaled	C_{SI} Scaled
SiO_2	69.8	85.5	1.23	0.23	15.7			
Al_2O_3	13.7	7.5	0.54	-0.46	-6.2			
Fe_2O_3	5.4	3.38	0.62	-0.38	-2.05			
CaO	3.0	0.2	0.07	-0.93	-2.80	5	15	1
MgO	1.9	0.6	0.32	-0.68	-1.3	20	28	12
Na_2O	2.6	0.5	0.19	-0.81	-2.1	20	52	10
K_2O	3.4	2.3	0.68	-0.32	-1.07			
TiO_2	0.5	0.3	0.57	-0.43	-0.23	50	25	15
MnO	0.09	0.03	0.33	-0.67	-0.06	100	9	3
P_2O_5	0.2	0.09	0.45	-0.55	-0.11	100	20	9

Note. C_{UA}, component averages for unaltered granite; C_{SI}, component averages for silicic–illite alteration; C_{SI}/C_{UA}, slope of data points defining isocon; $\Delta C/C_{UA}$, gain or loss of oxides compared to unaltered granite: negative numbers indicate a loss, positive numbers indicate a gain; ΔC, gain or loss of oxides in wt%; scale, factor used to scale up whole-rock data to fit isocon plot; C_{UA} scaled, scaled components for unaltered granite; C_{SI} scaled, scaled components for silicic–illite alteration.

Table 7. Isocon analysis of whole-rock averages in weight percent for carbonate alteration.

Oxide	C_{UA}	C_{CA}	C_{CA}/C_{UA}	$\Delta C/C_{UA}$	ΔC	Scale	C_{UA} Scaled	C_{CA} Scaled
SiO_2	69.8	65.7	0.94	-0.06	-4.1			
Al_2O_3	13.7	10.3	0.75	-0.25	-3.4			
Fe_2O_3	5.4	4.13	0.76	-0.24	-1.3			
CaO	3.0	18.9	6.3	5.3	15.9	5	15	94.5
MgO	1.9	0.2	0.11	-0.89	-1.88	20	38	4
Na_2O	2.6	0.03	0.01	-0.99	-2.57	20	52	0.6
K_2O	3.4	0.4	0.12	-0.88	-2.97			
TiO_2	0.5	0.4	0.75	-0.25	-0.13	50	25	20
MnO	0.09	0.3	3.33	2.33	0.21	100	9	30
P_2O_5	0.2	0.1	0.5	-0.5	-0.1	100	20	10

Note. C_{UA}, component averages for unaltered granite; C_{CA}, component averages for carbonate alteration; C_{CA}/C_{UA}, slope of data points defining isocon; $\Delta C/C_{UA}$, gain or loss of oxides compared to unaltered granite: negative numbers indicate a loss, positive numbers indicate a gain; ΔC, gain or loss of oxides in wt%; scale, factor used to scale up whole-rock data to fit isocon plot; C_{UA} scaled, scaled components for unaltered granite; C_{CA} scaled, scaled components for carbonate alteration.

Carbonate alteration has two whole-rock oxides, CaO and MnO, with positive $\Delta C/C_{UA}$ and ΔC values (table 7) and that plot above the isocon reference line (fig. 12). The positive $\Delta C/C_{UA}$ and ΔC values for CaO and MnO are a reflection of the abundant calcite that characterizes carbonate alteration. The rest of the whole-rock oxides have negative $\Delta C/C_{UA}$ and ΔC values (table 7) and plot below the isocon reference line (fig. 12). Compared to all the alteration types, carbonate alteration has the highest losses for K_2O, MgO, Na_2O, and SiO_2, indicated by high negative $\Delta C/C_{UA}$ and ΔC values. Carbonate alteration caused the greatest mobilization of K_2O, MgO, Na_2O, and SiO_2 compared to unaltered granite and the other alteration types. The whole-rock oxides TiO_2, P_2O_5, Fe_2O_3, and Al_2O_3 have greater losses than argillic–illite alteration and lower losses than silicic–illite alteration (fig. 12), indicating a high degree of oxide mobilization during carbonate alteration.

Alteration Trace Elements

Epithermal vein systems and modern hot springs have unique trace element assemblages and geochemical signatures (Mosier and others, 1987; Silberman and Berger, 1985; Simmons and Browne, 2000). Thirty-three trace elements were determined by ICP-AES methods by ALS Minerals for 20 samples representing four alteration types and unaltered granite host rock (table 8; complete data set is shown in appendix C). Trace elements known to be characteristic of epithermal vein systems, modern hot springs, and other elements consistently above instrument detection limits were selected from the total set and are shown in table 8. Unaltered granite compared to altered rock analysis determined gains or losses of trace elements. Epithermal and deeper vein systems, either directly or indirectly related to porphyry type mineralization, share the same characteristic trace elements (Halley and others, 2015). The techniques used for evaluating trace elements for epithermal veins can therefore be applied to porphyry type mineralization.

The degree of gain or loss of trace elements for the four alteration types compared to unaltered granite are shown in an isocon plot (fig. 13) and in tables 9–12. Isocon analysis methods defined by Grant (2005) and Kuwatani and others (2020) determined the isocon reference line in figure 13. The isocon reference line was defined using Sc and Cr. These have C_{PR}/C_{UA} (slope of the isocon) values of 1.02 and 1.04, respectively, which approaches 1, indicating a minor gain between unaltered granite and propylitic alteration. The $\Delta C/C_{UA}$ (gain or loss) approaches 0 (table 9), indicating minor Sc and Cr mobility between propylitic alteration and unaltered granite. Analytical values too large to reasonably fit on the isocon diagram were scaled down.

Trace elements for propylitic alteration have both gains and losses compared to unaltered granite (table 9). Elements with gains plot above the isocon reference line and those with losses plot below the line (fig. 13). The trace elements Cd, Cu, Mn, Pb, Sb, and Zn have the highest positive $\Delta C/C_{UA}$ and ΔC values compared to the other elements (table 9) and plot well above the reference isocon (fig. 13). The high $\Delta C/C_{UA}$ and ΔC values indicate these elements had a high degree of enrichment when propylitic alteration developed. The other elements with positive $\Delta C/C_{UA}$ and ΔC values Ag and As, were also gained during propylitic alteration and plot above the isocon reference line (fig. 13). Trace elements were also lost from the

Table 8. Trace element averages for unaltered granite and corresponding argillic–illite, silicic–illite, propylitic, and carbonate alteration.

Element	Granite	*n*	Argillic–Illite	*n*	Silicic–Illite	*n*	Propylitic	*n*	Carbonate	*n*
Ag	2.6	1	12.5	4	37.7	5	4.5	3	<0.5	2
As	20	4	1,256	4	5,093.4	5	32	4	27	1
Ba	615	4	732.5	4	168	5	377.5	4	25	2
Bi	<2	4	2	1	25.5	4	3	1	8	2
Cd	1.7	1	44.8	4	139.7	4	40.6	3	<0.5	2
Co	16.5	4	6.3	4	4	5	11.25	4	2	1
Cr	22.3	4	18.3	4	21.8	5	23.3	4	17	2
Cu	44.5	4	172	4	439	5	273	4	29	2
Ga	17.5	4	15	4	10	5	12.5	4	30	1
Mn	688	4	230.5	4	138.2	5	1,310	4	1,872.5	2
Mo	5.5	4	4	4	13.8	5	4.8	4	1	1
Pb	94.3	4	8,940.3	4	9,688	5	1,053.5	4	29.5	2
Sb	6.5	2	25.3	4	65.8	5	30.3	4	78	1
Sc	9.8	4	7.8	4	7.2	5	10	4	5.5	2
Sr	383.5	4	122.5	4	53.6	5	125.3	4	1,207.5	2
V	88.8	4	73.5	4	65	5	79	4	77	2
Zn	64.8	4	1,020.3	4	6,888.2	5	1,582	4	13	2

Note. Values are in parts per million; *n*, number of samples used in averages; samples below detection limits were not used in calculations. Complete analytical results are in appendix C.

unaltered granite during propylitic alteration and have negative $\Delta C/C_{UA}$ and ΔC values and plot below the isocon reference line (fig. 13). The elements Ba and Sr had the greatest losses with the highest negative $\Delta C/C_{UA}$ and ΔC values, followed by V, Co, Ga, and Mo; all of these elements were depleted compared to unaltered granite when propylitic alteration took place.

Trace elements for argillic–illite alteration have both gains and losses compared to unaltered granite (table 10). The trace elements with the highest positive $\Delta C/C_{UA}$ and ΔC values, As, Cd, Pb, and Zn (table 10), indicate the greatest gains compared to unaltered granite and the other elements. The other elements with positive $\Delta C/C_{UA}$ and ΔC values, Ag, Ba, Cu, and Sb, have major gains compared to unaltered granite. All the trace elements with positive $\Delta C/C_{UA}$ and ΔC values mobilized from hydrothermal fluids into the argillic–illite altered granite. Trace elements with negative $\Delta C/C_{UA}$ and ΔC values, Co, Cr, Ga, Mn, Mo, Sc, Sr, and V, were lost and depleted compared to unaltered granite during argillic–illite alteration. Compared to propylitic alteration, these elements have a greater loss except for Ga, which has a slight gain over propylitic alteration (fig. 13).

Silicic–illite alteration has the greatest gains and losses for trace elements compared to the other alteration types and unaltered granite (table 11, fig. 13). The trace elements with highest positive $\Delta C/C_{UA}$ and ΔC values are As, Cu, Pb, and Zn (table 11). This indicates these elements had the highest gains and were the most concentrated during silicic–illite alteration. Other elements Ag, Cd, Mo, and Sb have positive $\Delta C/C_{UA}$ and ΔC values, indicating concentration gains compared to unaltered granite and a high degree of mobility from the hydrothermal fluids during silicic–illite alteration. Compared to the other alteration types, silicic–illite alteration has the highest gains for Ag, As, Cd, Cu, Mo, Pb, Sb, and Zn; these plot well above the isocon reference line (fig. 13). Trace elements lost during silicic–illite alteration are Ba, Co, Cr, Ga, Mn, Sc, Sr, and V, indicated by negative $\Delta C/C_{UA}$ and ΔC values (table 11), and are depleted compared to unaltered host granite.

Compared to unaltered granite, carbonate alteration has gains of As, Ga, Mn, Sb, and Sr, indicated by positive $\Delta C/C_{UA}$ and ΔC values (table 12). Of all the trace elements, Mn had the greatest gain with a ΔC value of 1,184.5 ppm, reflecting the precipitation of carbonate minerals. The trace elements with positive gains plot above the isocon reference line (fig. 13) and were mobilized from the hydrothermal fluids into the carbonate-altered granite. The rest of the trace elements have losses compared to unaltered granite, indicated by negative $\Delta C/C_{UA}$ and ΔC values (table 12); these plot below the isocon reference line (fig. 13), indicating depletion from the carbonate-altered granite.

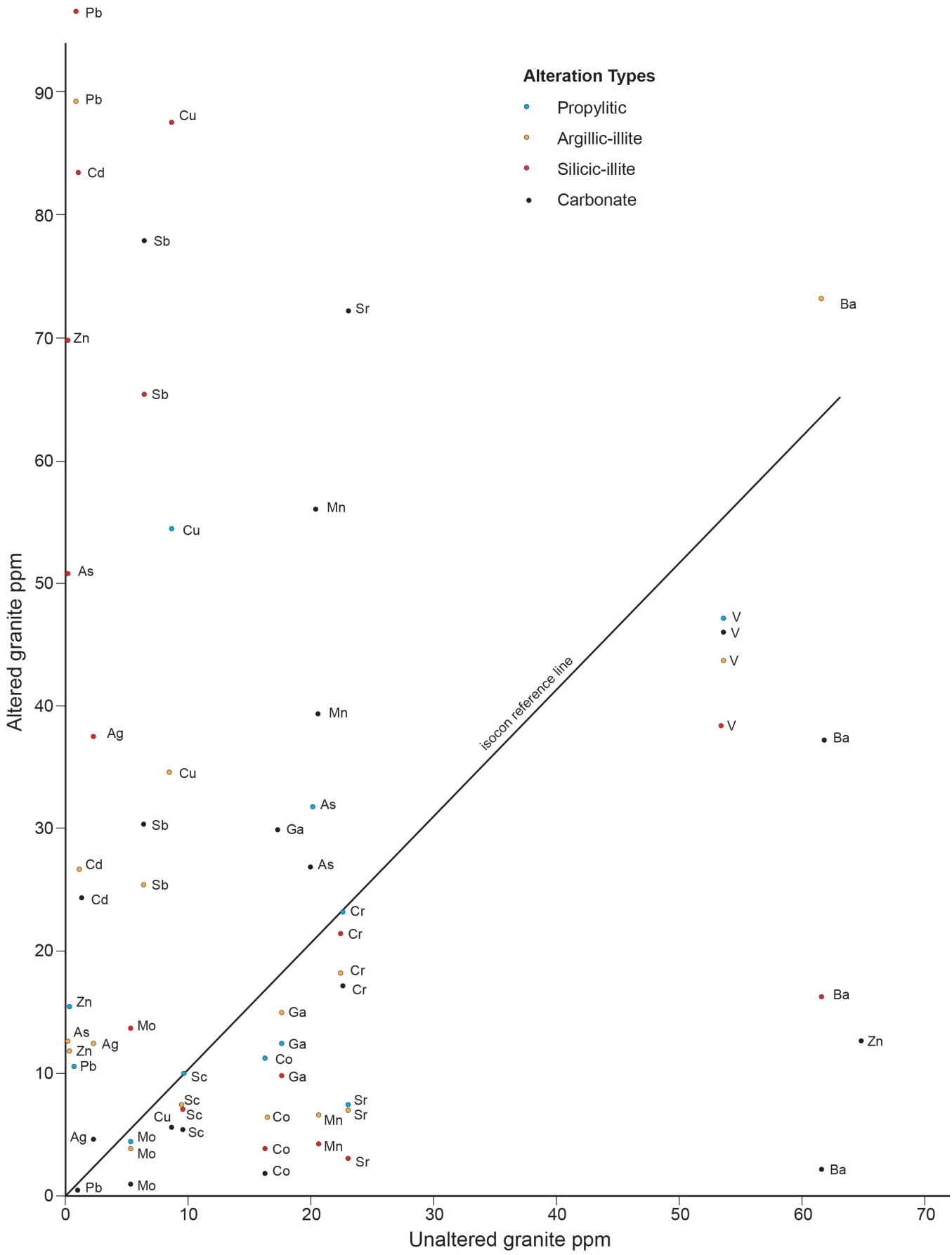

Figure 13. Isocon diagram showing trace elements losses and gains for silicic–illite, argillic–illite, propylitic, and carbonate alteration compared to unaltered granite isocon reference line. ppm, parts per million. Elements plotting below the reference line are lost and those plotting above show gains.

Table 9. Isocon analysis of trace element averages in parts per million (ppm) for propylitic alteration.

Element	C_{UA}	C_{PR}	C_{PR}/C_{UA}	$\Delta C/C_{UA}$	ΔC	Scale	C_{UA} Scaled	C_{PR} Scaled
Ag	2.6	4.5	1.73	0.73	1.9			
As	20	32	1.6	0.6	12			
Ba	615	377.5	0.61	-0.39	-237.5	0.1	61.5	37.8
Cd	1.7	40.6	23.88	22.88	38.9	0.6	1.02	24.4
Co	16.5	11.25	0.68	-0.32	-5.25			
Cr	22.3	23.3	1.04	0.04	1.0			
Cu	44.5	273	6.13	5.13	228.5	0.2	8.9	54.6
Ga	17.5	12.5	0.71	-0.29	-5			
Mn	688	1,310	1.9	0.9	622	0.03	20.6	39.3
Mo	5.5	4.8	0.87	-0.13	-0.7			
Pb	94.3	1,053.5	11.17	10.17	959.2	0.01	0.9	10.5
Sb	6.5	30.3	4.66	3.66	23.8			
Sc	9.8	10	1.02	0.02	0.2			
Sr	383.5	125.3	0.32	-0.68	-258.2	0.06	23	7.5
V	88.8	79	0.89	-0.11	-9.8	0.6	53.3	15.8
Zn	64.8	1,582	24.41	23.41	1517.2	0.01	0.65	47.4

Note. C_{UA}, component averages for unaltered granite; C_{PR}, component averages for propylitic alteration; C_{PR}/C_{UA}, slope of data points defining isocon; $\Delta C/C_{UA}$, gain or loss of elements compared to unaltered granite: negative numbers indicate a loss, positive numbers indicate a gain; ΔC, gain or loss of elements in ppm; scale, factor used to scale down element data to fit isocon plot; C_{UA} scaled, scaled components for unaltered granite; C_{PR} scaled, scaled components for propylitic alteration.

Table 10. Isocon analysis of trace element averages in parts per million (ppm) for argillic–illite alteration.

Element	C_{UA}	C_{AI}	C_{AI}/C_{UA}	$\Delta C/C_{UA}$	ΔC	Scale	C_{UA} Scaled	C_{AI} Scaled
Ag	2.6	12.5	4.81	3.81	9.9			
As	20	1,256	62.8	61.8	1,236	0.01	0.2	12.6
Ba	615	732.5	1.19	0.19	117.5	0.1	61.5	73.3
Cd	1.7	44.8	26.35	25.35	43.1	0.6	1.02	26.8
Co	16.5	6.3	0.38	-0.62	-10.2			
Cr	22.3	18.3	0.82	-0.18	-4.0			
Cu	44.5	172	3.87	2.87	127.5	0.2	8.9	34.4
Ga	17.5	15	0.86	-0.14	-2.5			
Mn	688	230.5	0.34	-0.66	-457.5	0.03	20.6	6.9
Mo	5.5	4	0.73	-0.27	-1.5			
Pb	94.3	8,940.3	94.81	93.81	8,846	0.01	0.9	89.4
Sb	6.5	25.3	3.89	2.89	18.8			
Sc	9.8	7.8	0.80	-0.20	-2.0			
Sr	383.5	122.5	0.32	-0.68	-261	0.06	23	7.4
V	88.8	73.5	0.83	-0.17	-15.3	0.6	53.3	44.1
Zn	64.8	1,020	15.75	14.75	955.5	0.01	0.65	10.2

Note. C_{UA}, component averages for unaltered granite; C_{AI}, component averages for argillic–ilite alteration; C_{AI}/C_{UA}, slope of data points defining isocon; $\Delta C/C_{UA}$, gain or loss of elements compared to unaltered granite: negative numbers indicate a loss, positive numbers indicate a gain; ΔC, gain or loss of elements in ppm; scale, factor used to scale down element data to fit isocon plot; C_{UA} scaled, scaled components for unaltered granite; C_{AI} scaled, scaled components for argillic–illite alteration.

Table 11. Isocon analysis of trace element averages in parts per million (ppm) for silicic-illite alteration.

Element	C_{UA}	C_{SI}	C_{SI}/C_{UA}	$\Delta C/C_{UA}$	ΔC	Scale	C_{UA} Scaled	C_{SI} Scaled
Ag	2.6	37.7	14.5	13.5	35.1			
As	20	5093.4	254.67	253.67	5073.4	0.01	0.2	50.9
Ba	615	168	0.27	-0.73	-447	0.1	61.5	16.8
Cd	1.7	139.7	82.18	81.18	138	0.6	1.02	83.8
Co	16.5	4	0.24	-0.76	-12.5			
Cr	22.3	21.8	0.98	-0.02	-0.05			
Cu	44.5	439	9.87	8.87	394.5	0.2	8.9	87.8
Ga	17.5	10	0.57	-0.43	-7.5			
Mn	688	138.2	0.20	-0.80	-549.8	0.03	20.6	4.2
Mo	5.5	13.8	2.51	1.51	8.3			
Pb	94.3	9,688	102.75	101.75	9593.7	0.01	0.9	96.9
Sb	6.5	65.8	10.12	9.12	59.3			
Sc	9.8	7.2	0.73	-0.27	-2.6			
Sr	383.5	53.6	0.14	-0.86	-329.9	0.06	23	3.2
V	88.8	65	0.73	-0.27	-23.8	0.6	53.3	39
Zn	64.8	6,888.2	106.3	105.3	6823.4	0.01	0.65	68.9

Note. C_{UA}, component averages for unaltered granite; C_{SI}, component averages for silicic–illite alteration; C_{SI}/C_{UA}, slope of data points defining isocon; $\Delta C/C_{UA}$, gain or loss of elements compared to unaltered granite: negative numbers indicate a loss, positive numbers indicate a gain; ΔC, gain or loss of elements in ppm; scale, factor used to scale down element data to fit isocon plot; C_{UA} scaled, scaled components for unaltered granite; C_{SI} scaled, scaled components for argillic–illite alteration.

Table 12. Isocon analysis of trace element averages in parts per million (ppm) for carbonate alteration.

Element	C_{UA}	C_{CA}	C_{CA}/C_{UA}	$\Delta C/C_{UA}$	ΔC	Scale	C_{UA} Scaled	C_{CA} Scaled
Ag	2.6	<0.5						
As	20	27	1.35	0.35	7	0.01	0.2	0.27
Ba	615	25	0.04	-0.96	-590	0.1	61.5	2.5
Cd	1.7	<0.5						
Co	16.5	2	0.12	-0.88	-14.5			
Cr	22.3	17	0.76	-0.24	-5.3			
Cu	44.5	29	0.65	-0.35	-15.5	0.2	8.9	5.8
Ga	17.5	30	1.71	0.71	12.5			
Mn	688	1,872.5	2.72	1.72	1,184.5	0.03	20.6	56.2
Mo	5.5	1	0.18	-0.82	-4.5			
Pb	94.3	29.5	0.31	-0.69	-64.8	0.01	0.9	0.29
Sb	6.5	78	12.0	11.0	71.5			
Sc	9.8	5.5	0.56	-0.44	-4.3			
Sr	383.5	1,207.5	3.15	2.15	824	0.06	23	72.5
V	88.8	77	0.87	-0.13	-11.8	0.6	53.3	46.2
Zn	64.8	13	0.20	-0.80	-51.8			

Note. $C_{UA,}$ component averages for unaltered granite; C_{CA}, component averages for carbonate alteration; C_{CA}/C_{UA}, slope of data points defining isocon; $\Delta C/C_{UA}$, gain or loss of elements compared to unaltered granite: negative numbers indicate a loss, positive numbers indicate a gain; ΔC, gain or loss of elements in ppm; scale, factor used to scale down element data to fit isocon plot; C_{UA} scaled, scaled components for unaltered granite; C_{CA} scaled, scaled components for argillic–illite alteration.

VEIN MINERALOGY

Mineral identification techniques consisted of reflected and transmitted light microscopy and scanning electron microscope-energy dispersive spectroscopy (SEM-EDS) using 15 polished sections, 33 polished thin sections, and 17 thin sections. Mineral identification was done at the Center for Advanced Mineral and Metallurgical Processing at Montana Tech using a Tescan Mira 3 scanning electron microscope equipped with a Tescan EDX detector for the SEM-EDS analysis and backscatter electron (BSE) images. Additional mineral identifications using SEM-EDS analysis utilized grains and crystals extracted from cut slabs and hand specimens.

Results showed the identification of 35 minerals from eight groups (table 13). The most important mineral group is the primary and secondary sulfide and sufosalt minerals. These minerals occur as disseminations and fracture fillings in the quartz veins. Most of the metals produced from the district came from the sulfide and sulfosalt mineral group. Native silver was a minor occurrence found only at the Attowa mine in a microvug with quartz crystals. Native sulfur is a secondary mineral filling fractures in altered sulfide minerals.

The oxide minerals are both secondary and primary, occurring as disseminations in the quartz veins and altered host granite. Rutile is the only primary oxide mineral occurring as disseminated grains in vein quartz. The secondary oxide minerals replace the sulfide minerals along fractures and on mineral surfaces. Iron oxide minerals occur as disseminations and fracture fillings in the altered host granite.

Carbonate minerals are secondary, occurring in the altered host granite and quartz veins as disseminations, fracture fillings, and replacements. The carbonate minerals ankerite, cerrusite, and malachite replace primary sulfide minerals on surfaces and along fractures. Calcite and dolomite fill fractures and open spaces in carbonate altered host granite.

Two primary silicate minerals, quartz and schorl, occur in the veins. The veins are composed of massive fine- to coarse-grained white to clear quartz filling faults and open spaces between brecciated and silicified granite. Quartz commonly occurs as massive compacted intergrown anhedral to subhedral grains completely filling open spaces. When open space filling is incomplete, quartz forms euhedral crystals in vugs. Schorl occurs as needles disseminated in quartz near the vein margins and in silicified host granite. Chrysocolla is a secondary copper silicate

Table 13. Summary of minerals identified from the Big Foot veins: vein paragenesis.

Mineral	Formula
Sulfides-	
Sulfosalts	
Arsenopyrite	$FeAsS$
Bournonite	$PbCuSbS_3$
Chalcopyrite	$CuFeS_2$
Covellite	CuS
Digenite	Cu_9S_5
Galena	PbS
Greenockite	CdS
Pyrargyrite	Ag_3SbS_3
Pyrite	FeS_2
Sphalerite	ZnS
Tennantite	$Cu_6Cu_4(Fe,Zn)_2(As,Sb)_4S_{13}$
Tetrahedrite	$Cu_6Cu_4(Fe,Zn)_2(Sb,As)_4S_{13}$
Native Element	
Silver	Ag
Sulfur	S
Oxides	
Goethite	$\alpha–Fe^{3+}O(OH)$
Hematite	$\alpha – Fe_2O_3$
Rutile	TiO_2
Bindheimite	$Pb_2Sb_2O_6(O,OH)$
Carbonates	
Ankerite	$Ca(Fe^{2+},Mg,Mn)(CO_3)_2$
Calcite	$CaCO_3$
Cerussite	$PbCO_3$
Dolomite	$MgCa(CO_3)_2$
Malachite	$Cu^{2+}_2(CO_3)(OH)_2$
Silicate	
Chrysocolla	$(Cu,Al)_2H_2Si_2O_5(OH)_4 \cdot nH_2O$
Quartz	SiO_2
Schorl	$Na(Fe^{2+})_3Al_6(BO_3)_3[Si_6O_{18}](OH)_4$
Phosphate	
Apatite-(Caf)	$Ca_5(PO_4)_3F$
Monazite-(Ce)	$(Ce,La,Nd)PO_4$
Pyromorphite	$Pb_5(PO_4)_3CL$
Sulfates	
Anglesite	$PbSO_4$
Linarite	$PbCu^{2+}(SO_4)(OH)_2$
Plumbojarosite	$PbFe_6(SO_4)_4(OH)_{12}$
Jarosite	$KFe_3(SO_4)_2(OH)_6$
Arsenate	
Mimetite	$Pb_5(AsO_4)_3Cl$
Scorodite	$Fe^{3+}AsO_4 \cdot 2H_2O$

mineral filling fractures in quartz and host granite.

The phosphate minerals are both primary and secondary. Apatite-(CaF) and monazite-(Ce) are primary minerals that occur as disseminations in the quartz veins and host granite. Pyromorphite is a secondary mineral that replaces the primary sulfide minerals and occurs as fracture and open space fillings in the quartz veins and altered host granite.

The sulfate and arsenate minerals are secondary and replace the primary sulfide minerals along fractures and on grain surfaces. Secondary minerals also occur in fractures and open spaces in vein quartz and altered host granite. Secondary minerals formed microcrystals in open fractures and spaces.

Paragenesis defines the sequence of mineralization within the vein systems. Characterization and identification of vein paragenesis was determined from SEM-backscatter images, microscopic examination of polished sections, thin sections, and polished thin sections, and examination of cut slabs and hand specimens. Mineralizing textures, including mineral overgrowths, replacements on grain boundaries, open space and fracture fillings, and mineral disseminations revealed a mineralizing sequence (fig. 14). This mineralization sequence is a reflection of the physical and chemical changes of the hydrothermal fluids during vein development. Physical events such as wall-rock reactions, fluctuating temperatures and pressures, and influx of meteoric water can influence the mineralization sequence. The introduction of different metals during vein development will generate different minerals, reflected in the vein paragenesis shown in figure 14. Two mineralizing events and host rock alteration developed the Big Foot veins.

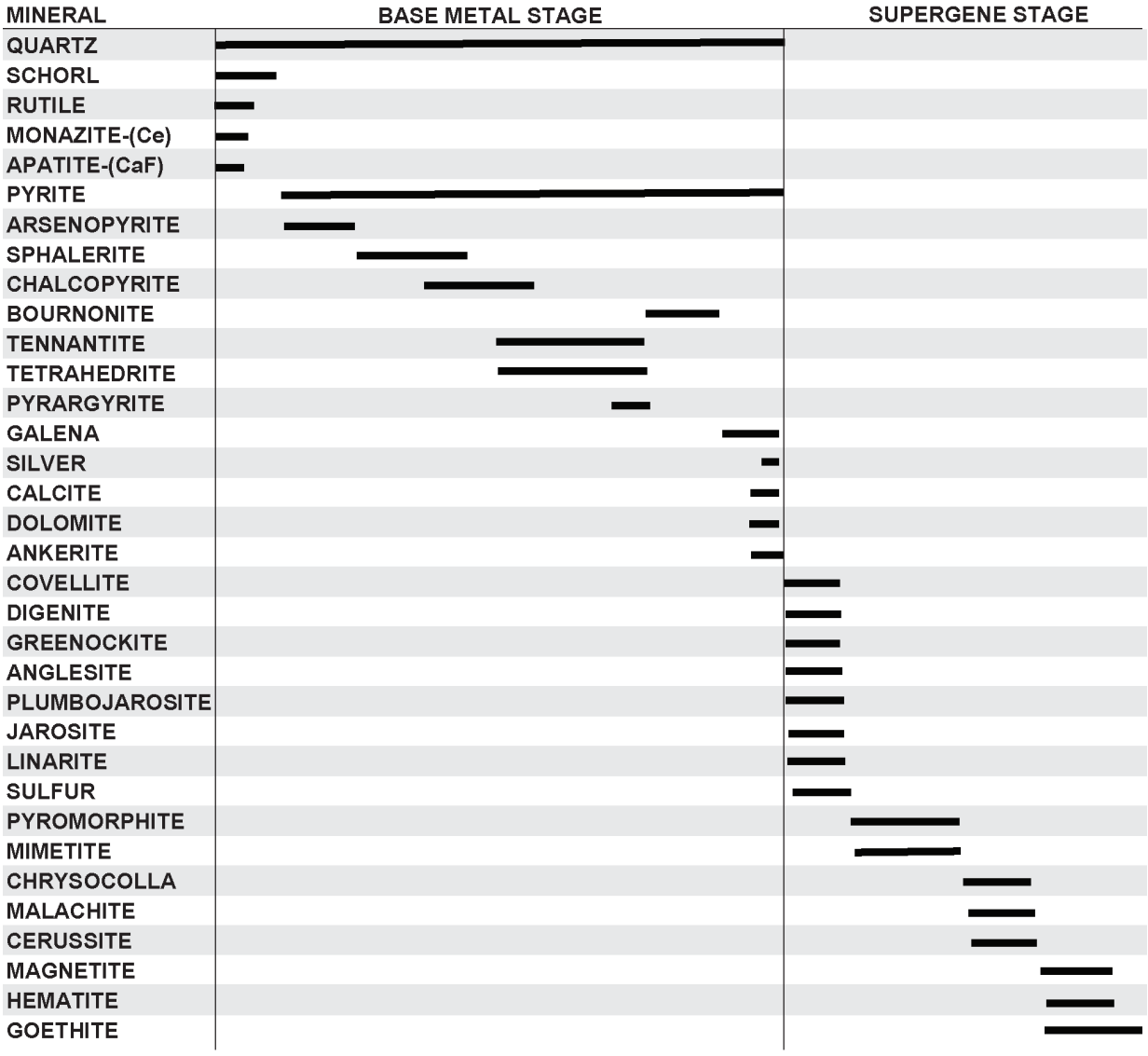

Figure 14. Paragenesis of base metal and supergene mineralizing events for the Big Foot veins.

Host Rock Alteration Minerals

Short-wave infrared spectrometry and illite spectral maturity scaler identified two alteration types, a high-temperature silicic–illite alteration and a low-temperature argillic–illite alteration (fig. 4). Silicic–illite alteration that took place during vein development is characterized by K–illite, phengite, schorl, illite–smectite, disseminated pyrite, and intense silicification of the host granite. Silicic–illite alteration grades into the quartz veins and becomes part of the veins along the granite contact. Quartz veinlets with inclusions of schorl needles and schorl veinlets occur as fracture and breccia fillings in the silicified granite. Low-temperature argillic–illite alteration characterized by minerals generated from weathering and meteoric water alteration overprints high-temperature silicic–illite alteration. K–illite and a variety of clay minerals are the most common minerals related to low-temperature alteration. Other common minerals related to weathering and meteoric water alteration include goethite, ferrihydrite, jarosite, hematite, and poorly crystallized kaolinite.

Base Metal Stage Minerals

Minerals representing base metal stage mineralization are identified on SEM-BSE images in figure 15. The paragenetic sequence (fig. 14) represents changes in fluid chemistry and temperatures during vein development. Schorl and quartz were the first minerals to crystallize as veinlets in the brecciated silicic–illite altered granite wall rock and altered granite breccia fragments assimilated into the quartz veins. Rutile, monzanite-(Ce), and apatite-(Ca,F) crystallized along with schorl during early vein development. Pyrite and arsenopyrite followed, representing the first sulfide minerals to precipitate, and pyrite crystallized continuously throughout the base metal stage. Later pyrite partially replaced arsenopyrite (fig. 15A).

With the introduction of zinc, copper, antimony, and silver, shalerite started crystallizing and overprinted arsenopyrite and early pyrite. Following sphalerite, a variety of copper minerals developed, including chalcopyrite, tennantite, tetrahedrite, and bournonite. Chalcopyrite was the first copper mineral to crystallize and replace sphalerite along cleavage planes. Tennantite and tetrahedrite precipitated simultaneously followed by bournonite with the introduction of lead (fig. 15B). Tetrahedrite is silver bearing and pyrargyrite crystallized along with tennantite (fig. 15C). Following pyrargyrite, native silver crystallized as wires (fig. 16) in open spaces in quartz. Galena crystallized last, enclosing and filling fractures in early formed minerals (figs. 15A, 15D). At the close of the base metal stage, carbonate minerals crystallized in fractures.

Supergene Stage Minerals

Supergene mineralization was the final stage that led to the development of oxide, arsenate, phosphate, sulfate, and secondary sulfide minerals (fig. 14). Some of the supergene minerals identified by SEM-EDS are identified on BSE images in figure 17. The secondary minerals developed from meteoric fluids reacting with primary sulfide minerals and vein weathering. Supergene alteration was minor at most mines but strongly developed at the Mountain Queen mine.

Leaching of the primary sulfide minerals and granite host rock supplied the elements that developed the supergene minerals. Covellite and digenite replaced chalcopyrite along grain margins (fig. 17A). Greenockite fills fractures and coats galena (fig. 17E), and anglesite replaces galena along grain margins and fractures (fig. 17B). Native sulfur fills fractures in chalcopyrite (fig. 17D). The sulfate minerals jarosite, plumbojarosite, and linarite fill open spaces and fractures in quartz and may have developed from a weathering process. Bindheimite, scorodite, and mimetite developed from the dissolution of arsenopyrite, galena, and tennantite (fig. 17C). Pyromorphite and mimetite fill fractures and open spaces in quartz veins; malachite and chrysocolla likewise fill and coat fractures in vein quartz. The iron oxide minerals deposited in fractures and replacing pyrite are most likely weathering products.

VEIN TRACE ELEMENTS

ALS Minerals, Inc. analyzed 18 vein samples for 48 trace elements by four acid digestion ICP-MS methods. Gold analyzed by fire assay was by ICP-AES or gravimetric finish. Analysis of ore-grade elements was by four acid digestion and ICP-AES methods. Results reported in appendix D for 19 elements show anomalous concentrations compared to unaltered and altered granite. Table 14 lists average analytical results for vein samples collected from mine dumps and ore stockpiles. Samples represent mined quartz veins with disseminated sulfide minerals that show multiple stages of quartz crystallization as open space fillings in brecciated and silicified granite. Sample size ranged from 0.63 to 1.27 kg, averaging 0.8 kg.

Losses or gains of trace element concentrations for quartz veins (Cv) compared to unaltered granite (C_{UA}) are presented on an isocon diagram and table

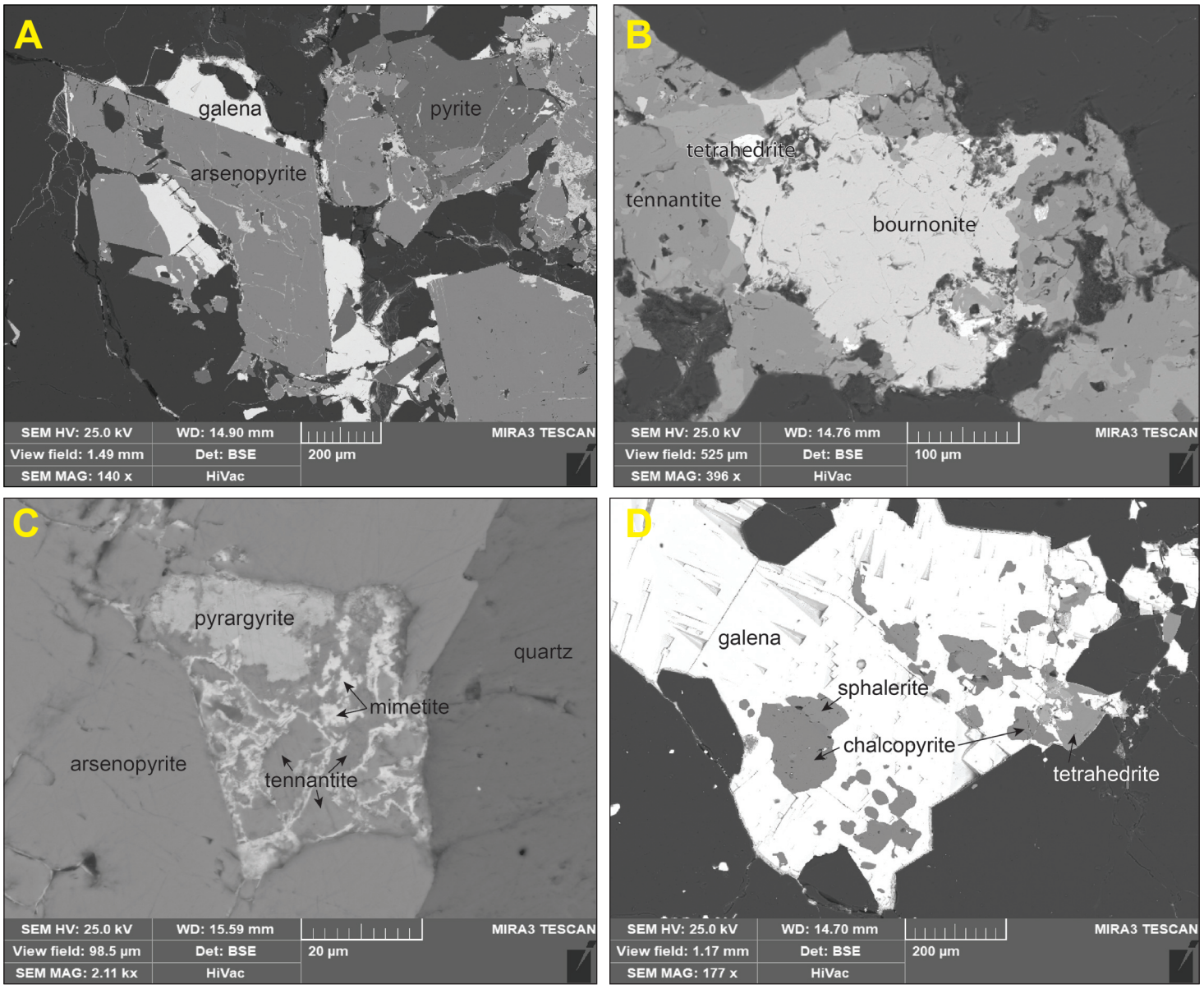

Figure 15. SEM-BSE images of primary sulfide minerals in quartz. (A) Euhedral to anhedral arsenopyrite grains partially replaced by pyrite with open spaces and fractures filled with galena. (B) Bournonite filling open space and partially replacing tennantite and tetrahedrite. (C) Pyrargyrite partially replacing tennantite filling open space in arsenopyrite. Tennantite partially replaced by mimetite along fractures. (D) Rounded sphalerite, chalcopyrite, and tetrahedrite grains included in late stage galena.

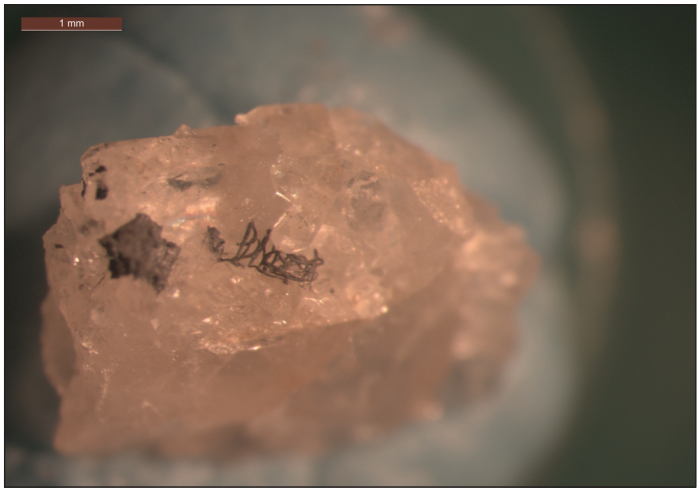

Figure 16. Silver wires in quartz vug with euhedral quartz crystals and galena inclusion from Attowa mine.

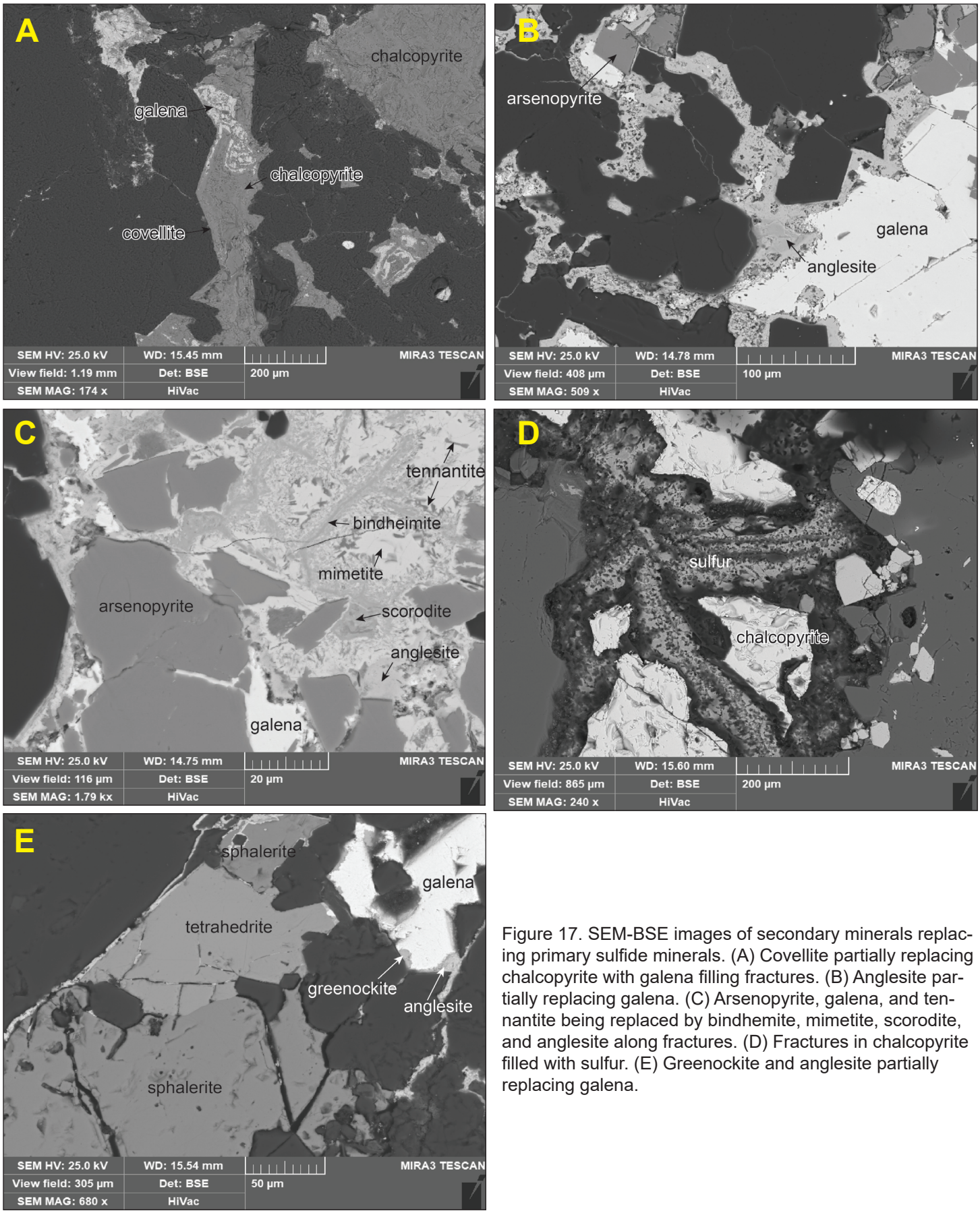

Figure 17. SEM-BSE images of secondary minerals replacing primary sulfide minerals. (A) Covellite partially replacing chalcopyrite with galena filling fractures. (B) Anglesite partially replacing galena. (C) Arsenopyrite, galena, and tennantite being replaced by bindhemite, mimetite, scorodite, and anglesite along fractures. (D) Fractures in chalcopyrite filled with sulfur. (E) Greenockite and anglesite partially replacing galena.

Table 14. Analytical averages of elements with anomalous results for sulfide-quartz veins from mines and prospects throughout the Big Foot mining district compared to unaltered granite.

Element	Unaltered Granite (ppm)	*n*	Quartz Veins (ppm)	*n*
Au	NA		3.6	18
Ag	2.6	1	160.6	18
As	20	4	4,522.5	18
Ba	615	4	158.9	18
Bi	<2	4	78.5	18
Cd	1.7	1	235.8	18
Co	16.5	4	35.6	18
Cu	44.5	4	3,638	18
Ga	17.5	4	4.3	18
Li	NA		16.4	18
Mn	688	4	174	18
Mo	5.5	4	65.9	18
Pb	94.3	4	50,751.6	18
Rb	NA		57.3	18
Sb	6.5	4	279.8	18
Sc	9.8	4	2.6	18
Sr	383.5	4	48.4	18
V	88.8	4	40.1	18
Zn	64.8	4	6,473.4	18

Note. Granite analyzed by ICP-AES methods. Quartz veins analyzed by ICP-MS methods. Gold analyzed by fire assay. All results in parts per million (ppm); NA, not analyzed; *n*, number of samples used in averages.

(fig. 18, table 15). Isocon analysis results show there are no conserved elements with equal concentrations between unaltered granite and quartz veins, indicated by isocon slopes C_V/C_{UA} being well below or above 1, and cannot be used to define an isocon reference line. The isocon reference line in figure 18 is taken from figure 13 and uses trace elements Sc and Cr between unaltered granite and propylitic alteration. Losses and gains of individual elements were determined using isocon analysis methods from Grant (2005) and Kuwatani and others (2020). Analytical values too large to reasonably fit on the isocon diagram were scaled down (table 15).

The isocon analysis in table 15 indicates gains and losses by positive or negative values for $\Delta C/C_{UA}$ and ΔC. The trace elements As, Cu, Pb, and Zn have the highest positive $\Delta C/C_{UA}$ and ΔC values (table 15) compared to the other elements. These plot well above the isocon reference line (fig. 18), indicating a high degree of concentration during quartz vein development. The other trace elements Ag, Cd, Co, Mo, and Sb have positive $\Delta C/C_{UA}$ and ΔC values (table 15) and plot above the isocon reference line (fig. 18), indicating anomalous concentrations gained during quartz vein development. Trace elements that were lost compared to unaltered granite are Ba, Ga, Mn, Sc, Sr, and V, as indicated by negative $\Delta C/C_{UA}$ and ΔC values (table 15), and these plot below the isocon reference line (fig. 18). Trace elements depleted during quartz vein development have negative $\Delta C/C_{UA}$ and ΔC values and are not anomalous compared to unaltered granite.

QUARTZ CATHODOLUMINESCENCE

Quartz is the most common mineral and occurs in all the veins throughout the district. Multiple quartz generations fill open spaces, and fractures in brecciated silicified granite, and replace granite breccia fragments assimilated into the veins. Quartz veins consist of fine- to coarse-grained white to clear anhedral compacted quartz grains with disseminated sulfides and sulfide minerals filling open spaces included with euhedral clear to milky quartz crystals. Clear to white euhedral quartz crystals line open vugs. The paragenetic sequence of these quartz generations reveals physical changes that took place during vein development.

Cathodoluminescence (CL) revealed the relationship between quartz crystallization and sulfide mineralization. A Tescan Mira3 scanning electron microscope equipped with a Tescan Pan Chromatic CL detector located at Montana Technological University

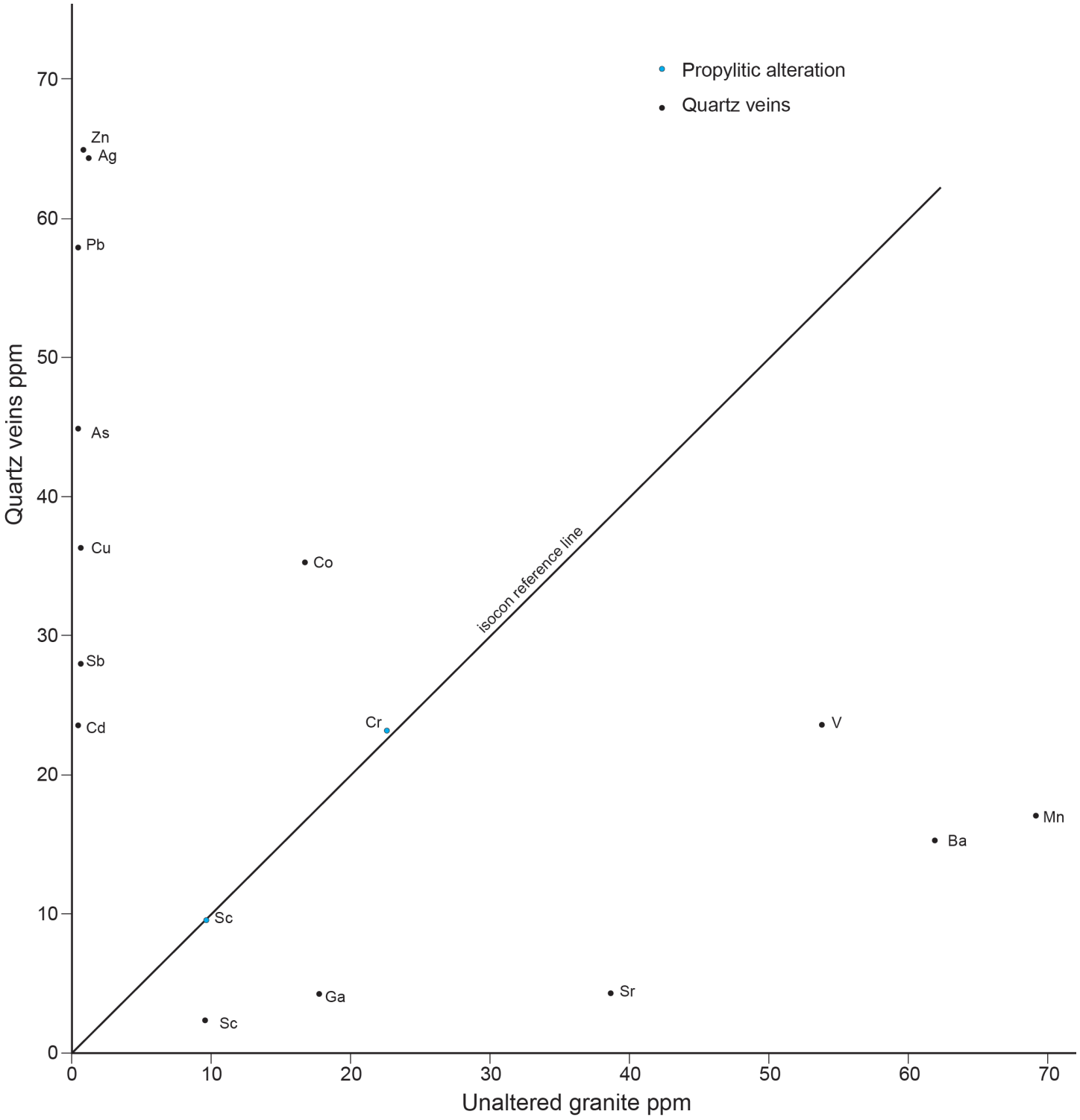

Figure 18. Isocon diagram showing trace element loss (plotting below reference line) and gains (plotting above reference line) for quartz veins compared to unaltered granite isocon reference line. ppm, parts per million.

Table 15. Isocon analysis of ICP-MS averages in parts per million (ppm) for quartz veins.

Elements	C_{UA}	C_v	C_V/C_{UA}	$\Delta C/C_{UA}$	ΔC	Scale	C_{UA} Scaled	C_V Scaled
Ag	2.6	160.6	61.8	60.8	158	0.4	1	64.3
As	20	4,522.5	226.1	225.1	4,502.5	0.01	0.2	45.2
Ba	615	158.9	0.26	-0.74	-456.1	0.1	61.5	15.9
Cd	1.7	235.8	138.7	137.7	234.1	0.1	0.2	23.6
Co	16.5	35.6	2.2	1.1	19.1			
Cu	44.5	3,638	81.8	80.8	3,593.5	0.01	0.5	36.4
Ga	17.5	4.3	0.25	-0.75	-13.2			
Mn	688	174	0.25	-0.75	-514	0.1	68.8	17.4
Mo	5.5	65.9	12	11	60.4			
Pb	94.3	50,751.6	538.2	537.2	50,657.3	0.001	0.09	50.8
Sb	6.5	279.8	43	42	273.3	0.1	0.7	28
Sc	9.8	2.6	0.27	-0.73	-7.2			
Sr	383.5	48.4	0.13	-0.87	-335.1	0.1	38.4	4.8
V	88.8	40.1	0.45	-0.55	-48.7	0.6	53.3	24
Zn	64.8	6,473.4	99.9	98.9	6,408.6	0.01	0.65	64.7

Note. C_{UA}, component averages for unaltered granite; C_V, component averages for quartz veins; C_V/C_{UA}, slope of data points defining isocon; $\Delta C/C_{UA}$, gain or loss of elements compared to unaltered granite: negative numbers indicate a loss, positive numbers indicate a gain; ΔC, gain or loss of elements in ppm; scale, factors used to scale down ICP-MS data to fit isocon plot; C_{UA} scaled, scaled components of unaltered granite; C_V scaled, scaled components for quartz veins.

Center for Advanced Metallurgical Processing was used to examine 14 polished thin sections representing veins from six mine locations for CL response. The instrument was set up with an electron beam acceleration of 15 and 20 kV, and beam intensity of 13 and 15 kV, with a working distance ranging from 12.5 to 14.97 mm. CL response varied from no response, resulting in a black image, to a strong response, yielding a bright white image. Some quartz grains showed a mottled image varying from bright to gray and others revealed euhedral forms with oscillatory growth bands. CL imaging revealed six quartz generations and two microbrecciation stages.

Brecciated primary quartz grains from the granite host gave a strong to moderate CL response with a mottled pattern (fig. 19). Quartz stringers filling fractures in the brecciated primary quartz grains did not give a strong CL response and appear as black to dark gray veinlets. The nonresponsive black background (fig. 19) is quartz and illite that partially replaces brecciated feldspar, and schorl and quartz filled fractures.

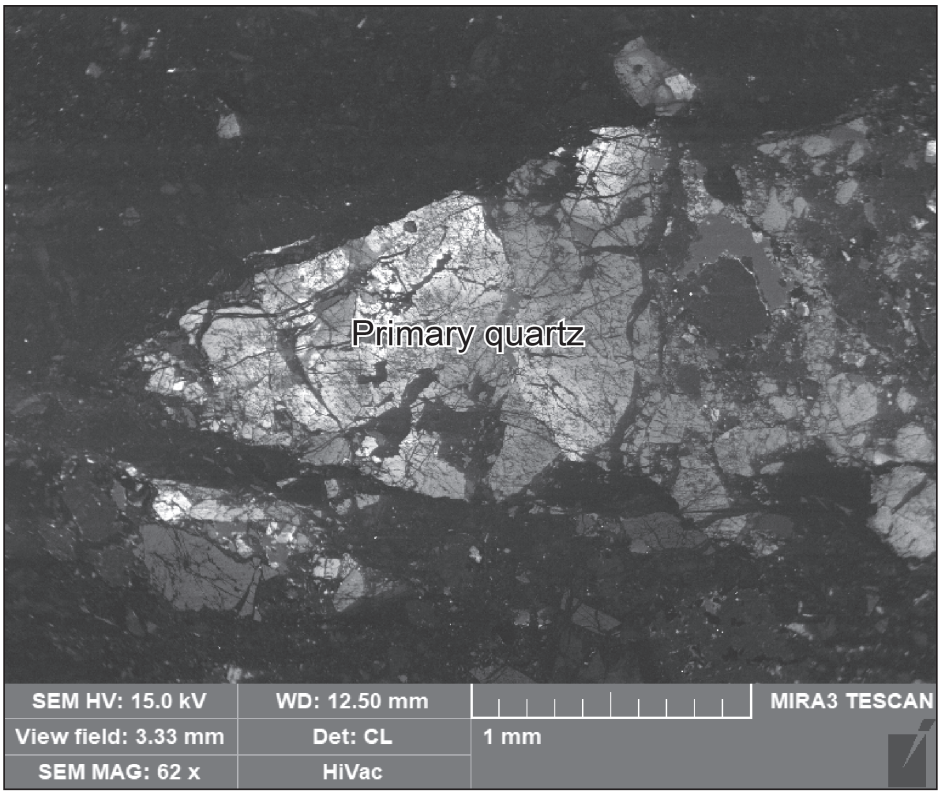

Figure 19. Primary quartz grain in silicic–illite altered host granite showing extensive microbrecciation and fracturing. Fractures filled with secondary quartz and schorl.

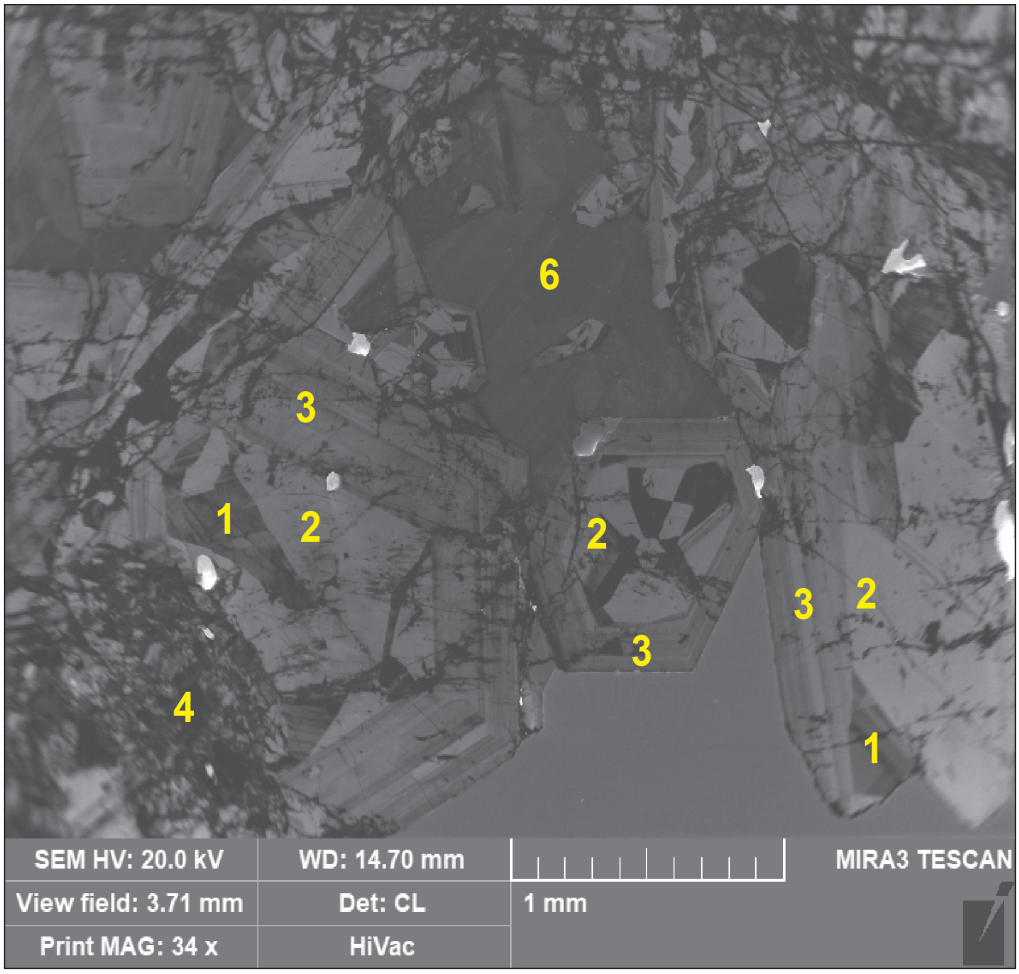

Figure 20. Multiple generations of quartz crystallization. The first generation (1) was fractured and replaced by second-generation quartz (2), both generations form the cores of euhedral crystals. A third quartz generation (3) showing oscillating growth zones was overgrown on generation one and two euhedral crystals. A fourth quartz generation (4) fills open spaces and fractures in microbrecciated euhedral crystals. A sixth non-brecciated generation (6) following sulfide crystallization fills open spaces adjacent to euhedral crystals.

Three quartz generations fill fractures and open spaces in the silicified and brecciated host granite. Microbrecciation followed the three quartz generations and a fourth quartz generation precipitated (fig. 20). The first generation (1, fig. 20) is not common and occurs as fragments showing oscillatory growth with a dark gray to black CL response located in the cores of euhedral crystals and overgrown by second and third quartz generations. The second quartz generation (2, fig. 20) gives an even light gray CL response and forms the cores of euhedral crystals overgrowing and replacing fragments of the first generation. Following the second generation, a third quartz generation (3, fig. 20) formed overgrowths on the first and second generations and defines the outer margins of euhedral crystals. The third quartz generation overgrowths gave a medium gray CL response and show oscillating growth bands.

After the first three generations developed, they underwent extensive fracturing and microbrecciation. This was followed by a fourth quartz generation filling fractures and partially replacing early quartz generations and cementing breccia fragments (4, fig. 20). The fourth quartz generation was nonresponsive to slightly responsive to CL activation, resulting in black to dark gray stringers and patches. The degree of fracturing and microbrecciation varied from moderate to extensive (figs. 21, 22). Moderate fracturing of the early quartz generations in figure 21 display numerous quartz stringers filling fractures in euhedral quartz crystals. Strongly brecciated early quartz generations shown in figure 22 consist of angular fragments of generation 2 and 3 quartz cemented with generation 4 quartz. Sulfide minerals represented by euhedral to anhedral pyrite grains that fill open spaces in the microbreccia and that are scattered in the breccia matrix precipitated with the fourth quartz generation (fig. 22).

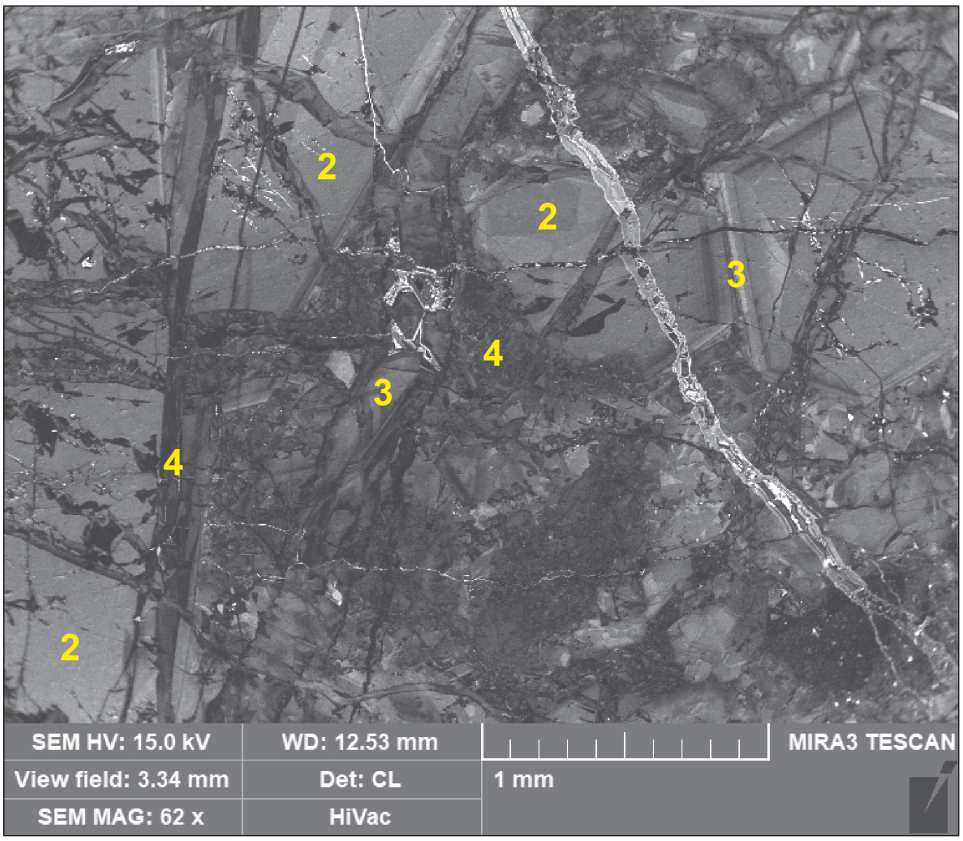

Figure 21. Fractured and partially brecciated generation two and three euhedral quartz crystals. Fractures filled with generation 4 quartz stringers and open space filling.

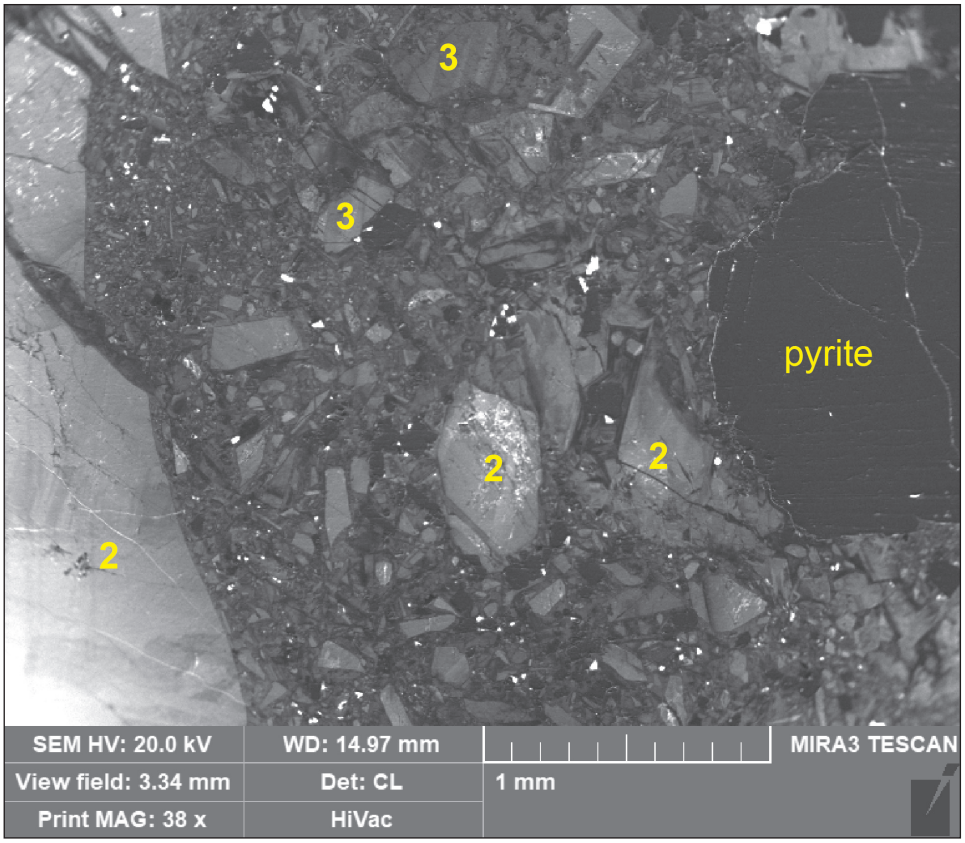

Figure 22. Intense microbrecciation of second- and third-generation quartz crystals (2 and 3) and grains. Open spaces between breccia fragments filled with a fourth quartz generation and pyrite (black grains).

A fifth quartz generation crystallized at the same time sulfide minerals precipitated in intensely brecciated early quartz stages. The fifth quartz generation (5, fig. 23) shows a strong Cl response and weak oscillatory growth zones. Pyrite grains (black CL response) are included in the base of the euhedral quartz crystals, suggesting simultaneous growth. Shortly after the quartz crystals formed, sphalerite precipitation followed, filling in the remaining open space. The fifth quartz generation did not undergo brecciation or fracturing and neither did the sulfide minerals; this indicates sulfide precipitation followed at the close of microbrecciation. The fifth quartz generation, represented by euhedral quartz crystals enclosed by sulfide minerals and lining open vugs, yielded the best fluid inclusions for study.

Following sulfide mineral precipitation, a sixth quartz generation crystallized in the remaining open spaces (6, fig. 20). The sixth generation gave a dark to medium gray Cl response and has a mottled appearance. This quartz stage along with the fifth stage did not show evidence of microbrecciation or fracturing.

FLUID INCLUSIONS

Microthermometric measurements of fluid inclusions were made to gain an understanding of the temporal evolution, salinity, and temperatures for the hydrothermal fluids that developed the veins. The fifth quartz generation identified by CL yielded the best fluid inclusions for study. Fluid inclusions in the other quartz stages were too small for reliable measurements or were lost due to fracturing and brecciation. Fluid inclusions were selected from euhedral quartz crystals (fifth quartz generation) and were analyzed on a Fluid, Inc. adapted USGS-type gas-flow heating freezing stage mounted on an Olympus BH-2 microscope located at the Geological Engineering Department, Montana Tech.

Six identified fluid inclusion types were type I, type II, liquid, vapor, and two types of three-phase inclusions (figs. 24–27). Type I inclusions are the most common and consist of liquid and <50 vol% vapor bubble (fig. 24). Type II inclusions are vapor dominated, consisting of liquid and >50 vol% vapor bubble (fig. 25). Single-phase inclusions consisting of all liquid or vapor were not common, and some of these may have developed from necking of larger two-phase inclusions. Three-phase inclusions with a halite

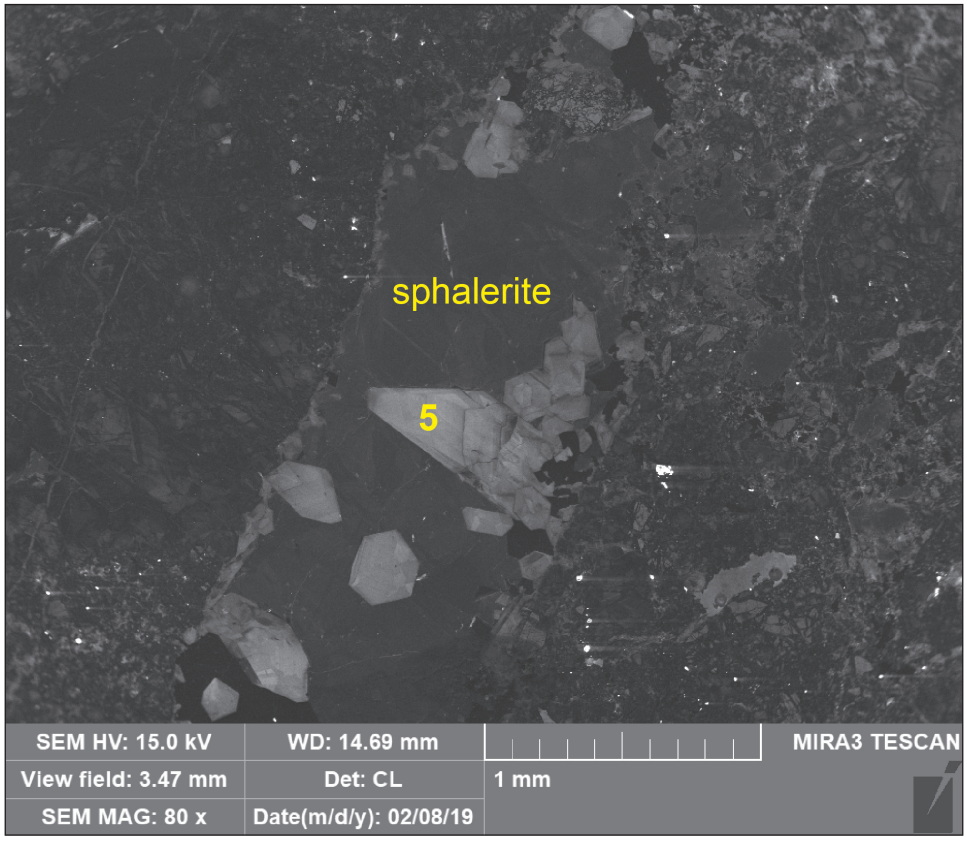

Figure 23. A fifth quartz generation (5) showing euhedral crystals with weak oscillatory growth that crystallized with sphalerite and pyrite in open space within brecciated second and third generations.

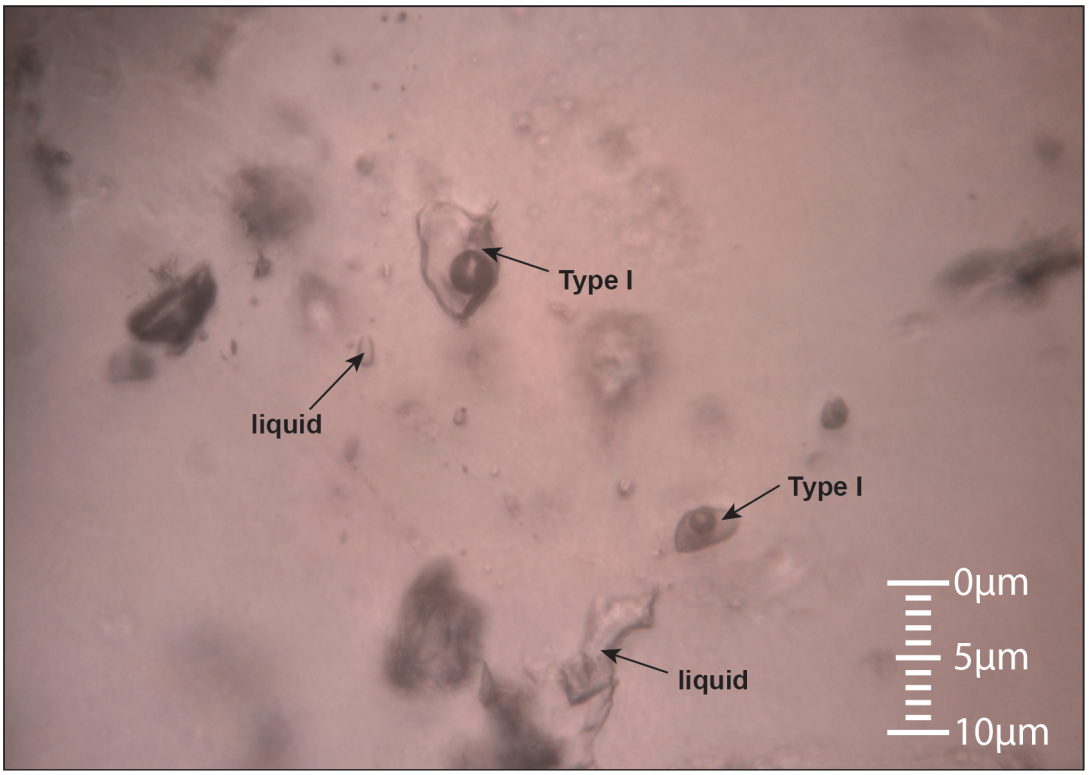

Figure 24. Primary type I two-phase and liquid fluid inclusions.

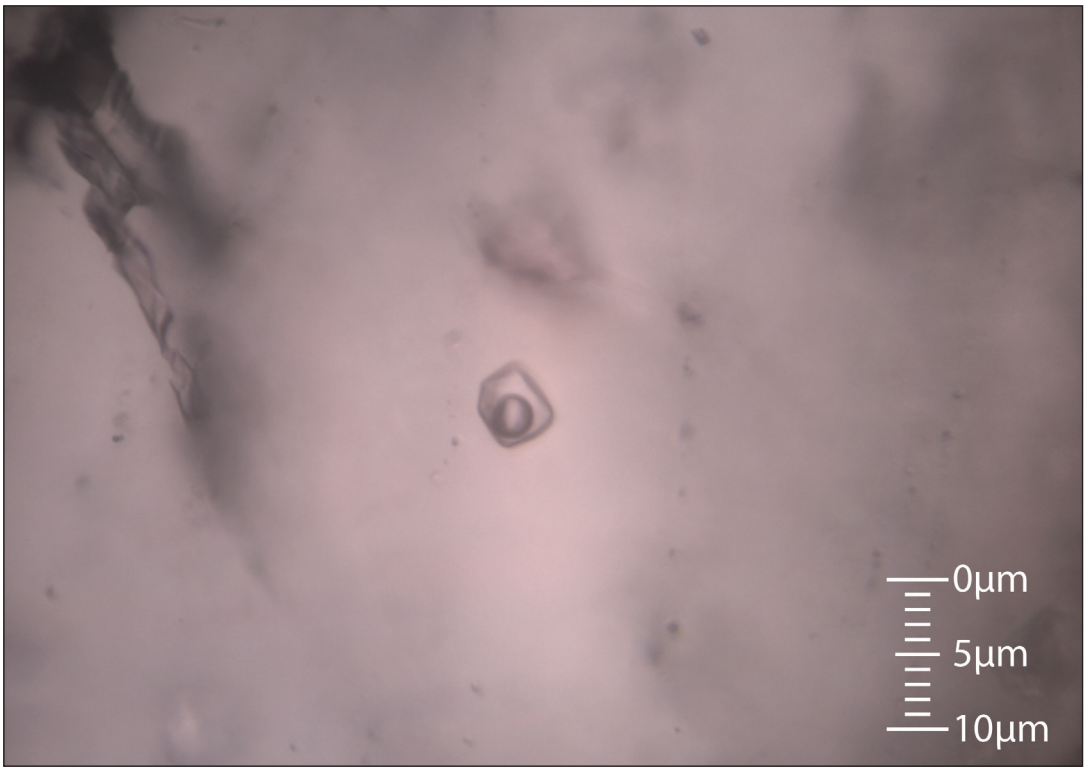

Figure 25. Primary type II two-phase fluid inclusion consisting of a vapor bubble and brine.

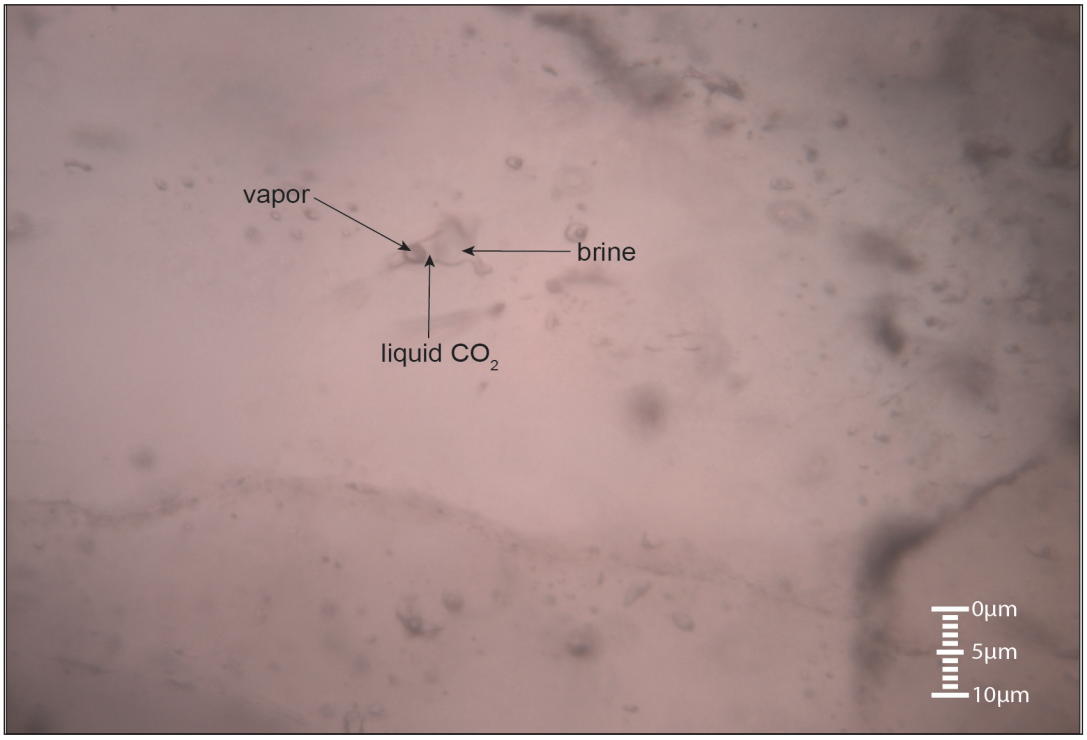

Figure 26. Three-phase fluid inclusion with liquid CO_2, vapor, and brine.

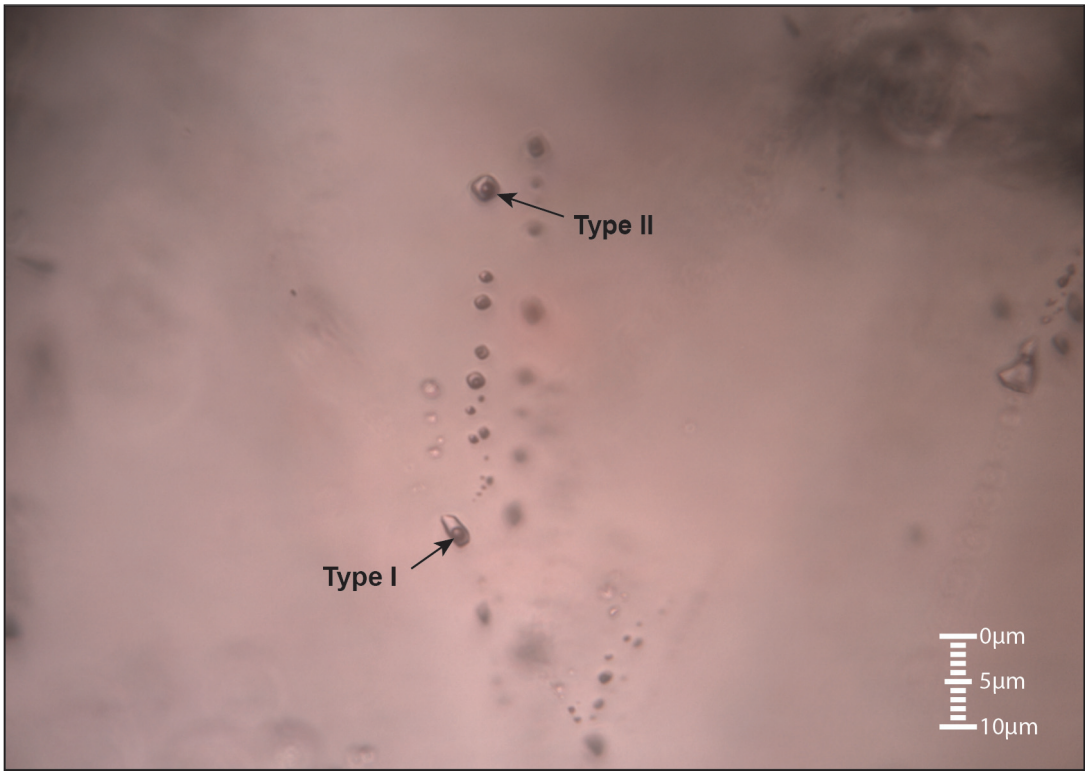

Figure 27. String of secondary type I and II fluid inclusions in a healed fracture.

daughter mineral, brine, and vapor were also present but are rare. These were found at nine locations. Another type of three-phase inclusion with liquid CO_2, a vapor bubble, and brine was identified in samples from six locations (fig. 26).

The designation between primary and secondary inclusions used the criteria outlined by Roedder (1984). Primary inclusions occur as groups trapped in quartz crystal growth zones and yielded data reflecting the time of entrapment. Primary inclusions are type I and II, liquid, and vapor or three phase. Secondary inclusions are found in healed fractures and can be type I and II, liquid, or vapor (fig. 27). Secondary inclusions give information on late-stage fluids trapped in healed fractures during the close of crystallization. Inclusions show evidence of necking, which will generate all liquid and all vapor inclusions. Necking may have taken place during fracture healing and recrystallization of primary quartz crystals.

A total of 181 quartz-hosted fluid inclusions were analyzed, including 161 two-phase type I and II, 9 three-phase inclusions with halite, and 11 three-phase inclusions with CO_2 liquid, vapor, and brine. Homogenization temperatures and wt% NaCl equivalent (eq) are summarized in table 16, and the complete data set is shown in appendix E. All two-phase inclusions yielded both homogenization temperature (Th) and wt% NaCl eq data, with the exception of one inclusion that only gave Th. Primary and secondary type I and II inclusions homogenized into a liquid phase. Homogenization temperatures for type I and II inclusions were the same for those in assemblages of 3D clusters. Fluid salinities for type I and II inclusions were determined by freezing with liquid nitrogen followed by melting the ice and recording the melting temperature (Tm) when the last ice crystal melted. Salinity calculated from the Tm used the methods of Roedder (1984).

Three-phase inclusions with liquid, vapor, and a halite daughter mineral homogenized in steps yielding homogenization and halite dissolution temperatures (table 16). Complete homogenization temperature was reached when both the vapor phase and halite phase assimilated into the liquid phase, yielding a homogenized liquid-filled inclusion. Salinities were calculated from the halite dissolution temperature method of Sterner and others (1988).

Three-phase inclusions with liquid CO_2 developed clathrate upon freezing, indicating dissolved CO_2 in the fluids at the time of entrapment. Homogenization temperatures were reached when the CO_2 liquid and vapor bubble assimilated into the brine phase and generated a homogenized liquid-filled inclusion. Salinities were determined from the clathrate melt temperature using the methods of Darling (1991).

Homogenization temperatures illustrated on a histogram plot (fig. 28) show two distinct populations. Most inclusions were trapped between 210ºC and 350ºC, indicating the veins developed from one hydrothermal event. Near the close of hydrothermal activity, a population of lower temperature inclusions ranging from 140ºC to 200ºC were trapped. These lower temperature inclusions could represent the close of hydrothermal activity.

Salinities illustrated on a histogram plot (fig. 29) show two distinct populations between 0 to 8 and 32 to 38 wt% NaCl eq. Most fluid inclusions fall in the 0 to 9 wt% NaCl eq range, and nine three-phase inclusions with halite daughter minerals fall in the 32 to 39 wt% NaCl eq range. Vein quartz from the State mine

Table 16. Summary of fluid inclusion data for type I and II, three phase with halite, and three phase with CO_2.

Inclusion Type	I and II	Three Phase with Halite	Three Phase with CO_2
ThºC range	148.9 to 347.5	216.5 to 314.0	247.0 to 312.3
ThºC average	268.9	276.3	292.8
TmºC ice range	-0.1 to -5.4		
TmºC ice average	-1.6		
wt% NaCl eq range	0.2 to 8.4	32.6 to 38.1	1.2 to 1.6
wt% NaCl eq average	2.6	33.6	1.4
ThºC halite range		209.8 to 298.9	
ThºC halite average		230.3	
TmºC clathrate range			6.9 to 9.5
TmºC clathrate average			8.3
n for all averages	161	9	11

Note. Complete data set is in appendix E. ThºC, homogenization temperature; TmºC ice, melting temperature of ice; wt% NaCl eq, weight percent NaCl equivalent; ThºC halite, homogenization temperature for halite; TmºC clathrate, melting temperature of clathrate; *n*, number of inclusions used for averages.Temperatures in degrees centigrade.

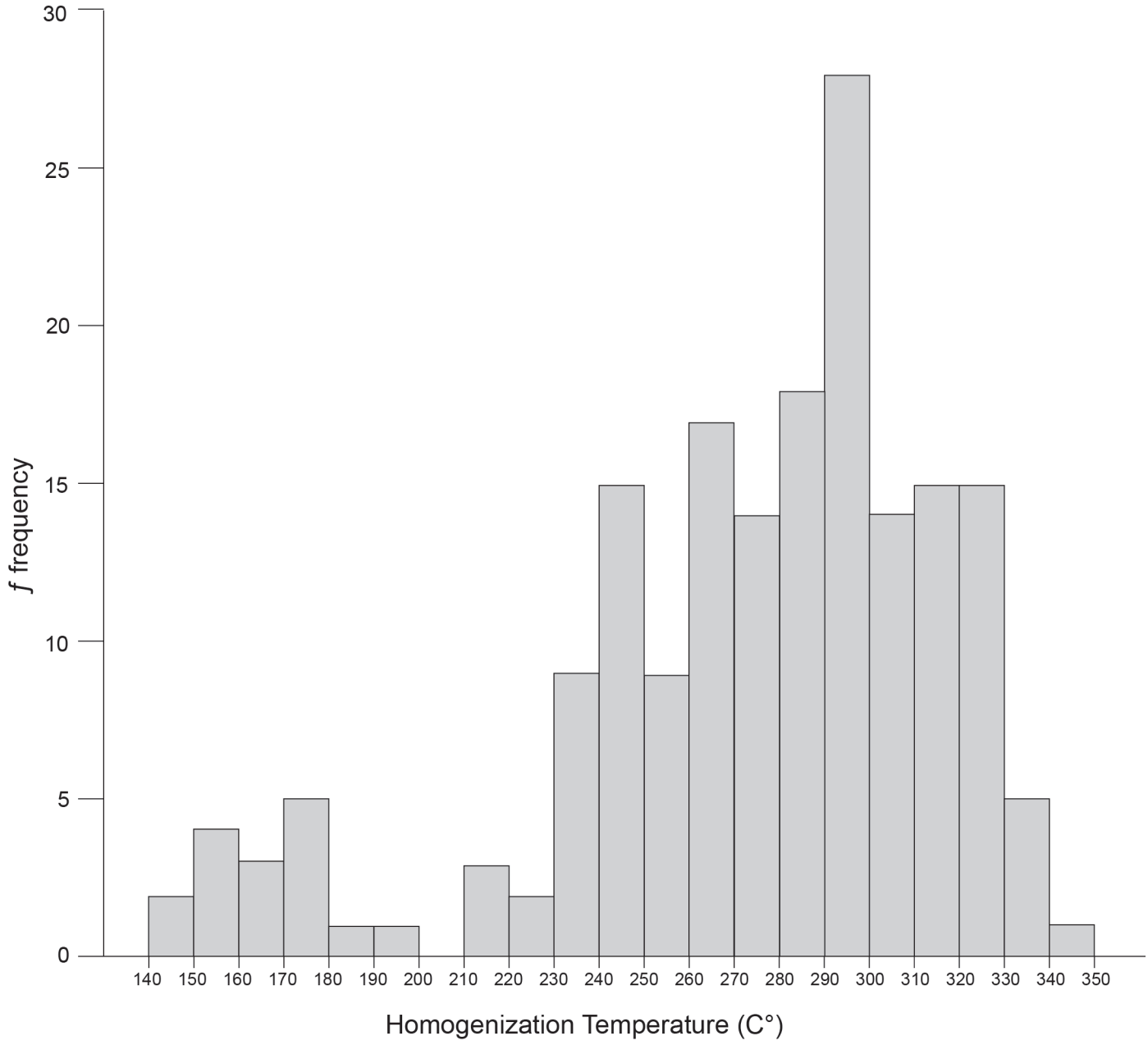

Figure 28. Histogram plot showing distribution of homogenization temperatures.

has type I and II fluid inclusions with salinities ranging from 6.0 to 8.4 wt% NaCl eq. The largest vein in the district developed by the Big Four, Nickel Plate, Ajax, and Attowa mines, has type I and II fluid inclusions with salinities ranging from 0.4 to 6.9 wt% NaCl eq. Further south in the district, veins developed by the Mountain Queen and St. Anthony mines, and prospects near Whitetail Park, have salinities ranging from 0.2 to 3.2 wt% NaCl eq for type I and II inclusions. Nine three-phase inclusions with halite daughter minerals have salinities ranging from 32 to 38 wt% NaCl eq. These occur in four veins throughout the district. One three-phase inclusion was found at the Big Four site (BF-4) and one at the Attowa site (BF-9); both of these sites are on the same vein cutting across the district. Further south, the Mountain Queen (BF-19) and St. Anthony veins (BF-54) each have one three-phase inclusion. Five three-phase inclusions were in a quartz vein developed by prospect pits (BF-63) near Whitetail Park (fig. 2).

On a salinity versus homogenization temperature plot, two distinct fields are displayed (fig. 30). Near the top of the diagram, a group of nine inclusions with halite daughter minerals with salinities ranging from 32.6 to 38.1 NaCl wt% eq form one field. The rest of the fluid inclusions plot near the bottom of the diagram and form a field represented by low salinity (0.1 to 8.4 NaCl wt% eq) with a wide temperature range (148.9º to 347.4ºC). The temperature corresponding

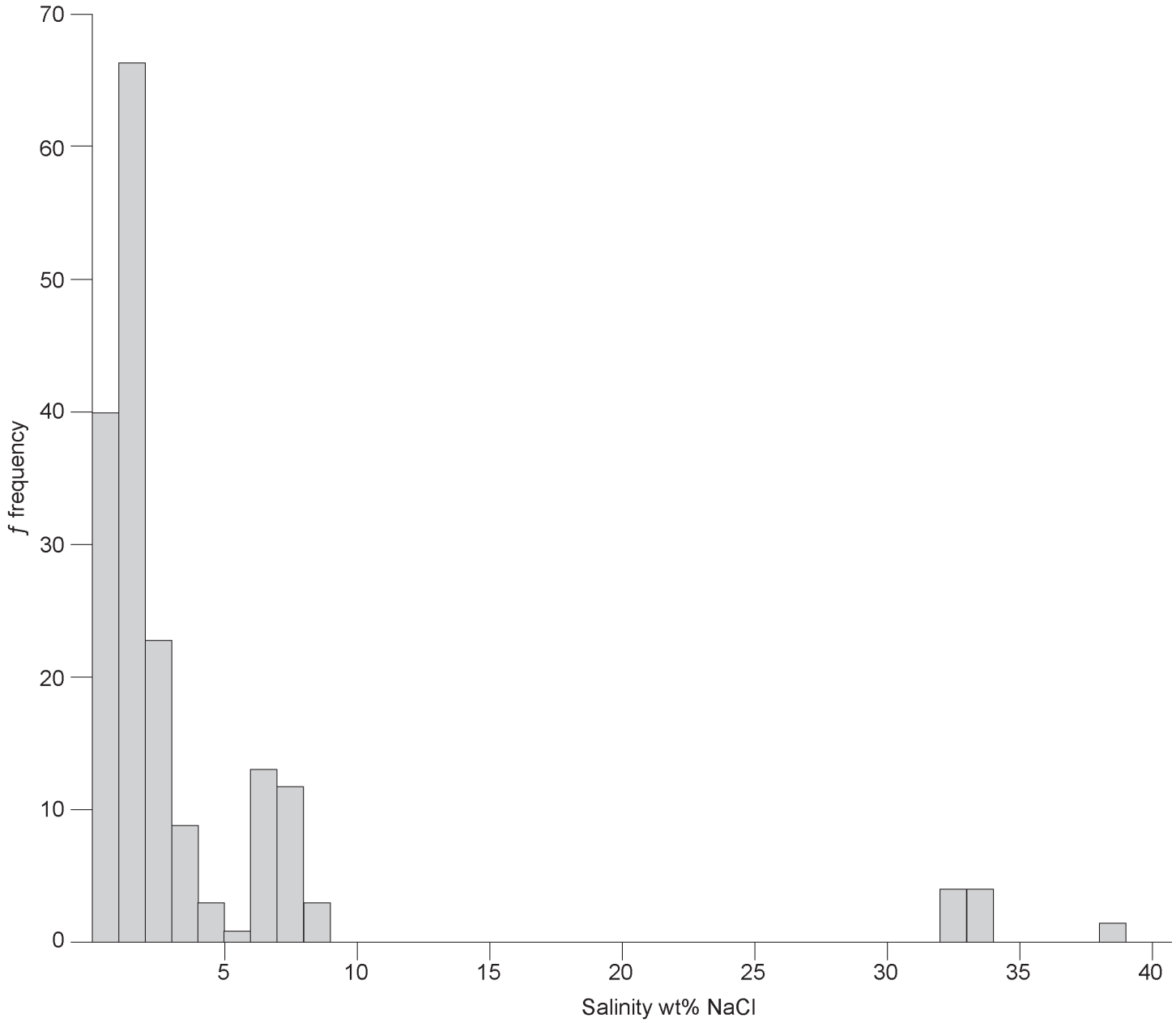

Figure 29. Histogram plot showing distribution of salinity in weight percent NaCl equivalent.

to both the high- and low-salinity fields overlap, and this shows salinities changed during vein evolution but temperature remained relatively constant. The diagram further shows lower (<200ºC) or higher (>300ºC) temperatures did not have an impact on salinity.

SULFUR ISOTOPES

Sulfur isotopes for 48 sulfide mineral samples were analyzed at the stable isotope laboratory of the U.S. Geological Survey Crustal Geophysics Geochemistry Science Center in Denver, Colorado. Analysis of sulfur isotopes was done by vacuum-line conversion to SO_2 followed by an elemental analyzer using a Thermo Delta Plus XP mass spectrometer. Samples were extracted under a microscope from cut slabs using a Dremel tool and diamond bit or hand extracted under a microscope from specimens. All measured sulfur isotope values are reported in standard $\delta^{34}S$‰ notation (in per mil, ‰) relative to Vienna Canyon Diablo Troilite (VCDT) standard.

Sulfur isotopic data for 16 pyrite, 16 galena, 11 sphalerite, and 5 chalcopyrite samples are illustrated on a histogram plot (fig. 31) and summarized in table 17. Appendix F presents the completed data set. Although the sulfur isotope data shows a wide variation, from -1 to 16‰, all but one sample vary within -1 to 5‰. The anomalous value is for a galena sample above 16‰.

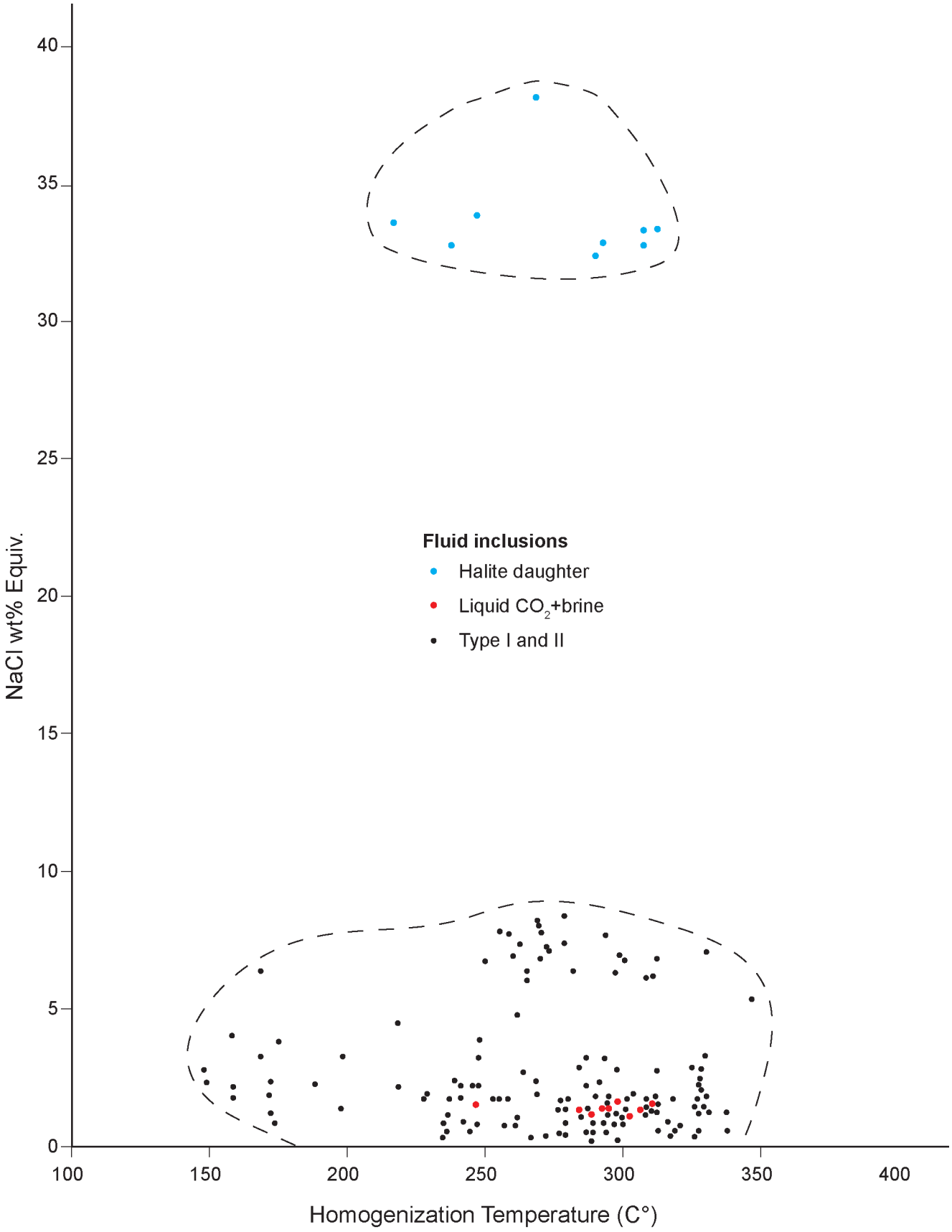

Figure 30. Salinity (NaCl wt% equiv.) versus homogenization temperature diagram for type I and II, three-phase CO_2 , and three-phase halite daughter fluid inclusions showing groups of low- and high-salinity fluids.

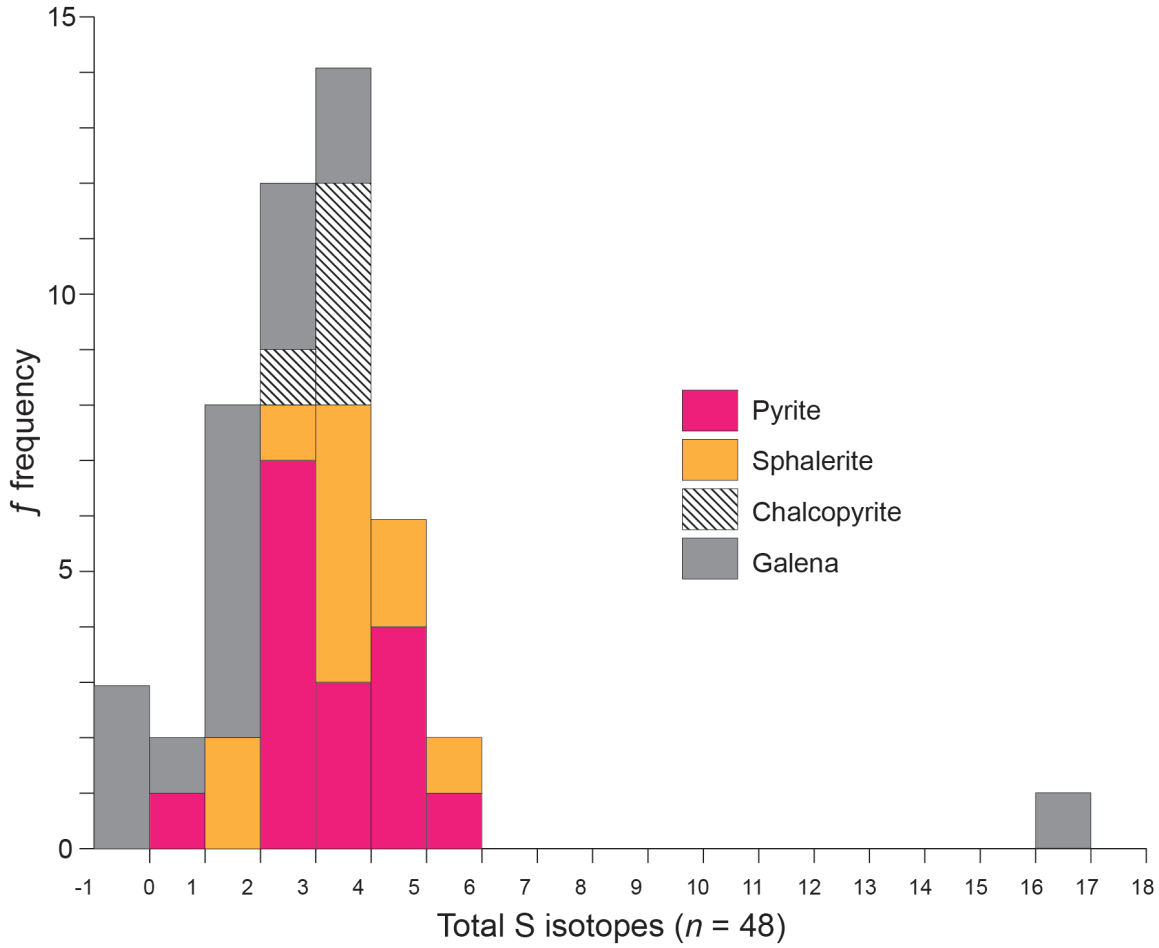

Figure 31. Histogram showing distribution of total sulfur isotopes for all phases.

Geothermometery was determined for isotope pairs from four locations using the methods of Ding and others (2003). Spahlerite–galena pairs, showing co-genetic relationships and physical evidence of being in equilibrium, were selected for geothermometry calculations. Isotopes from 11 different sphalerite–galena pairs used in the calculations represent the St. Anthony vein and the vein crossing the district sampled at the Big Four, Nickel Plate, and Attowa mines (summarized in appendix G). Results showed equilibrium temperatures ranging from 304.2ºC to 578.6ºC and averaging 429.8ºC. The two lower equilibrium temperatures (304.2ºC and 332.1ºC) overlap the higher fluid inclusion temperatures, which range from 306.9ºC to 347.5ºC.

Table 17. Summary of sulfur isotope analytical results.

Mineral	Number of Samples	$\delta^{34}S‰$ Range	$\delta^{34}S‰$ Average
Pyrite	16	0.7–5.2	3.3
Galena	16	-0.7–16.6	2.5
Sphalerite	11	1.0–5.0	3.3
Chalcopyrite	5	2.8–3.9	3.3

Note. Sulfur isotopes in parts per mil ($\delta^{34}S‰$).

OXYGEN ISOTOPES

Oxygen isotopes were determined for six quartz samples from five locations (table 18) within the most extensive and mineralized veins in the district (fig. 2). Selected samples represent clear to milky euhedral to anhedal quartz crystals and grains from sulfide–quartz veins of disseminated sulfides and silicified host rocks. Coarsely crushing slabs and hand specimens freed and separated the quartz crystals and grains, which were subsequently hand selected under a binocular microscope. The hand-picked 100 g of coarsely crushed quartz grains was powdered in a pulverizer as instructed by Geochron Laboratories.

The powdered samples were sent to Geochron Laboratories, Chelmsford, Massachusetts for isotope analysis. The laboratory procedure for extracting oxygen isotopes from the quartz powders used the CIF_3 method of Borthwick and Harmon (1982), quantitatively converting O_2 to CO_2 over hot graphite. The oxygen isotope measurements were performed using an Optima dual-inlet stable isotope mass spectrometer. The oxygen isotope results (table 18) are in the normal delta-notation relative to Vienna standard

mean ocean water (VSMOW).

Temperatures acquired from fluid inclusion data and sulfur isotope pairs from each sample site were used to calculate $\delta^{18}O$ for the hydrothermal fluids using quartz–water fractionation equations from Campbell and Larson (1998), Matthews and Beckinsale (1979), and Clayton and others (1972). Average temperatures used to calculate the hydrothermal fluid $\delta^{18}O$ composition for quartz veins from the Ajax, Nickel Plate, and State mines are from pressure-corrected fluid inclusion homogenization temperatures. Galena–sphalerite sulfur isotope pairs were used for the Big Four and Attowa mines temperatures.

The $\delta^{18}O_{H_2O}$ (‰) was calculated using the quartz–water fractionation equations from Campbell and Larson (1998) for measured fractionation between quartz and water. Fractionation equations from Matthews and Beckinsale (1979) were applied for temperatures ranging from 265º to 465ºC, and Clayton and others (1972) fractionation equations were used for temperatures ranging from 500º to 750ºC.

Oxygen isotope results for the quartz samples showed little variation between sampling sites along the strike of the vein represented by sample sites at the Big Four, Ajax, Nickel Plate, and Attowa mines (table 18). The vein mined at the State mine has the same oxygen isotope compositions as the vein represented by the other four mines. Calculating the oxygen isotope composition for the hydrothermal fluid using quartz–water fractionation equations showed a wide variation in isotope compositions (table 18). These compositions ranged from 6.8 to 9.0‰ for the main vein represented by Big Four, Ajax, Nickel Plate, and Attowa mines. The vein at the State mine also showed a similar wide variation ranging from 6.5 to 7.5‰.

DISCUSSION

All the veins in the Big Foot district hosted by the Butte Granite (fig. 2) developed after the granite solidified and fractured by tectonic forces. Age dating suggests the veins could be contemporaneous with a late-stage aplite intrusion that followed the emplacement of the Butte Granite. The granite hosting the veins crystallized at a depth of 7 to 8 km, as determined by hornblende barometric methods (Olsen and others, 2016). Age dating of the veins by $^{40}Ar/^{39}Ar$ methods yielded ages varying from 73.8 ± 0.12 to 75.3 ± 0.25 Ma (Olson and others, 2016), similar to the aplite dike zircon age of 74.5 ± 0.6 Ma (Korzeb and Scarberry, 2017). The similarities in ages suggest the veins developed from a hydrothermal system coeval with aplite intrusion and may have evolved from magmatic fluids originating from a cooling pluton at depth. The presence of schorl further suggests the early mineralizing fluids were saturated in boron, silica, and aluminum and may have had a magmatic source.

Similarities between ages of the veins and aplite intrusions indicate the initial magmatic fluids that developed the veins and deposited schorl could have originated from the same felsic pluton. Aplite intrusions hosted by the Boulder Batholith are known to be boron enriched, developing pegmatites with abundant schorl. Boron-enriched magmas could originate from the anataxis of boron-rich protoliths such as marine sediments (London and others, 2002). The original boron source for the aplite intrusions may have been marine sediments of the Proterozoic Belt Supergroup formations, which at some locations contain tourmalinites (Beaty and others, 1988; Slack, 1993) and underlie the Boulder Batholith (Harrison, 1972). Assimilation of Proterozoic Belt Supergroup formations into a magma could generate a boron-enriched felsic magma that was intruded as aplite and alaskite; this may be the mineralizing fluid source for the Big

Table 18. Oxygen isotope compositions for six quartz vein samples from the Big Foot mining district.

Sample	Location	Temperature (ºC)	$\delta^{18}O_{SMOW}$ (‰)	$\delta^{18}O_{H2O}$ (‰)
BF-4	Big Four mine	382.8	11.8	6.8
BF-8	Ajax mine	463.4	11.9	8.4
BF-12	Nickle Plate mine	503.5	11.2	9.0
BF-25	State mine	407.4	11.0	6.5
BF-27	State mine	419.5	11.8	7.5
BF-48	Attowa mine	449.6	12.3	8.6

Note. Temperature is in degrees centigrade; $\delta^{18}O_{SMOW}$ (‰), oxygen isotope composition for vein quartz; $\delta^{18}O_{H2O}$ (‰), calculated oxygen isotope composition for hydrothermal fluid. See figure 2 for sample locations.

Foot district. Boron, being an incompatible element, will exsolve along with water from the cooling magma (London and others, 2002), generating a boron-enriched magmatic-hydrothermal fluid. A magmatic-derived, boron- and silica-enriched hydrothermal fluid originating from a cooling magma could have invaded fractures currently occupied by the veins, depositing schorl and quartz along the vein margins, and silicified the host granite, which would generate silicic–illite alteration.

Wall-Rock Alteration

Four types of alteration occur in the granite host rock adjacent to the veins. These include propylitic, carbonate, silicic–illite, and argillic–illite identified by VNIR-SWIR spectroscopy, whole-rock analysis, and from thin sections and hand specimens. Propylitic alteration is not common and was identified at two locations, at the Big Major mine and St. Anthony mine. Propylitic alteration was overprinted by silicic–illite alteration throughout the district, which could account for its rarity. Carbonate alteration was found at one location, the Big Major mine. Silicic–illite alteration and argillic–illite alteration are the most prolific alteration types within the wall rock adjacent to all the veins throughout the district.

Two alteration types, identified as high temperature and low temperature by VNIR-SWIR spectroscopy, took place during vein development. High-temperature alteration, represented by silicic–illite alteration, developed by hydrothermal fluids silicifying and replacing the host granite with quartz. This took place during quartz vein mineralization. Following the silicic–illite alteration, low-temperature alteration developed argillic–illite alteration. This alteration overprinted the silicic–illite alteration and formed distal from the veins. The transition from silicic–illite alteration to argillic–illite alteration and overprinting of propylitic alteration implies a cooling hydrothermal system. Schorl, along with a variety of clay minerals present in the silicic–illite and argillic–illite alteration, indicate mineralization from a hydrothermal fluid with a variable pH.

Schorl precipitates from fluids with a pH below 6.5 and is unstable in alkali fluids with a pH above 7.0 (London, 2011). The presence of schorl and extensive silicification suggest the initial hydrothermal fluid was enriched in boron, aluminum, and silica with an acidic pH. The acidic boron–silica-enriched hydrothermal fluids altered the host granite. This released Al, Na, and K and led to schorl and quartz precipitation in open fractures, as well as the replacement of feldspar minerals with quartz and clay minerals. As alteration progressed from schorl deposition and quartz to K–illite, illite–smectite, dickite, montmorillonite, and muscovite alteration, the hydrothermal fluid began to neutralize, becoming less acidic (Simmons and others, 2005; Fournier, 1985). The presence of schorl and dickite is indicative of acidic pH conditions while K–illite and illite–smectite indicate a neutral pH environment (Hedenquist and others, 2000; Reyes, 1990).

Alteration of the host granite continued after silicic–illite alteration, generating a low-temperature argillic–illite alteration distal from the veins. The low-temperature hydrothermal fluid was less acidic than the high-temperature hydrothermal fluids and generated K–illite, illite–smectite, phengite, and kaolinite. Kaolinite is both well crystallized and poorly crystallized, suggesting a transition from late-stage hydrothermal conditions (well-crystallized kaolinite) to supergene weathering (poorly crystallized kaolinite). Supergene weathering generated ferrihydrite, jarosite, goethite, hematite, and poorly crystallized kaolinite.

The overprinting of propylitic alteration by argillic–illite alteration may be an indication of a cooling system. The high-temperature silicic–illite alteration overprinting propylitic alteration followed by cooler argillic–illite alteration indicates a drop in temperature as alteration was taking place. Two fluid inclusion homogenization temperature populations ranging from 140º to 200º C and 210º to 350º C further suggest a cooling system during vein and alteration development.

Pressure and Depth of Mineralization

The surface exposures of the Butte Granite in the Big Foot district are estimated to have crystallized at a depth of 7 to 8 km (Olson and others, 2016). Using a geobaric gradient of 3.5 km per kb, the lithostatic pressure would be approximately 2 to 2.3 kb. This lithostatic pressure is similar to the 2.1 to 2.4 kb pressure estimated for the crystallization of the Butte Granite from hornblende compositions (Anderson and Smith, 1995; Olson and others, 2016). Quartz vein lithostatic pressure was estimated from aqueous two-phase fluid inclusions and an average temperature from sulfur isotope geothermometry of sphalerite–galena pairs. By applying the average fluid inclusion homogenization temperature (270ºC) and average 2.6 wt% NaCl eq to a diagram in Roedder (1984), a fluid density of 0.75 g/cm^3 was estimated. The estimated fluid density (0.75 g/cm^3) and average sulfur isotope geothermometry temperature (430ºC) were applied to a pressure temperature diagram from Fisher (1976). That yielded a lithostatic pressure of 2 kb for quartz vein mineralization. This pressure is close to the pres-

sure determined by Olson and others (2016) from the Butte Granite hornblende compositions and calculated from the crystallization depth.

Vein Formation Temperature

The average two-phase fluid inclusion temperature (270ºC) is 160ºC lower than the average sulfur isotope geothermometry temperature (430ºC). There is little evidence for boiling and all inclusions homogenized to liquid, and this suggests trapping above the liquid–vapor curve in the one-phase field. Differences in the fluid inclusion homogenization temperatures and sulfur isotope geothermometry temperatures could be attributed to the lack of boiling during sulfide mineralization.

An isobaric correction needs to be applied to the homogenization temperatures to obtain the true fluid inclusion trapping temperatures. The upper pressure is constrained by the depth of crystallization of the Butte Granite at 2.3 kb. A fluid density of 0.75 g/cm^3 was determined from average salinity and Th for two-phase fluid inclusions. By applying the fluid density and lithostatic pressure to a pressure density diagram from Fisher (1976), a temperature correction of 160ºC was determined. Applying the 160ºC correction yielded an inferred fluid trapping temperature ranging from 310ºC to 508ºC with an average of 430ºC. This pressure-corrected fluid inclusion temperature range overlaps the sulfur isotope, equilibrium temperatures, which range from 304ºC to 579ºC.

Trace Elements

Anomalous concentrations of trace elements from the veins and altered rocks consist of Au, Ag, As, Cd, Co, Cu, Pb, Sb, Mn, Mo, and Zn. The trace elements Ag, As, Pb, Sb, and Zn are characteristic of epithermal systems and active geothermal vents (Weissberg, 1969; Silberman and Berger, 1985; Ewers and Keays, 1977; Simmons and Browne, 2000; Simmons and others, 2016). The other trace elements, including Au, Cd, Co, Cu, Mn, and Mo, are not characteristic of epithermal vein systems but are reported from active geothermal fields, precipitates, and sulfide minerals in modern volcanic back arc environments (Fouquet and others, 1993; Berkenbosch and others, 2012; Simmons and others, 2016). In addition to epithermal systems, the Big Foot trace element suite is also characteristic of porphyry systems (Halley and others, 2015). The trace elements and boron represented by schorl from the Big Foot veins could result from a hydrothermal fluid derived from a magmatic source.

The trace elements, As, Ag, Cd, Cu, Pb, Sb, and Zn, are the most anomalous compared to unaltered granite. These elements could have been sourced from either the host granite by circulating meteoric water or a hydrothermal-magmatic-derived fluid. Based on the depth of vein formation (7 to 8 km), trace element content, fluid inclusions and stable isotopes, the hydrothermal fluid was derived from a magmatic source and not from circulating meteoric water. The trace elements B, As, Cu, Pb, Sb, and Zn are enriched in hydrothermal fluids sourced from volcanic arc subduction-derived magmas (Noll and others, 1996). The same trace element suite from the Big Foot veins also occurs in subduction-derived magmas, and this implies a magmatic-hydrothermal fluid source for the Big Foot trace element suite. Trace element content, fluid inclusions, and stable isotopes from the epithermal polymetallic deposit of Cerro de Pasco, Peru, indicates a magmatic origin for this deposit (Rottier and others, 2018). Compared to the polymetallic Cerro de Pasco, Peru deposit, the Big Foot veins have similar anomalous trace elements, fluid inclusions, and stable isotopes. This further implies a magmatic trace element source for the Big Foot veins.

Sulfide-Quartz Vein Genesis

Fluid inclusion data, sulfur isotope equilibrium temperatures, and lithostatic pressure evidence suggest the veins exposed on the surface in the Big Foot district represent the deep roots of an inferred epithermal system. Fluid inclusion temperatures for two-phase fluid inclusions, corrected for pressure, range from 310ºC to 508ºC with an average of 430ºC, and salinities range from 0.2 to 8.4 with an average of 2.6 wt% NaCl eq. Three-phase fluid inclusions with a halite daughter mineral have pressure-corrected homogenization temperatures averaging 436ºC, with a range of 377ºC to 474ºC, an average salinity of 33.6 wt% NaCl eq, with a range of 32.6 to 38.1 wt% NaCl eq. Three-phase CO_2 inclusions that generated clathrate have an average pressure-corrected homogenization temperature of 452ºC with a range of 407ºC to 472ºC. These have an average salinity of 1.4 wt% NaCl equivalent with a range of 1.2 to 1.6 wt% NaCl eq. Lithostatic pressure and fluid inclusion data suggest the vein quartz started crystallizing from a high-temperature, hydrothermal fluid with low to high salinities similar to those measured in deep porphyry systems (Rusk and others, 2008; Reed and others, 2013).

Single-phase magmatic-hydrothermal fluids rise in pulses as over-pressure waves from cooling plutons (Monecke and others, 2018). Pressures intermittently exceeding lithostatic pressures within the upward-

moving pulses cause microfracturing of the host rock with the passing of each over-pressure wave, increasing host rock permeability. Monecke and others (2018) suggest with the passing of each over-pressure wave, early formed quartz will go into dissolution, and when pressure drops to lithostatic conditions, quartz will precipitate and recrystallize overprinting the early quartz phases. The cathodoluminescence (CL) patterns and textures found in the cores of early quartz crystals suggest the Big Foot veins formed during fluctuating pressure events. The passage of multiple pressure waves will create a stockwork of early quartz veins in the host rock and reopen earlier-formed veins (Monecke and others, 2018).

Textures revealed by Cl response of primary quartz grains remaining within the altered host granite show extensive microfracturing and brecciation. The microfractures are filled with quartz that give a black to dark gray CL response. This microfracturing may have been caused by pulses of over-pressured fluids exceeding lithostatic pressure followed by pressure drops to lithostatic conditions and quartz precipitation. Along with quartz, schorl also fills microfractures, which does not give a CL response.

Cathodoluminescence of the quartz veins shows six quartz generations and two episodes of microbreccia generation and microfracturing of primary quartz grains in the host granite. Each quartz generation represents pressure and temperature changes that took place during vein development. The first two quartz generations took place at high temperatures (≥500ºC) and fluctuating lithostatic pressures. The cores of these crystals show CL patterns consisting of bright to black responding grains and grains with dark oscillatory growth bands showing evidence of dissolution along the grain boundaries. The early quartz generations formed euhedral crystals in open spaces and crystallized at the same time as schorl. When schorl is present, quartz is included with schorl crystals resembling needles. Early quartz with schorl inclusions suggest the quartz precipitated at similar acidic pH, high temperatures, and lithostatic pressure required for schorl crystallization.

The first quartz generation might have precipitated from cooling magmatic-hydrothermal fluids ascending from a cooling pluton. Pressure fluctuations as well as temperature influenced the precipitation of the first quartz generations. Dissolution and recrystallization textures revealed by Cl response indicate the first quartz generation went into dissolution after crystallization and was later replaced by a second generation. Fluid pressures exceeding lithostatic pressure could cause dissolution of an early quartz phase back into the magmatic-hydrothermal fluids (Monecke and others, 2018). When pressures return to lithostatic conditions or lower, quartz will reprecipitate over the partially dissolved first quartz generation. These periodic changes between lithostatic pressures may have taken place when the Big Foot veins crystallized and are recorded by quartz textures revealed by CL responses.

A third quartz generation with oscillating growth bands revealed by CL response occurs as an overgrowth on early stage one and two quartz crystals. The quartz overgrowths could have precipitated from a rising and cooling single-phase, magmatic-hydrothermal fluid at lithostatic conditions. Monecke and others (2018) suggest that during cooling of a hydrothermal fluid, pressure conditions may fluctuate and decompression to hydrostatic or lower pressure conditions may occur. This decompression and cooling of the hydrothermal fluid would cause further quartz precipitation. During decompression to hydrostatic conditions, brittle fracturing of the early formed quartz veins could take place (Monecke and others, 2018).

Two microbrecciation events took place during vein development. One event brecciated the host granite and another brecciated the quartz veins. The host granite underwent microbrecciation, which generates open spaces and fractures. This allowed quartz veinlets to develop, feldspar replacement by quartz and clay minerals, and schorl to crystallize from invading hydrothermal fluids. After the third quartz generation precipitated, brittle fracturing generated microbreccias in the early quartz veins. A fourth quartz generation giving a black to dark gray CL response filled fractures and open spaces generated by microbrecciation of the early stage quartz crystals. A fifth quartz generation gave a low to white CL response, displaying oscillating growth bands, crystallized with sulfide minerals in open spaces generated by microbrecciation. Equilibrium temperatures determined from sulfur isotope pairs indicate sulfide mineralization and microbrecciation took place over a wide temperature range (304º to 579ºC). Monecke and others (2018) noted pressure changes from lithostatic to hydrostatic take place at wide temperature ranges (≈350ºC to ≈500ºC) and pressures up to 2 kb for a deep porphyry system that is similar to the Big Foot vein temperatures and pressures. When lower lithostatic pressure conditions are reached, temperatures are typically below ≈350ºC (Monecke and others, 2018), and this is reflected in lower fluid inclusion homogenization and sulfur isotope equilibrium tempera-

tures for the Big Foot quartz veins.

Quartz precipitation during and after brecciation most likely took place during a transition from lithostatic to stable lower pressure conditions over a wide temperature range. Microbrecciation of the early quartz phases allowed a rising magmatic-hydrothermal fluid to circulate throughout the vein system. Cooling of a circulating magmatic-hydrothermal fluid could lead to quartz and sulfide precipitation (Monecke and others, 2018). As the hydrothermal fluids cooled, quartz solubility decreased. This resulted in the precipitation of a fourth quartz phase with sulfide minerals filling fractures and open spaces.

Mineralization takes place as low-salinity hydrothermal fluids of the lithostatic environment transition into the lower pressure hydrostatic realm during brittle fracturing in deep porphyry systems (Monecke and others, 2018). Sulfur isotope equilibrium and pressure-corrected fluid inclusion temperatures indicate that Big Foot vein sulfide mineralization started under lithostatic conditions at high temperatures. Sulfide and vein quartz mineralization continued as decompression and cooling of the magmatic-hydrothermal fluid occurred during microbrecciation of the early quartz generations. Decompression of the hydrothermal fluid may have taken place during exhumation of the Butte Granite by erosion of the overlying Elkhorn Volcanic sequence.

At the close of vein development, a sixth quartz generation filling remaining open spaces precipitated, giving a low, even CL response. Textures revealed by CL response indicate this final quartz generation did not undergo fracturing or brecciation and was not subject to fluid decompression. This quartz generation precipitated after sulfide mineralization and crystallized at low temperatures below 300ºC at low-pressure or hydrostatic conditions. The sixth quartz generation could have crystallized at a shallower pressure, representing hydrostatic conditions caused by exhumation of the Butte Granite during vein development.

Sulfur isotopes from the quartz veins range from -0.7‰ to 16.6‰. All the samples fall within the -0.7‰ to 5.2‰ range with the exception of one galena sample, with a $\delta^{34}S$ value of 16.6‰. The sulfur isotope range suggests the veins developed from a magmatic-hydrothermal fluid enriched in heavy sulfur sourced from crustal rocks assimilated into a felsic pluton. Granitic magmas acquire most of their sulfur during emplacement from crustal sources (Ohmoto, 1986). Granitoid magmas become enriched in crustal sulfur by bulk assimilation of country rocks and selective assimilation of sulfur (Ohmoto, 1986). Acidic igneous rocks not influenced by crustal sources are expected to have a $\delta^{34}S$ composition of 0 ± 3‰ (Ohmoto and Rye, 1979). The range of $\delta^{34}S$ found in the Big Foot veins extends to 16‰, suggesting a magmatic-hydrothermal fluid source influenced by crustal rocks. Proterozoic and Phanerozoic marine evaporates, which have a $\delta^{34}S$ range of 10‰ to 35‰, could be a crustal source for heavy sulfur (Claypool and others, 1980). Isotopically heavy marine sulfate assimilated into a magma could cause $\delta^{34}S$ enrichment of the magmatic-hydrothermal fluids exsolved from a source pluton (Field and others, 2005).

The regional extent of the Belt Supergroup shows a spatial relationship, suggesting it underlies the Boulder Batholith (Harrison, 1972) and that it is the most likely source for heavy sulfur assimilated into the Boulder Batholith intrusions. The Newland Formation has diagenetic pyrite with $\delta^{34}S$ values ranging from -8.7‰ to 36.7‰ (Lyons and others, 2000). Strauss and Schieber (1990) inferred that baryte with $\delta^{34}S$ values of 13.6‰, 14.4‰, and 18.3‰ replaced gypsum. Field and others (2005) suggest the Belt Supergroup could serve as a potential source for heavy sulfur in the Butte district veins. The heavy sulfur was derived from the quartz porphyry magma that assimilated Belt Supergroup rocks. When Belt Supergroup heavy sulfur is combined and equilibrated with magmatic sulfur, the $\delta^{34}S_{\Sigma S}$ is raised from a magmatic value of 0‰ to 10‰ (Field and others, 2005). The $\delta^{34}S$ from the Big Foot veins could have originated from magmatic-hydrothermal fluids exsolved from a pluton that assimilated underlying Belt Supergroup rocks. This pluton intruded the Butte Granite at depth, similar to the pluton that formed the Butte district porphyry deposit.

Oxygen isotopes for the quartz veins range from 11.0‰ to 12.3‰. Calculated oxygen isotopes for the hydrothermal fluids range from 6.5‰ to 9.0‰ (table 11). These findings suggest a granitoid magmatic origin for the hydrothermal fluids that precipitated the vein quartz (Ohmoto, 1986). For I-type granitoids, $\delta^{18}O$ values fall between 6‰ and 8‰ (Ohmoto, 1986), similar to the calculated hydrothermal fluid $\delta^{18}O$ range. The vein quartz $\delta^{18}O$ values fall between the S-type granitoid range of 8‰ and 12‰ (Ohmoto, 1986). An implication of the $\delta^{18}O$ values is that the magmatic fluids originated from an I-type granitoid pluton that assimilated crustal rocks. This imparted an S-type $\delta^{18}O$ signature to the vein quartz.

Oxygen isotopes further imply the veins crystallized from a magmatic-hydrothermal fluid. This fluid exsolved from a pluton that assimilated underlying Belt Supergroup rocks. The average $\delta^{18}O$ value for

the Ravalli Group is 12‰ (Rye and others, 1984), with values of 11.3‰ to 13.0‰ determined for the Revett Formation of the Belt Supergroup (Lange and Sherry, 1986). The Belt Supergroup rock $\delta^{18}O$ values reflect the $\delta^{18}O$ measurements for marine sediments (10‰ to 22‰) reported by Campbell and Larson (1998). The partial melting of marine sediments assimilated into a pluton could generate an exsolved magmatic fluid with an S-type $\delta^{18}O$ signature similar to the Big Foot quartz veins.

Rusk and others (2008) propose that low-salinity, CO_2-bearing fluids derived from a magmatic source provided the mineralizing fluids for the Butte porphyry copper deposit. Low-salinity, CO_2-bearing fluid inclusions present in the Big Foot veins could likewise be an indication the veins were mineralized from a magmatic-derived, low-salinity, CO_2-bearing hydrothermal fluid similar to that in the Butte district. The initial magmatic-hydrothermal fluid that formed the veins and altered the host granite was probably CO_2 enriched and acidic. Pressure-corrected fluid inclusion temperatures and sulfur isotope geothermometry suggest fluid temperatures varied from 310ºC to 579ºC and calculated lithostatic pressure ranged up to 2 kb.

During vein development, the magmatic-hydrothermal fluid underwent physical and chemical changes caused by fluctuating pressures and temperatures and wall-rock reactions. These physical and chemical changes led to quartz precipitation and sulfide mineralization. There is little evidence of boiling during vein development, but separation from a low- to high-salinity fluid occurred as noted at five vein locations. The initial magmatic-hydrothermal fluid may have changed from a high-temperature (≥500ºC), low-salinity (1.2 to 1.6 wt% NaCl eq), CO_2-bearing fluid to an intermediate-temperature (≤500ºC), moderate to low-salinity (0.2 to 8.4 wt% NaCl eq), CO_2-deficient fluid by decompression from lithostatic to lower pressure conditions. Rapid decompression of a magmatic-hydrothermal fluid from lithostatic to hydrostatic conditions will lead to a decrease in temperature (Monecke and others, 2018) and could result in the loss of CO_2 and increase in salinity, similar to a boiling event. The loss of CO_2 from a hydrothermal fluid can change the pH from acidic to alkali (Reed and Palandri, 2006). A shift in pH to alkali and dropping temperatures will cause sulfide precipitation to take place (Reed and Palandri, 2006). Microbreccias hosting sulfide minerals developed in the Big Foot veins, implying rapid decompression of the magmatic-hydrothermal fluids after the first three quartz generations crystallized. Rapid decompression of the hydrothermal fluids resulted in a temperature drop, a change to low-pressure conditions, and loss of CO_2 that shifted the pH to basic. These changes resulted in the precipitation of sulfide minerals.

After vein development, minor to intense supergene alteration generated a variety of secondary minerals. In contrast to the other veins in the district, the vein at the Mountain Queen mine experienced intense supergene alteration, with few primary sulfide minerals remaining intact. The breakdown and oxidation of primary minerals by groundwater generated abundant secondary minerals found at the Mountain Queen mine. These minerals consist of iron–lead–antimony oxides, lead and copper carbonates, a copper silicate, a lead phosphate, copper–iron–lead sulfates, and lead and iron arsenates. The sulfur and arsenic, probably leached from the primary sulfide minerals by acidic ground water, was transported to locations with conditions that favored mineral precipitation. Pyromorphite, a lead phosphate, is the most abundant secondary mineral at the Mountain Queen mine. To generate this mineral, lead was most likely leached from the vein while phosphorus was sourced from the altered host granite and transported by groundwater to favorable precipitation sites.

GEOLOGIC MODEL

A geologic model for the Big Foot mining district is based on data generated by this investigation, past geophysical data, and geologic mapping. The veins are hosted by the Butte Granite, which crystallized at a depth of 7 to 8 km (Olson and others, 2016). The Butte Granite is 74.5 ± 0.9 to 76.28 ± 0.14 Ma as dated by Lund and others (2002) and Martin and others (1999). The veins were dated at 73.81 ± 0.12 to 75.2 ± 0.25 Ma by Olson and others (2016). Following emplacement of the Butte Granite, aplite dikes were intruded into the granite at 74.5 ± 0.6 Ma (Korzeb and Scarberry, 2017). Age dating suggests the veins were emplaced at the same time as aplite intrusive events.

Age dating of the veins by Olson and others (2016) show they formed about 1 million years after the host granite crystallized, implying the veins were emplaced at the same depth as the granite host. The veins now exposed at the surface formed at a lithostatic pressure of 2 kb, reflecting the 7- to 8-km depth of the host granite, with temperatures varying from 310ºC to 579ºC. The lithostatic pressure and temperature suggest the veins represent the exhumed deep roots of an epithermal system. Based on the depth of formation, lithostatic pressure, and temperature, the veins fit the mesothermal classification based on the model from Ridge (1972).

Age dating, trace element, isotopic, and fluid inclusion evidence suggest a magmatic fluid source for the veins. Timing of vein emplacement implies that magmatic fluids were sourced from a magma with a felsic composition. Schorl is known to have crystallized from boron-enriched aplites within the Boulder Batholith. Magmatic-hydrothermal fluids generated from a boron-enriched felsic magma will likewise be enriched in boron and could crystallize schorl during alteration of the host granite along the vein contacts. Anomalous trace elements found in the veins and altered host rock consisting of As, Cu, Pb, Sb, Zn, and B implied schorl crystallization; these are known to be enriched in volcanic arc subduction-derived magmas (Noll and others, 1996). This suggests the fluids that developed the Big Foot veins may have a subduction-derived magmatic origin. Pressure-corrected fluid inclusions indicate the veins started to crystallize at temperatures above 500ºC, from CO_2-enriched mineralizing fluids with a variable salinity from 0.2 to 38.1 wt% NaCl eq. The presence of three-phase CO_2-enriched inclusions, and pressure-corrected homogenization temperatures exceeding 500ºC, further suggest the initial mineralizing fluids had a magmatic origin. Likewise, sulfur isotope equilibrium temperatures exceeding 500ºC also imply crystallization from a high-temperature magmatic-hydrothermal fluid.

The largest sulfide–quartz vein and most aplite dikes correlate with a magnetic low located in the northeast area of the district (figs. 2, 3). A smaller magnetic low correlates with the vein at the St. Anthony mine. These magnetic lows interpreted by Hanna and others (1994) are related to a pluton that altered the Butte Granite, and they are similar to the magnetic lows in the Butte district. The correlation of the aplite dikes and sulfide quartz vein with the magnetic anomaly implies the veins and aplite dikes share a common felsic pluton source.

Quartz textures revealed by CL response provide additional evidence that the Big Foot veins may have originated from mineralizing fluids derived from a cooling pluton intruded into the Butte Granite. As the magmatic-hydrothermal fluids ascended through fractures in the Butte Granite, they began altering the granite and initiated quartz crystallization on the fracture margins. From quartz textures, it appears the veins underwent pressure changes of varying lithostatic conditions. Quartz that precipitated during initial vein development shows evidence of dissolution, reprecipitation, and microfracturing caused by fluctuating pressure changes from above lithostatic conditions and returning to lower lithostatic conditions. These fluctuating pressure changes could have taken place during vein exhumation as the overlying Elkhorn volcanic sequence was eroded. Monecke and others (2018) suggest fluid sourced from a pluton rises in pulses that intermittently exceed lithostatic conditions. This causes microfracturing in the host rock and increases permeability. This microfracturing and brecciation is found in the quartz veins and host granite throughout the Big Foot district. These fluctuating pressure conditions imply a plutonic source for the hydrothermal fluids that precipitated the Big Foot veins.

EXPLORATION POTENTIAL

The northern and southern part of the Big Foot mining district may have exploration potential for a deep-seated porphyry or stockwork vein system. Based on the results from this study, the veins classified as mesothermal might be related to a magmatic source. Magmatic-hydrothermal fluids sourced from a pluton intruded into the Butte Granite, or a cupola formed during cooling of the Butte Granite pluton, may have supplied the metals that developed the veins. Although speculative, there could be a deep-seated porphyry or stockwork vein system underlying the district. Elliott and others (1993) ranked the district as high potential for the occurrence of porphyry and/or stockwork deposits of copper, molybdenum, and tungsten or stockwork and disseminated gold and silver deposits.

Hanna and others (1994) identified a magnetic low covering 60 km^2 in the Butte Granite in the northeast part of the district. The anomaly encompasses the Big Four, Nickel Plate, Ajax, and Attowa mines and a major vein extending to the center of the anomaly (figs. 2, 3). A smaller magnetic low in the southwest part of the district identified by Hanna and others (1994) lies northwest of the St Anthony mine. It extends 4 km northwest of the mine and covers 4 km^2. Hanna and others (1994) interpreted these magnetic lows in the Butte Granite as caused by altered intrusions in the granite, similar to those found in the Butte mining district. However, the two magnetic lows in the Big Foot district are smaller than the one in the Butte district. The Butte district anomaly covers 120 km^2 and the Big Foot district anomalies cover a total of 64 km^2. The Big Foot district anomalies are associated with a clustering of aplite and alaskite dikes and intrusions mapped by Olson and others (2016; fig. 3). These clusters of dikes and intrusions might be sourced from an underlying pluton related to the magnetic low anomaly or during cooling of the Butte Granite.

High-sulfidation epithermal veins, and mesothermal veins in deep systems, are known to be related to porphyry systems (Chang and others, 2011; Cook and Bloom, 1990; Sillitoe, 2010). A relationship between the Butte district porphyry system and associated polymetallic veins is well documented (Dilles and others, 1999; Rusk and others, 2008; Reed and others, 2013; Houston and Dilles, 2013). Likewise, the Big Foot district veins could be related to a deep porphyry system or to a stockwork vein system in the vicinity of the two magnetic lows identified by Hanna and others (1994). The Big Foot district veins have some similarities to the early Ag-Au-polymetallic veins that occur in the Butte district. Lund and others (2018) dated the Ag-Au-polymetallic veins to be 73 to 70 Ma, making them the oldest veins in the Butte district. Lund and others (2018) suggest the genesis of these early veins are hydrothermal fluids related to the emplacement of plutons in the Boulder Batholith. Veins with similar ages to the oldest veins in the Butte district are found in the Basin and Boulder districts, and these may have a genetic relationship with plutons in the Boulder Batholith (Lund and others, 2018). The ages of the veins in the Big Foot district are also similar to those in the Basin and Boulder districts and early veins in the Butte district; the Big Foot veins may likewise be related to a pluton emplaced in the Boulder Batholith.

There is supporting geologic, geophysical, trace element, isotope, quartz textures, and fluid inclusion evidence suggesting the Big Foot district veins formed from a magmatic-hydrothermal fluid, which originated from an underlying pluton or cupola in the Butte Granite. Evidence further suggests the magmatic-hydrothermal fluid source could also be related to a porphyry or stockwork vein system, and this could be determined by deep drilling and detailed geophysical surveys. Exploration for a porphyry system in the Big Foot district will require targeting the two magnetic lows identified by Hanna and others (1994) with detailed geophysical surveys followed by a deep drilling program. The veins themselves may not be viable exploration targets for polymetallic lodes because they appear to represent the roots of an epithermal system with one mineralizing event, and economic lode deposits may not extend beyond the currently mined depths. Deeper mineralization of a Cu-Mo porphyry system may extend below the mesothermal veins.

ACKNOWLEDGMENTS

I extend a special thanks to the patented claim owners who granted permission to enter and sample the mines and prospects on their properties. This study would not have been possible without their cooperation and help. A special thank you is due Gnanou Hamadou, who conducted the fluid inclusion analysis when he was a graduate student at the Department of Geological Engineering, Montana Tech of the University of Montana. I would like to thank Kaleb Scarberry of the MBMG, whose comments and suggestions improved the final manuscript. I thank George Brimhall, Clementine Exploration LLC, and Robert Houston, Oregon Department of Geology and Mineral Industries, whose reviews and comments greatly improved the manuscript. Cartography and graphic work by Susan Smith, MBMG; editing and layout by Susan Barth, MBMG.

REFERENCES

Anderson, J., and Smith, D., 1995, The effect of temperature and $f\ O_2$ on the Al-hornblende barometer: American Mineralogist, v. 80, p. 549–559.

Beaty, D.W., Hahn, G.A., and Threlkeld, W.E., 1988, Field, isotopic, and chemical studies of tourmaline-bearing rocks in the Belt-Purcell Supergroup: Genetic constraints and exploration significance for Sullivan type ore deposits: Canadian Journal of Earth Science, v. 25, p. 392–402.

Berger, B.R., Hildenbrand, T.G., and O'Neill, J.M., 2011, Control of Precambrian basement deformation zones on emplacement of the Laramide Boulder Batholith and Butte mining district, Montana, United States: U.S. Geological Survey Investigations Report 2011-5016, 29 p.

Berkenbosch, H.A., de Ronde, C.E.J., Gemmell, J.B., McNeill, A.W., and Goemann, K., 2012, Mineralogy and formation of black smoker chimneys from Brothers submarine volcano, Kermadec arc: Economic Geology, v. 107, p. 1613–1633.

Borthwick, J., and Harmon, S.R., 1982, A note regarding ClF_3 as an alternative to BrF_5 for oxygen isotope analysis: Geochimica et Cosmochimica Acta, v. 46, p. 1665–1668.

Campbell, A.R., and Larson, P.B., 1998, Introduction to stable isotope applications in hydrothermal systems, *in* Richards, J.P., and Larson, P.B., eds., Techniques in hydrothermal ore deposits geology: Reviews in Economic Geology, Society of Economic Geologists, v. 10, p. 173–193.

Chang, Z., Hedenquist, J.W., White, N.C., Cooke, D.R., Roach, M., Deyell, C.L., Garcia, J. Jr., Gemmell, J.B., Stafford, M., and Cuison, L. 2011, Exploration tools for linked porphyry and epithermal deposits: Example from Mankayan intrusion-

centered Cu-Au district, Luzon, Philippines: Economic Geology, v. 106, p. 1365–1398.

Claypool, G.E., Holser, W.T., Kaplan, I.R., Saki, H., and Zak, I., 1980, The age curves of sulfur and oxygen isotopes in marine sulfate and their mutual interpretations: Chemical Geology, v. 28, p. 199–260.

Clayton, R.N., O'Neil, J.R., and Mayeda, T.K., 1972, Oxygen isotope exchange between quartz and water: Journal of Geophysical Research, v. 77, p. 3057–3067.

Darling, R.S. 1991, An extended equation to calculate NaCl contents from final clathrate melting temperatures in H_2O-CO_2-NaCl fluid inclusions: Implications for P-T isochore location: Geochimica et Cosmochimica Acta, v. 55, p. 1869–1871.

Dilles, J., Reed, M., Roberts, S., and Houston, R., 1999, Early magmatic-hydrothermal features related to porphyry copper mineralization at Butte, Montana: Geological Society of America Abstracts, National meeting, v. 31 p. A380.

Ding, T., Zhang, C., Wan, D., Liu, Z., and Zhang, G., 2003, An experimental calibration on sphalerite-galena sulfur isotope geothermometer: Acta Geologica Sinica, v. 77, no. 4, p. 519–521.

Dudás, F.O., Ispolatov, V.O., Harlan, S.S., and Snee, L.W., 2010, $^{40}Ar/^{39}Ar$ geochronology and geochemical reconnaissance of the Eocene Lowland Creek volcanic field, west-central Montana: Journal of Geology, v. 118, p. 295–304.

Elliott, J.E., Wallace, C.A., Lee, G.K., Antweiler, J.C., Lidke, D.J., Rowan, L.C., Hanna, W.F., Trautwein, C.M., Dwyer, J.L., and Moll, S.H., 1993, Maps showing mineral resource assessment for porphyry and stockwork deposits of copper, molybdenum, and tungsten and for stockwork and disseminated deposits of gold and silver in the Butte 1º x 2º quadrangle, Montana: U.S. Geological Survey Miscellaneous Investigations Series Map I-2050-F, 30 p., scale 1:250,000 and 1:500,000.

Ewers, G.R., and Keays, R.R., 1977, Volatile and precious metal zoning in the Broadlands geothermal field, New Zealand: Economic Geology, v. 72, p. 1337–1354.

Feely, T.C., 2003, Origin and tectonic implications of cross-strike geochemical variations in the Eocene Absaroka Volcanic Province, United States: Journal of Geology, v. 111, p. 329–346.

Field, C.W., Zhang, L., Dilles, J.H., Rye, R.O., and Reed, M.H., 2005, Sulfur and oxygen isotopic record in sulfate and sulfide minerals of early, deep mainstage porphyry Cu-Mo and late mainstage base-metal mineral deposits, Butte district, Montana: Chemical Geology, v. 215, p. 61–93.

Fisher, J.R., 1976, The volumetric properties of H_2O, a graphical portrayal: Journal of Research U.S. Geological Survey v. 4, no. 2, p. 189–193.

Fouquet, Y., Stackelberg, U.V., Charlou, J.L., Erzinger, J., Herzig, P.M., Mühe, R., and Wiedicke, M., 1993, Metallogenesis in back-arc environments: The Lau basin example: Economic Geology, v. 88, p. 2154–2181.

Fournier, R.O., 1985, The behavior of silica in hydrothermal solutions, *in* Berger, B.R., and Bethke, P.M., eds., Geology and geochemistry of epithermal systems: Reviews in Economic Geology, Society of Economic Geologists, v. 2, p. 45–61.

Grant, J.A., 2005, Isocon analysis: A brief review of the method and applications: Physics and Chemistry of the Earth, v. 30, p. 997–1004.

Halley, S., Dilles, J.H., and Tosdal, R.M., 2015, Footprints: Hydrothermal alteration and geochemical dispersion around porphyry copper deposits: Society of Economic Geologists Newsletter, no. 100, p. 1, 12–17.

Hanna, W.F., Hassemer, J.H., Elliott, J.E., Wallace, C.A., and Snyder, S.L., 1994, Maps showing gravity and aeromagnetic anomalies in the Butte 1º x 2º quadrangle, Montana: U.S. Geological Survey Miscellaneous Investigations Series Map I-2050-I, 35 p., scale 1:250,000 and 1:500,000.

Harrison, J.E., 1972, Precambrian Belt Basin of northwestern United States: Its geometry, sedimentation, and copper occurrences: Geological Society of America Bulletin, v. 83, p. 1215–1240.

Hedenquist, J.W., Arribas R.A., and Gonzalez-Urien, E., 2000, Exploration for epithermal gold deposits, *in* Hagemann, S.G., and Brown, P.E., eds., Gold in 2000: Society of Economic Geologists, Reviews in Economic Geology, v. 13, p. 245–277.

Houston, R.A., and Dilles, J.H., 2013, Structural geologic evolution of the Butte district, Montana: Economic Geology, v. 108, p. 1397–1424.

Klepper, M.R., Weeks, R.A., and Ruppel, E.T., 1957, Geology of the southern Elkhorn Mountains, Jefferson and Broadwater Counties, Montana: U.S. Geological Survey Professional Paper 292, 82 p.

Korzeb, S.L., and Scarberry, K.C., 2017, Timing of pluton emplacement and mineralization of the Boulder Batholith: Proceedings, Montana Mining

and Mineral Symposium, October 11–October 14, 2017: Montana Bureau of Mines and Geology Open-File Report 699, p. 39–44.

Kuwatani, T., Yoshida, K., Ueki, K., Oyanagi, R., Uno, M., and Akaho, S., 2020, Sparse isocon analysis: A data-driven approach for material transfer estimation: Chemical Geology, v. 532, article 119345, in progress.

Lange, I.M., and Sherry, R.A., 1986, Nonmassive sulfide deposits in the late Precambrian Belt Supergroup of western Montana, *in* Roberts, S.M., Belt Supergroup: A guide to Proterozoic rocks of western Montana and adjacent areas: Montana Bureau of Mines and Geology Special Publication 94, p. 269–278.

Large, R.R., Gemmell, J.B., and Paulick, H., 2001, The alteration box plot: A simple approach to understanding the relationship between alteration mineralogy and lithogeochemistry associated with volcanic-hosted massive sulfide deposits: Economic Geology, v. 96, p. 957–971.

London, David, 2011, Experimental synthesis and stability of tourmaline: A historic overview: Canadian Mineralogists, v. 49, p. 117–136.

London, D., Morgan VI, G.B., and Wolf, M.B., 2002, Boron in granitic rocks and their contact aureoles, *in* Grew, E.S., and Anovitz, L.M., eds., Boron mineralogy, petrology and geochemistry: Reviews in Mineralogy, Mineralogical Society of America, v. 33, p. 299–330.

Lund, K., Aleinikoff, J.N., Kunk, M.J., Unruh, D.M., Zeihen, G.D., Hodges, W.C., Du Bray, E.A., and O'Neill, J.M., 2002, SHRIMP U-Pb and $^{40}Ar/^{39}Ar$ age constraints for relating plutonism and mineralization in the Boulder Batholith region, Montana: Economic Geology, v. 97, p. 241–267.

Lund, K., McAleer, R.J., Aleinikoff, J.N., Cosca, M.A., and Kunk, M.J. 2018, Two-event lode-ore deposition at Butte, USA: $^{40}Ar/^{39}Ar$ and U-Pb documentation of Ag-Au-polymetallic lodes overprinted by younger stockwork Cu-Mo ores and penecontemporaneous Cu lodes: Ore Geology Reviews, v. 102, p. 666–700.

Lyden, C.J., 2013, Gold placers of Montana: Montana Bureau of Mines and Geology Reprint 6, p. 34.

Lyons, T.W., Luepke, J.J., Madeline, E.S., and Zieg, G.A., 2000, Sulfur geochemical constraints on Mesoproterozoic restricted marine deposition: Lower Belt Supergroup, northwestern United States: Geochimica et Cosmochimica Acta, v. 64, p. 427–437.

Madubuike, C., Brikowski, T., and Moulding, A., 2016, Using infrared spectrometry to deduce fluid history from an exploration core, Emigrant Peak geothermal prospect, northern Fish Lake Valley, Nevada, USA: Geothermal Resources Council Transactions, v. 40, p. 445–454.

Mahoney, J.B., Pignotta, G.S., Ihinger, P.D., Wittkop, C., Balgord, E.A., Potter, J.J., and Leistikow, A., 2015, Geologic relationships in the northern Helena salient, Montana: Geology of the Elliston region: Northwest Geology, v. 44, p. 109–135.

Martin, M., Dilles, J., and Proffett, J.M., 1999, U-Pb geochronologic constraints for the Butte porphyry system [Abs.]: Geological Society of America Abstracts with Programs, v. 31, no. 7, p. A380.

Matthews, A., and Beckinsale, R.D., 1979, Oxygen isotope equilibration systematics between quartz and water: American Mineralogists, v. 64, p. 232–240.

Monecke, T., Monecke, J., Reynolds, T.J., Tsuruoka, S., Bennett, M.N., Skewes, W.B., and Palin, R.M., 2018, Quartz solubility in the H_2O-NaCl system: A framework for understanding vein formation in porphyry copper deposits: Economic Geology, v. 113, p. 1007–1046.

Mosier, D.L., Sato, T., Page, N.J., Singer, D.A., and Berger, B.R., 1987, Descriptive model of Creede epithermal veins, *in* Cox, D.P. and Singer, D.A., eds., Mineral deposit models: U.S. Geological Survey Bulletin 1693, p. 145–149.

Noll, P.D. Jr., Newsom, H.E., Leeman, W.P., and Ryan, J.G., 1996, The role of hydrothermal fluids in the production of subduction zone magmas: Evidence from sidophile and chalcophile trace elements and boron: Geochimica et Cosmochimica Acta, v. 60, p. 587–611.

Ohmoto, Hiroshi, 1986, Stable isotope geochemistry of ore deposits, *in* Valley, J.W., Taylor, H.P. Jr., and O'Neil, J.R., eds., Stable isotopes in high temperature geologic processes: Mineralogical Society of America Reviews in Mineralogy, v. 16, p. 491–559.

Ohmoto, H., and Rye, R.O., 1979, Isotopes of sulfur and carbon, *in* Barnes, H.L., ed.: Geochemistry of hydrothermal ore deposits: Hoboken, N.J., Wiley and Sons, 2nd ed., p. 509–567.

Olson, N.H., Dilles, J.H., Kallio, I.M., Horton, T.R., and Scarberry, K.C., 2016, Geologic map of the Ratio Mountain 7.5' quadrangle, southwest Montana: Montana Bureau of Mines and Geology EDMAP 10, scale 1:24,000.

Olson, N.H., Sepp, M.D., Mankins, N.E., Blessing, J.M., Dilles, J.H., and Scarberry, K.C., 2017, Geologic map of the Mount Thompson 7.5' quadrangle, southwest Montana: Montana Bureau of Mines and Geology EDMAP 11, 13 p., 11 sheets, scale 1:24,000.

Pinckney, D.M., and Becraft, G.E., 1961, Preliminary geologic map of the southwest quarter of the Boulder quadrangle, Montana: U.S. Geological Survey Mineral Investigations Field Studies Map MF-187, scale 1:24000.

Reed, M.H., and Palandri, J., 2006, Sulfide mineral precipitation from hydrothermal fluids, *in* Vaughan, D.J., ed., Sulfide mineralogy and geochemistry: Mineralogical Society of America Reviews in Mineralogy and Geochemistry, v. 61, p. 609–631.

Reed, M., Rusk, B., and Palandri, J., 2013, The Butte magmatic-hydrothermal system: One fluid yields all alteration and veins: Economic Geology, v. 108, p. 1379–1396.

Reyes, A.G., 1990, Petrology of Philippine geothermal systems and the application of alteration mineralogy to their assessment: Journal of Volcanology and Geothermal Research, v. 43 p. 279–309.

Ridge, J.D., 1972, Classification of ore deposits, *in* Ridge, J.D., ed., Annotated bibliographies of mineral deposits in the western hemisphere: Geological Society of America Memoir 131, p. 673–678.

Roby, R.N., Ackerman, W.C., Fulkerson, F.B., and Crowley, F.A., 1960, Mines and mineral deposits (except fuels), Jefferson County, Montana: Montana Bureau of Mines and Geology Bulletin 16, p. 37–38.

Roedder, Edwin, 1984, Fluid inclusions: Mineralogical Society of America Reviews in Mineralogy, v. 12, 646 p.

Rottier, B., Kouzmanov, K., Casanova, V., Wälle, M., and Fontboté, L., 2018, Cyclic dilution of magmatic metal-rich hypersaline fluids by magmatic low salinity fluid: Generating the giant epithermal polymetallic deposit of Cerro de Pasco, Peru: Economic Geology, v. 113, p. 825–856.

Rusk, B.G., Reed, M.H., and Dilles, J.H., 2008, Fluid inclusion evidence for magmatic-hydrothermal fluid evolution in the porphyry copper-molybdenum deposit at Butte, Montana: Economic Geology, v. 103, p. 307–334.

Rutland, C., Smedes, H., Tilling, R., and Greenwood, W., 1989, Volcanism and plutonism at shallow crustal levels: The Elkhorn Mountains Volcanics and the Boulder Batholith, southwestern Montana, *in* Henshaw, P., ed., Volcanism and plutonism of western North America: Volume 2, Cordilleran volcanism, plutonism, and magma generation at various crustal levels, Montana and Idaho, Field trips for the 28th International Geological Congress: American Geophysical Union, Monograph, p. 16–31.

Rye, R.O., Whelan J.E., Harrison, J.E., and Hayes, T.S., 1984, The origin of copper-silver mineralization in the Ravalli group as indicated by preliminary stable isotope studies, *in* Hobbs, S.W., The belt abstracts with summaries, Belt Symposium II, 1983: Montana Bureau of Mines and Geology Special Publication 90, p. 104–107.

Scarberry, K.C., 2016, Geologic map of the Sugarloaf Mountain 7.5' quadrangle, Deer Lodge, Jefferson, and Powell Counties, Montana: Montana Bureau of Mines and Geology Open-File Report 674, scale 1:24,000.

Scarberry, K.C., Korzeb, S.L., and Smith, M.G., 2015, Origin of Eocene volcanic rocks at the south end of the Deer Lodge Valley, Montana, *in* Mosolf, J., and McDonald, C., eds.: 40th annual field conference Geology of the Elliston area, Montana and other papers: Northwest Geology, v. 44, p. 201–212.

Scarberry, K.C., Coppage, E.L., and English, A.R., 2019a, Field guide to the geology and metallic mineral deposits along the western contact between the Boulder Batholith and the lower and middle members of the Elkhorn Mountains Volcanic field: Northwest Geology, v. 48, p. 61–70.

Scarberry, K.C., Gammons, C.H., and Kallio, I.M., 2019b, Field guide to the geology and metallic mineral deposits along the eastern contact between the Boulder Batholith, the Elkhorn Mountains Volcanic field, and Cretaceous-Paleozoic sedimentary rocks: Northwest Geology, v. 48, p. 97–108.

Scarberry, K.C., Elliott, C.G., and Yakovlev, P.V., 2019c, Geologic summary of the Butte North 30' x 60' quadrangle, southwestern Montana: Northwest Geology, v. 48, p. 1–14.

Scarberry, K.C., Elliott, C.G., and Yakovlev, P.V., 2019d, Geology of the Butte North 30' x 60' quadrangle, southwest Montana: Montana Bureau of Mines and Geology Open-File Report 715, 30 p., scale 1:100,000.

Shankar, Vikram, 2015, Field characterization by near infrared (NIR) mineral identifiers—A new pros-

pecting approach: Procedia Earth and Planetary Science, v. 11, p. 198–203.

Silberman, M.L., and Berger, B.R., 1985, Relationship of trace-element patterns to alteration and morphology in epithermal precious-metal deposits, *in* Berger, B.R., and Bethke, P.M., eds., Geology and geochemistry of epithermal systems: Reviews in Economic Geology, v. 2, p. 203–232.

Sillitoe, R.H., 2010, Porphyry copper systems: Economic Geology, v. 105, p. 3–41.

Sillitoe, R.H., Grauberger, G.L., and Elliott, J.E., 1985, A diatreme-hosted gold deposit at Montana Tunnels, Montana: Economic Geology, v. 80, p. 1707—-1721.

Simmons, S.F., and Browne, P.R.L., 2000, Hydrothermal minerals and precious metals in the Broadlands-Ohaaki geothermal system: Implications for understanding low-sulfidation epithermal environments: Economic Geology, v. 95, p. 971–999.

Simmons, S.F., White, N.C., and John, D.A., 2005, Geologic characteristics of epithermal precious and base metal deposits, *in* Hedenquist, J.W., Thompson, J.F.H., Goldfarb, R.J., and Richards, J.P. eds., Economic Geology One Hundredth Anniversary Volume 1905–2005: Society of Economic Geologists, p. 485–522.

Simmons, S.F., Brown, K.F., and Tutolo, B.M., 2016, Hydrothermal transport of Ag, Au, Cu, Pb, Te, Zn, and other metals and metalloids in New Zealand geothermal systems: Spatial patterns, fluid-mineral equilibria, and implications for epithermal mineralization: Economic Geology, v. 111, p. 589–618.

Slack, J.F., 1993, Models of tourmalinite formation in the Middle Proterozoic Belt and Purcell supergroups (Rocky Mountains) and their exploration significance, in Current Research, Part E: Geological Survey of Canada Paper 93-1E, p. 33–40.

Smedes, H.W., 1966, Geology and igneous petrology of the Northern Elkhorn Mountains, Jefferson and Broadwater Counties, Montana: U.S. Geological Survey Professional Paper 510, 82 p., scale 1:48,000.

Sterner, M.S., Hall, D.L., and Bodnar, R.J., 1988, Synthetic fluid inclusions. V. Solubility relations in the system NaCl-KCl-H_2O under vapor-saturated conditions: Geochimica et Cosmochimica Acta v. 52, p. 989–1005.

Strauss, H., and Schieber, J., 1990, A sulfur isotope study of pyrite genesis: The mid-Proterozoic Newland Formation, Belt Supergroup, Montana: Geochimica et Cosmochimica Acta, v. 54, p. 197–204.

Weissberg, B.G., 1969, Gold-silver ore grade precipitates from New Zealand thermal waters: Economic Geology, v. 64, p. 95–108.

Yang, K., Brown, P.R.L., Huntington, J.F., and Walshe, J.L., 2001, Characterising the hydrothermal alteration of the Broadlands-Ohaaki geothermal system, New Zealand, using short-wave infrared spectroscopy: Journal of Volcanology and Geothermal Research, v. 106, p. 53–65.

APPENDIX A

Appendix A

Terraspec Halo VNIR-SWIR analytical results for argillic-illite altered rocks.

Sample	Mineral	ISM	Al-OH	Mg-OH	Al-Fe-Mg	Fe3i	Fe3T	KX	Fe-OH
BF-1	K-illite	3.912	2209.0	2349.3	2209.0				
	phengite	2.407	2210.0	2349.3	2210.0				
	beidellite	3.742	2210.6	2350.3	2210.6				
	ferrihydrite	3.333	2210.9	2350.0	2210.9				
		3.564	2210.3	2349.7	2210.3				
BF-2	K-illite	1.084	2208.0	2351.4	2208.0			1.32	
	Illite/smectite	1.815	2211.7	2348.9	2211.6				
	phengite	2.065	2212.5	2351.2	2212.5				
	jarosite	2.045	2211.4	2349.8	2211.2	1.154	902.6		
	kaolinite PX	2.957	2209.9	2349.4	2209.9	1.262	908.2		
		3.575	2210.1			1.226	889.4		
		2.438	2211.2	2350.7	2211.2	1.132	892.4		
BF-3	K-illite	2.473	2208.0	2350.0	2208.0	1.437			
	kaolinite WX	2.080	2207.7	2350.0	2207.7			1.071	
	dickite	1.586	2207.7	2350.0	2207.7				
	jarosite	2.408	2208.4	2349.3	2208.4				
		1.485	2208.9	2350.3	2208.9				
		1.440	2208.9	2351.3	2208.9	1.091	903.8		
		1.551	2209.0	2349.9	2209.0				
		1.399	2208.9	2351.3	2208.9		904.2		
BF-4	K-illite	3.225	2211.8						
	phengite	3.269	2210.5						
	pyrophyllite	1.475	2211.5	2350.0	2211.5				
		3.281	2210.4						
BF-5	K-illite	1.150	2211.2	2348.9	2211.2				
	illite/smectite	1.300	2211.9	2350.1	2211.9				
BF-9	K-illite	1.038	2211.0	2348.4	2211.0				
	ferrihydrite	1.044	2211.5	2349.2	2211.5				
	phengite	1.349	2210.9	2346.1	2208.0				
	illite/smectite								
	playgorskite								
BF-10	phengite	2.399	2208.5	2351.3	2208.5				2245.3
	tourmaline	2.748							
	roscoelite	2.441	2208.7	2356.6	2208.7				
	vermiculite	1.928						1.014	
	K-illite	1.052							
	ferrihydrite	2.569	2208.9		2208.9				
	Mg-illite	3.918	2210.9	2349.9		1.561	915.7		
	kaoliniteWX	1.191	2212.5	2350.6	2212.5				
	beidellite	3.179	2210.8						
	glaucophane	1.351	2212.9	2348.9	2212.9				
	rectorite	1.074	2208.4	2351.4	2208.4				2246.5
BF-11	K-illite	2.244	2208.8	2349.5	2208.8			1.051	
	kaoliniteWX	1.398	2210.2	2351.5	2210.2	1.367	966.2		
	jarosite	1.026	2210.3	2350.9	2210.3	1.442	966.9		
	magnesite	2.248	2209.1	2349.6	2209.1				
	muscovite								
	ferrihydrite								
BF-16	kaoliniteWX	1.384	2208.0	2382.6	2208.0	1.486		0.971	
	palygorskite	1.458	2207.9		2207.9			0.974	
	muscovite	1.379	2208.3	2382.4	2208.3	1.486		0.942	
	K-illite								
	Illite/smectite								
	montmorillonite								

Sample	Mineral	ISM	Al-OH	Mg-OH	Al-Fe-Mg	Fe3i	Fe3T	KX	Fe-OH
BF-17	K-illite	1.450	2207.8	2350.5	2207.8			1.450	
	muscovite	1.379	2207.5	2349.9	2207.5				
	dickite	1.589	2207.7	2351.9	2207.7				
	halloysite								
	kaolinite WX								
	ferrihydrite								
BF-19	K-illite	1.098	2201.6	2321.7	2201.6	1.385	905.9		
	illite/smectite	1.505	2211.6	2349.1	2211.6	1.932	929.7		
	goethite	1.174	2211.1	2349.6	2211.1	1.507	964.3		
	palygorskite	1.510	2210.5	2348.3	2210.5	2.024	921.1		
	kaolinite PX	1.597	2211.5	2349.7	2211.5	2.255	921.2		
		1.289	2211.3	2349.2	2211.3	1.498	924.8		
BF-22	K-illite	2.492	2208.6	2349.1	2208.6	1.127	920.0		
	jarosite	0.998	2212.0	2347.7	2212.0				
	goethite	3.365	2209.8	2349.3	2209.8	1.369	886.6		
	nontronite	2.870	2208.9	2348.9	2208.9	1.328			
	ferrihydrite	1.751	2208.4	2348.5	2208.4	1.250	917.3		
		1.527	2208.3	2347.2	2208.3	1.366			
BF-23	K-illite	1.092	2212.5	2347.3	2212.5	1.466	961.9		
	nontronite	1.006	2212.9	2346.7	2212.9	1.770	962.9		
	ferrihydrite	1.081	2212.9	2348.5	2212.9				
BF-24	muscovite	2.074	2208.8	2349.3	2208.8	1.696	924.1		
	jarosite	1.640	2208.8	2349.8	2208.8	1.560	918.3		
	goethite	2.522	2208.7	2351.6	2208.7	2.266	919.5		
	ferrihydrite								
BF-25	K-illite	1.727	2208.0	2349.9	2208.0				
	Mg-illite	1.310	2210.4	2358.1	2210.4				2247.3
	tourmaline	1.729	2209.7		2209.7	1.001			
	goethite	2.097	2207.4	2349.7	2207.4				
	phengite	1.450	2207.6	2349.7	2207.6				
	Fe-smectite	1.584	2209.6	2351.8	2209.6				
	ferrihydrite	1.037	2210.2	2351.0	2210.2	1.652			
	beidellite	1.497	2210.3	2350.1	2210.3				
		3.220	2211.3	2349.5	2211.3	1.366	892.8		
		1.335	2211.6	2350.9	2211.6				
		2.712	2211.5		2211.5				
BF-42	K-illite	1.212	2208.1	2349.5	2208.1	1.248	923.8		
	goethite	1.026	2208.2	2351.4	2208.2	1.108	964.3		
		0.878	2208.2	2351.0	2208.2	1.314	964.0		
		1.198	2208.2	2353.1	2208.2	1.524	999.2		
		1.202	2208.3	2352.8	2208.3	1.467	964.6		
		1.382	2208.1	2352.0	2208.1	1.419			
BF-47	Mg-illite	3.205	2207.4						
	K-illite	2.372	2207.2	2349.2	2207.2				
	phengite	3.482	2207.0	2349.3	2207.0				
	muscovite								
	rectorite								
BF-48	phengite	3.332	2207.8	2349.8	2207.8				
	rectorite	2.447	2208.1	2348.8	2206.3				
	Illite/smectite	2.533	2207.2		2207.2				
	K-illite	2.051	2206.3		2207.6				
	hydrobiotite	1.562							
	magnesite	1.268							
	muscovite	3.397	2208.1		2208.1				
	glaucphane	1.836	2204.7	2346.9	2204.7				
	Mg-illite								

Sample	Mineral	ISM	Al-OH	Mg-OH	Al-Fe-Mg	Fe3i	Fe3T	KX	Fe-OH
BF-52	tourmaline	1.022	2209.1	2357.5	2209.1				2246.5
	K-illite		2208.8		2347.4				2347.4
	ankerite								
	Mg-illite								
BF-53	Mg-illite	1.283	2214.3	2348.4	2214.3				
	muscovite	1.297	2208.4	2355.3	2208.4			0.994	
	halloysite	1.092	2208.6	2353.9	2208.6			0.993	
	K-illite	1.286	2208.5	2354.6	2208.5			0.993	
	palygorskite								
BF-54	K-illite	1.515	2213.0	2351.3	2213.0				
	tourmaline	1.135	2211.4	2353.6	2211.4				2246.9
	phengite	1.207	2212.0	2350.5	2212.0				
	Mg-illite	2.054	2208.5	2350.3	2208.5				
	ferrihydrite	1.933	2208.2	2314.6	2208.2				
Sample	Mineral	ISM	Al-OH	Mg-OH	Al-Fe-Mg	Fe3i	Fe3T	KX	Fe-OH
BF-55	Mg-illite	1.391	2211.8	2349.7	2211.8				
	muscovite	2.002	2212.9						
	phengite	1.103	2213.0	2340.7	2340.7				
	montmorillonite	0.849	2211.2	2347.1	2211.2				
	ankerite	1.023	2212.4	2339.5	2339.5				
BF-58	tourmaline		2207.9	2366.2	2246.3				2246.3
	goethite		2208.0	2365.7	2208.0	0.986			2246.9
	vermiculite		2207.4		2207.4				2246.5
BF-59	dickite	1.097	2207.4		2207.4	1.271	966.4		
	goethite	1.371	2207.8	2352.5	2207.8	1.511	965.3	1.079	
	montmorillonite								
	halloysite								
	muscovite								
	ferrihydrite								
BF-60	chabazite		2207.1		2207.1	1.094			
	goethite		2207.5	2374.8	2207.5	1.212	992.3		
	Fe-saponite		2206.4	2372.0	2206.4	1.177			
BF-61	tourmaline	2.203	2208.7	2358.0	2208.7				2245.7
	halloysite		2208.6		2208.6				2247.0
			2208.7		2208.7				2245.5
			2208.3	2363.9	2246.2				2246.2
			2208.6		2247.2				2247.2
BF-62	tourmaline	2.155	2207.6	2363.8	2246.5				2246.5
	vermiculite								
	roscoelite								
BF-63	goethite	1.118	2208.3	2354.0	2208.3	1.383	994.3	1.005	
	halloysite	0.836	2208.3			1.301		1.004	
			2208.2	2356.0	2208.2	1.320			
BF-64	tourmaline		2207.9	2364.5	2246.8				2246.8
	chabazite		2208.6	2362.7	2246.2				2246.2
	vermiculite		2207.8		2296.4				2296.4
	saponite								
BF-65	goethite	0.849	2208.5	2316.3	2208.5	1.335	949.1	0.972	
	K-illite	1.630	2208.4	2315.1	2208.4	1.451	965.4	0.961	
	kaolinite PX	1.040	2208.9	2354.1	2208.9	1.525	937.9	1.006	
	kaolinite WX								
	hematite								
	ferrihydrite								
BF-66	tourmaline	2.149	2208.2	2364.1	2246.3	1.229			2246.3
	goethite	2.535	2208.3		2246.6				2246.6
	roscoelite		2208.2	2364.7	2246.6	1.155			2246.6
	vermiculite		2207.8	2367.7	2247.4	1.088			2247.4

Sample	Mineral	ISM	Al-OH	Mg-OH	Al-Fe-Mg	Fe3i	Fe3T	KX	Fe-OH
	chabazite								
	jarosite								
	magnesite								
BF-67	chabazite		2208.3			1.262			
	tourmaline		2208.3			1.114			
	goethite		2208.4			1.105			
	montmorillonite		2207.9	2365.0	2247.2				2247.2
BF-68	chabazite		2207.5	2371.1	2207.5				2247.2
	tourmaline		2207.6	2370.4	2246.9				2246.9
	goethite			2310.6	2206.9	1.215			2309.3
					2204.9	1.297			2299.2
BF-69	chabazite		2207.4	2371.0	2247.5				2247.5
	tourmaline								
BF-70	jarosite		2208.1			1.144	964.8	0.927	
	Kaolinite WX								

Terraspec Halo VNIR-SWIR analytical results for unaltered aplite

Sample	Mineral	ISM	Al-OH	Mg-OH	Al-Fe-Mg	Fe3i	Fe3T	KX	Fe-OH
BF-28	phillipsite-Ca		2207.3		2207.3				2296.0
	tourmaline		2202.3	2315.1	2162.5				2296.9
	Fe-smectite								

Terraspec Halo VNIR-SWIR analytical results for unaltered granite

Sample	Mineral	ISM	Al-OH	Mg-OH	Al-Fe-Mg	Fe3i	Fe3T	KX	Fe-OH
BF-33	K-illite	0.191	2207.4	2341.5	2341.5			0.717	
	stilpnomelane	0.228	2207.5	2341.6	2341.6			0.603	
		0.352	2206.6	2332.2	2332.2			1.131	
		0.212	2207.7	2339.9	2339.9				
BF-43	clinoptilolite	0.254	2204.6	2337.7	2337.7				
	montmorillonite	0.162	2203.6	2334.2	2334.2				
	rectorite		2206.9	2341.8	2206.9				
BF-44	halloysite	1.009	2208.1	2352.2	2208.1	1.117			
	goethite	0.991	2207.9	2354.2	2207.9	1.255	964.9		
	ferrihydrite	1.014	2208.3	2354.9	2208.3				
BF-45	K-illite	0.821	2204.6	2345.6	2204.6				
	muscovite	0.637	2205.0	2346.0	2205.0				
	montmorillonite		2204.9	2326.4	2326.4			0.590	
BF-57	K-illite	0.317	2204.1	2329.0	2329.0				
	Mg-illite	0.327	2205.7	2331.9	2331.9				
	phengite	0.347	2202.0	2341.8	2341.8				
	stilpnomelane	0.454	2206.8	2342.1	2342.1				
	epidote	0.276							
	Fe-saponite	0.166							
	clinozoisite	0.314							
	rectorite	0.558	2201.8	2342.0	2342.0				
	montmorillonite								
	vermiculite								

Terraspec Halo VNIR-SWIR analytical results for propylitic alteration

Sample	Mineral	ISM	Al-OH	Mg-OH	Al-Fe-Mg	Fe3i	Fe3T	KX	Fe-OH
BF-49	phengite	3.094	2208.1	2346.4	2208.1			1.038	
	kaoliniteWX	2.932	2208.6		2208.6			0.947	2246.7
	tourmaline	2.139	2206.1		2206.1			1.018	
	halloysite	2.060	2208.4	2381.8	2208.4				

Sample	Mineral	ISM	Al-OH	Mg-OH	Al-Fe-Mg	Fe3i	Fe3T	KX	Fe-OH
	K-illite	3.819							
	muscovite								
BF-51	K-illite	1.830	2208.2	2347.9	2208.2				
	muscovite	1.782	2208.4		2208.4				
	phengite	1.866	2207.0	2346.3	2207.0				
	ankerite	1.784	2207.4	2346.4	2207.4				
		1.901	2207.5	2345.1	2207.5				
		1.488							
		1.441							
BF-56	K-illite	2.040	2208.2	2344.5	2208.2				
	muscovite	1.083	2208.1	2345.8	2208.1				
	ankerite	2.191							
	phengite	0.759							
	kaolinitePX	2.310							
	hydrobiotite	1.353							
	rectorite	1.583							
	Mg-illite	2.044	2208.5	2345.8	2208.5			1.044	
	dolomite	1.067							

Terraspec Halo VNIR-SWIR analytical results for carbonate alteration

Sample	Mineral	ISM	Al-OH	Mg-OH	Al-Fe-Mg	Fe3i	Fe3T	KX	Fe-OH
BF-34	calcite	1.638	2208.1	2331.0	2208.1			0.987	
	kaoliniteWX	2.523	2208.2		2208.2			0.995	
	kaolinitePX								
	Mg-illite								
	smithsonite								
	hematite								
BF-35	clinozoisite	2.815	2207.3	2342.7	2343.0				
	epidote	2.326	2206.9	2343.0	2342.8				
	muscovite	2.838	2208.7	2344.4	2344.4				
	K-illite								
	dolomite								
	montmorillonite								
	phlogopite								

APPENDIX B

Appendix B

Terraspec Halo VNIR-SWIR analytical results for quartz veins and silicic-illite alteration. ISM, illite spectral maturity scaler; CSM, chlorite spectral maturity scaler.

Sample	Mineral	ISM	Al-OH	Mg-OH	Al-Fe-Mg	Fe3i	Fe3T	CSM	Fe-OH
BF-1	illite/smectite	0.538	2208.7	2344.9	2208.7				
	K-illite	0.710	2213.9	2351.0	2213.9				
BF-2	illite/smectite	0.659	2211.6	2344.7	2211.6				
	K-illite	0.688	2210.3	2351.2	2210.3				
	muscovite	0.488	2208.6						
	jarosite	0.733	2208.3	2349.7	2208.3				
		0.506	2209.5	2347.4	2209.5				
		0.371	2209.7		2209.7				
		0.874	2210.1	2349.4	2210.1				
BF-4	K-illite	0.882	2212.6	2345.5	2212.6				
	jarosite	0.838	2209.5	2340.6	2209.5				
	illite/smectite	0.976	2212.1	2344.5	2212.1				
	chabazite	0.674	2208.0	2343.3	2208.0				
		0.703	2212.0	2342.7	2212.0				
		0.937	2211.1	2348.1	2211.1				
		0.357	2197.9	2322.9	2197.9				
		0.386	2198.1	2342.1	2198.1				
BF-5	illite/smectite	0.897	2210.4	2348.9	2210.4				
	K-illite	0.489	2210.6	2342.9					
BF-7	jarosite	0.369	2208.8	2342,9	2208.8	0.916			
	K-illite	0.360	2204.5	2340.0	2204.5	0.924	997.1		
	chabazite	0.355	2204.1	2318.4	2204.1				
			2205.2	2205.2	2205.2				
BF-8	Illite/smectite	0.302	2201.0	2354.9	2201.0				
	K-illite	0.240	2198.9	2337.8	2198.9				
	chabazite	0.193	2205.8	2347.8	2205.8				
	gmelinite-Na	0.701	2208.4	2349.7	2208.4				
	ferrihydrite		2197.6	2377.1					
BF-9	K-illite	0.234	2207.7		2254.2	2.049	919.7		
	chabazite	0.296	2209.1			1.861	934.6		
	harmotome	0.871	2208.0	2345.4					
	goethite								
	illite/smectite								
	magnesite								
BF-11	K-illite	0.788	2209.8	2348.7	2209.8				
BF-19	illite/smectite	0.575	2209.8			1.459	931.2		
	goethite	0.545	2208.5			1.368	938.8		
	Mg-illite	0.569	2208.8	2350.7	2208.8	1.388	931.6		
	ferrihydrite	0.833	2212.0	2343.5	2212.0	1.514	934.7		
		0.895	2215.2			1.733	920.8		
			2202.6						
BF-20	K-illite	0.430	2211.0		2211.0	1.542	953.7		
	Mg-illite	0.580	2210.6	2351.1	2210.6	1.442	959.0		
	muscovite	0.512	2209.5	2348.2	2209.5	1.538	944.3		
	gmelinite-Na	0.613	2210.2	2348.8	2210.2				
	montmorillonite	0.524	2211.6	2349.4	2211.6	1.784	943.2		
	goethite	0.679	2209.8	2353.0	2209.8	1.528	962.4		
	hematite	0.735	2210.7	2350.1	2210.7	1.833	949.0		
	ferrihydrite	0.882	2208.5	2351.1	2208.5	1.505	959.4		
	nontronite	0.572	2210.7	2350.1	2210.7				
		0.661	2210.4	2351.9	2210.4	1.576	960.8		

Sample	Mineral	ISM	Al-OH	Mg-OH	Al-Fe-Mg	Fe3i	Fe3T	CSM	Fe-OH
			2211.7			1.250	967.5		
			2212.2			1.409	949.6		
			2211.3		2297.1	1.403	949.7		
BF-23	jarosite	0.629	2208.3		2208.3	1.300	924.8		
			2210.3			1.368	923.7		
BF-25	K-illite	0.212	2203.1	2349.4	2203.1				
	illite/smectite	0.588	2209.3			1.590			
	gmelinite-Na	0.352	2207.7	2316.9	2316.9				
	phengite	0.334	2208.7	2315.3	2315.3				
	montmorillonite	0.668	2208.8	2348.7	2208.8				
	ferrihydrite	0.839	2210.2	2349.9	2210.2	1.547			
BF-26	K-illite	0.301	2206.3		2206.3				
	Mg-illite	0.556	2207.1	2351.7	2207.1				
	gmelinite-Na	0.966	2208.6	2353.7	2208.6				
	chabazite		2200.2	2350.3		1.024			
	montmorillonite								
	jarosite								
BF-27	K-illite	0.567	2207.9	2349.9	2207.9				
	Mg-illite	0.476	2207.6	2349.0	2207.6				
	illite/smectite	0.456	2207.8	2349.0	2207.8				
	muscovite	0.403	2208.0	2352.0	2208.0				
	ferrihydrite	0.587	2208.1	2348.5	2208.1	1.425	910.7		
		0.550	2208.6	2349.4	2208.6				
		0.593	2208.1	2343.0	2208.1				
		0.923	2206.5	2357.2	2206.5				
BF-29	illite/smectite	0.399	2208.7	2348.9	2208.7	1.195	908.8		
	gmelinite-Na	0.403	2209.1			1.277	911.5		2255.3
	goethite	0.454	2208.4	2349.4	2208.4				
	chlorite								
BF-38	K-illite	0.516	2208.1	2344.8	2208.1	1.207	912.7		
	illite/smectite	0.483	2208.7	2344.0	2208.7				
	goethite	0.569	2208.7	2348.8	2208.7				
	chabazite	0.827	2208.3	2208.3	2208.3				
	tourmaline	0.355	2207.8	2207.8	2207.8				
			2207.9	2383.3	2207.9				
			2207.6	2351.7					2247.8
BF-40	chabazite		2194.4		2161.0				
	montmorillonite		2194.0						
	saponite		2189.2						
			2189.9						
			2194.8						
BF-46	chabazite	0.481	2193.7		2193.7				
	K-illite	0.187	2196.8	2350.9	2196.8				
	Gmelinite-Na	0.179	2195.9						
	illite/smectite	0.186	2198.1	2350.8	2198.1				
	rectorite		2195.5						
	montmorillonite		2193.1		2193.1				
			2197.8	2315.8	2197.8				
BF-48	illite/smectite	0.427	2205.8	2346.9	2205.8				
	K-illite	0.788	2204.4	2349.3	2204.4				
	muscovite	0.801	2205.3	2348.1	2205.3				
	chabazite	0.526	2206.8	2350.1	2206.8				
	vermiculite	0.619	2207.8	2349.8	2207.8				
	Mg-illite	0.308	2207.2	2348.8	2207.2				

Sample	Mineral	ISM	Al-OH	Mg-OH	Al-Fe-Mg	Fe3i	Fe3T	CSM	Fe-OH
BF-52	K-illite	0.505	2208.2	2346.4	2346.4				
	Mg-illite	0.623	2208.3	2355.3	2247.6			1.593	2247.6
	ankerite	0.884	2208.4	2358.8	2208.4				
	Fe-Mg chlorite		2208.4		2247.3				2247.3
	tourmaline		2208.7		2247.3			1.943	2247.3
			2209.1	2355.3	2247.6				2247.6
			2208.8		2247.4				2247.4
BF-53	K-illite	0.734	2213.9	2348.8	2213.9				
	Mg-illite	0.876	2213.8	2350.7	2213.8				
	palygorskite	0.519	2213.9	2348.0	2213.9				
	gmelinite-Na	0.217	2213.6	2345.8	2213.6				
	goethite	0.433	2214.0	2345.0	2214.0				
	montmorillonite	0.902	2213.9	2350.4	2213.9				
	illite/smectite	0.359	2212.6	2349.9	2212.6	1.227	999.3		
	ankerite	0.375	2209.4	2346.0	2209.4				
	ferrihydrite	0.365	2209.8	2345.6	2209.8				
	muscovite	0.502	2209.4	2345.5	2209.4				
		0.602	2208.7	2355.2	2208.7				
BF-54	K-illite	0.878	2208.5	2349.3	2208.8				
	Mg-illite	0.595	2208.6	2316.4	2208.6				
Sample	Mineral	ISM	Al-OH	Mg-OH	Al-Fe-Mg	Fe3i	Fe3T	CSM	Fe-OH
	phengite	0.883	2212.8	2351.2	2212.8				
	tourmaline	0.772	2212.3	2350.7	2212.3				
	ankerite	0.807	2211.9	2348.8	2211.9				
		0.719	2211.4	2348.6	2211.4				
		0.796	2212.0	2345.6	2212.0				2245.4
BF-59	dickite	0.678	2207.4		2207.4	1.247	966.5		
	muscovite								
	halloysite								
	montmorillonite								
	goethite								
	ferrihydrite								
BF-64	roscoelite	0.750	2208.7	2361.6	2245.7				2245.7
	tourmaline	0.663	2208.8	2361.0	2246.0				2246.0
	vermiculite	0.602	2208.8	2360.4	2245.7				2245.7

APPENDIX C

Appendix C

Complete ICP-MS analytical results for altered and unaltered granite. Results are in parts per million (ppm), or weight percent (%). BF-28 is unaltered aplite. Analysis conducted by ALS Minerals Inc., ALS analytical code ME-ICP 61 selected for trace element analysis.

Sample No.	Alteration type	Ag ppm	Al ppm	As ppm	Ba ppm	Be ppm	Bi ppm	Ca %	Cd ppm	Co ppm
BF-3	argillic-sericitic	8.2	7.18	3,090	950	0.5	<2	0.20	53.4	7
BF-10	argillic-sericitic	57.0	3.05	1,535	170	0.6	2	0.05	499	8
BF-11	argillic-sericitic	19.8	6.38	3,610	310	0.9	<2	0.05	57.9	5
BF-16	argillic-sericitic	0.6	6.08	39	590	0.5	2	0.05	1.3	1
BF-22	argillic-sericitic	9.1	6.47	1,035	810	0.6	<2	0.05	6.8	3
BF-28	aplite	<0.5	6.16	18	40	3.2	<2	0.54	0.6	2
BF-33	granite	<0.5	7.50	14	870	1.7	<2	2.67	<0.5	9
BF-33a	propylitic	2.9	6.60	9	290	1.0	3	1.22	<0.5	6
BF-34	carbonate	<0.5	1.24	<5	20	<0.5	6	13.00	<0.5	2
BF-35	carbonate	<0.5	6.33	27	30	1.1	10	10.65	<0.5	<1
BF-38	silicic	51.4	0.66	402	20	<0.5	55	0.06	1.1	5
BF-43	granite	<0.5	7.73	7	720	1.5	<2	3.18	<0.5	13
BF-44	granite	2.6	4.43	54	250	<0.5	<2	0.38	1.7	33
BF-48	argillic-sericitic	31.9	7.62	844	580	0.9	<2	0.18	117.5	14
BF-49	propylitic	0.8	5.37	40	470	1.0	<2	2.35	0.6	17
BF-51	propylitic	<0.5	7.23	17	470	1.5	<2	2.92	0.7	11
BF-56	propylitic	9.7	6.34	62	280	1.3	<2	4.68	120.5	11
BF-57	granite	<0.5	7.26	5	620	1.7	<2	2.54	<0.5	11
BF-62	silicic	20.9	2.37	>10,000	10	1.0	38	0.06	<0.5	1
BF-66	argillic-sericitic	39.4	4.70	9,920	330	0.9	7	0.08	0.6	1

Appendix C continued

Sample No.	Alteration type	Cr ppm	Cu ppm	Fe %	Ga ppm	K %	La ppm	Mg %	Mn ppm	Mo ppm
BF-3	argillic-sericitic	22	227	3.61	20	4.28	30	0.57	629	4
BF-10	argillic-sericitic	12	1,340	1.90	10	2.20	10	0.17	241	3
BF-11	argillic-sericitic	22	202	1.65	10	4.18	30	0.33	112	7
BF-16	argillic-sericitic	10	39	0.57	10	4.93	60	0.02	95	1
BF-22	argillic-sericitic	19	60	1.36	10	5.14	30	0.17	82	3
BF-28	aplite	7	16	0.92	10	4.50	30	0.06	234	2
BF-33	granite	22	78	3.88	20	3.04	30	1.33	600	1
BF-33a	propylitic	29	301	2.44	20	2.90	30	0.75	567	3
BF-34	carbonate	16	51	0.70	<10	0.13	20	0.09	2,030	1
BF-35	carbonate	18	7	4.31	30	0.50	20	0.05	1,750	<1
BF-38	silicic	24	429	1.09	<10	0.10	<10	0.08	55	23
BF-43	granite	20	14	3.73	20	3.24	20	1.37	725	8
BF-44	granite	22	54	2.78	10	1.35	30	0.35	893	11
BF-48	argillic-sericitic	22	382	2.43	20	4.65	40	0.28	116	8
BF-49	propylitic	18	14	2.99	10	3.27	20	0.93	908	2
BF-51	propylitic	26	12	3.41	10	4.33	40	1.20	1,375	12
BF-56	propylitic	20	795	4.44	10	3.90	30	1.60	2,390	2
BF-57	granite	25	32	3.04	20	3.27	30	1.07	534	2
BF-62	silicic	26	78	2.41	10	0.03	<10	0.46	133	21
BF-66	argillic-serictic	25	146	3.61	10	2.84	70	0.54	150	15

Appendix C continued

Sample No.	Alteration type	Na %	Ni ppm	P ppm	Pb ppm	S %	Sb ppm	Sc ppm	Sr ppm	Th ppm
BF-3	argillic-sericitic	0.24	9	600	6,170	2.26	21	10	154	<20
BF-10	argillic-sericitic	0.04	3	270	31,600	3.01	130	3	25	<20
BF-11	argillic-sericitic	0.03	2	450	9,890	0.92	92	9	74	<20
BF-16	argillic-sericitic	0.26	3	110	301	0.01	12	2	183	40
BF-22	argillic-sericitic	0.09	2	350	2,790	0.09	20	8	102	<20
BF-28	aplite	2.02	<1	50	105	<0.01	<5	2	28	60
BF-33	granite	1.97	10	870	51	0.08	8	11	538	20
BF-33a	propylitic	0.06	9	720	142	0.12	9	10	102	20
BF-34	carbonate	0.02	<1	280	29	0.01	<5	4	295	<20
BF-35	carbonate	0.02	<1	670	30	<0.01	78	7	2,120	<20
BF-38	silicic	0.05	<1	110	2,940	0.11	43	2	23	<20
BF-43	granite	2.16	11	860	67	0.01	<5	12	497	20
BF-44	granite	1.36	6	510	219	0.19	5	7	79	<20
BF-48	argillic-sericitic	0.06	8	800	26,500	1.83	48	11	51	20
BF-49	propylitic	0.21	7	490	110	1.05	9	6	111	<20
BF-51	propylitic	0.26	10	900	42	0.26	6	12	116	20
BF-56	propylitic	0.03	9	850	3,880	0.65	97	12	172	20
BF-57	granite	2.01	9	650	40	0.01	<5	9	420	20
BF-62	silicic	0.23	1	70	1,620	0.05	23	9	49	<20
BF-66	argillic-serictic	0.29	3	690	2,390	0.32	41	13	97	30

Appendix C continued

Sample No.	Alteration type	Ti %	Tl ppm	U ppm	V ppm	W ppm	Zn ppm
BF-3	argillic-sericitic	0.27	<10	10	86	20	3,490
BF-10	argillic-sericitic	0.09	<10	<10	31	<10	30,800
BF-11	argillic-sericitic	0.27	<10	10	82	10	3,530
BF-16	argillic-sericitic	0.06	<10	<10	23	<10	86
BF-22	argillic-sericitic	0.25	<10	<10	84	10	449
BF-28	aplite	0.07	<10	10	5	<10	38
BF-33	granite	0.36	<10	10	102	<10	54
BF-33a	propylitic	0.30	<10	<10	93	10	54
BF-34	carbonate	0.10	<10	<10	20	<10	14
BF-35	carbonate	0.31	<10	10	134	<10	12
BF-38	silicic	0.02	<10	<10	14	<10	43
BF-43	granite	0.37	<10	<10	108	<10	65
BF-44	granite	0.20	<10	<10	59	<10	72
BF-48	argillic-sericitic	0.27	10	10	101	20	5,620
BF-49	propylitic	0.18	<10	10	42	<10	76
BF-51	propylitic	0.33	<10	<10	98	<10	88
BF-56	propylitic	0.32	<10	<10	83	<10	6,110
BF-57	granite	0.32	<10	<10	86	<10	68
BF-62	silicic	0.03	<10	<10	106	<10	29
BF-66	argillic-serictic	0.35	<10	<10	92	<10	39

APPENDIX D

Appendix D

Trace element results for vein samples analyzed by four acid digestion and ICP-MS and fire assay methods. Analysis conducted by ALS Minerals Inc., analytical code ME-MS 61 selected for trace element analysis and Au-ICP 21 selected for gold analysis.

Sample No.	Mine/Claim/Prospect	Au ppm	Ag ppm	As ppm	Ba ppm	Bi ppm	Cd ppm	Co ppm	Cs ppm	Cu ppm
BF-1	Big Four	4.21	126	>10,000	10	9.88	>1,000	23.9	1.33	1,470
BF-7	Ajax	1.740	638	>10,000	30	480	441	47.9	0.66	5,850
BF-13	Attowa	3.29	61.8	>10,000	190	6.06	304	11.8	15.75	471
BF-15	Blue Jay	0.346	8.33	190.0	50	0.85	4.62	1.7	2.38	33.6
BF-18	Mountain Queen	0.795	73.9	5,980	530	21.6	72.8	16.9	11.65	1,900
BF-23	Mountain Queen	10.40	242	>10,000	40	52.9	123.5	3.5	1.90	1,940
BF-24	Mountain Queen	4.23	159	>10.000	50	8.88	52.8	3.1	1.62	7,050
BF-25	State	14.70	281	519	30	251	0.94	3.1	1.57	2,050
BF-26	State	10.55	198	1,545	10	67.3	4.01	18.0	1.81	8,720
BF-31	Big Major	0.615	135	153.0	30	39.2	2.05	143.0	1.48	20,700
BF-36	State	0.078	15.70	157.5	40	5.34	2.08	1.9	10.45	333
BF-40	State	5.85	57.9	1,240	10	30.4	2.38	295	0.44	2,870
BF-47	Attowa	3.34	547	>10,000	270	198	488	13.0	3.61	4,180
BF-53	St. Anthony	3.29	127	593	180	14.50	>1,000	36.9	1.89	5,650
BF-54	St. Anthony	0.313	45.3	258	40	4.95	737	14.3	2.05	1,900
BF-58	prospect shaft	0.336	60.6	>10,000	10	45.3	3.26	1.7	0.46	155
BF-68	prospect pit	0.432	98	346	1,010	157.5	1.55	4.6	0.44	126
BF-70	prospect pit	0.046	16.30	423	330	18.80	4.67	0.5	2.34	85.4

Sample No.	Mine/Claim/Prospect	Li ppm	Mn ppm	Mo ppm	Pb ppm	Rb ppm	Sb ppm	Sr ppm	Te ppm	Tl ppm
BF-1	Big Four	6.6	153	102.0	64,000	9.2	398	9.1	0.24	1.46
BF-7	Ajax	4.0	25	153.0	179,000	18.4	732	9.0	5.40	0.19
BF-13	Attowa	15.4	80	558	26,700	161.0	311	64.6	0.22	0.91
BF-15	Blue Jay	17.3	125	3.00	499	47.3	27.8	26.2	<0.05	0.28
BF-18	Mountain Queen	24.3	422	6.17	25,800	190.0	64.5	141.0	0.51	1.03
BF-23	Mountain Queen	11.0	35	44.7	78,000	63.8	569	55.5	0.34	0.37
BF-24	Mountain Queen	20.9	48	16.5	61,800	51.1	87.9	62.5	0.69	0.24
BF-25	State	22.5	64	23.9	8,060	49.0	69.8	4.4	1.20	0.22
BF-26	State	36.1	25	43.0	23,500	31.4	655	165.0	0.64	0.16
BF-31	Big Major	5.7	38	35.6	1,220	42.2	12.85	12.8	1.57	0.20
BF-36	State	36.7	67	3.76	2,440	90.0	103.0	27.3	0.10	0.50
BF-40	State	16.2	27	21.5	383	12.1	9.61	1.2	0.87	0.06
BF-47	Attowa	17.2	67	117.5	>200,000	100.5	657	38.0	2.46	0.62
BF-53	St. Anthony	8.0	561	13.40	>200,000	51.8	718	55.8	1.47	0.30
BF-54	St. Anthony	10.9	1,280	4.61	38,300	55.9	513	75.7	0.28	0.30
BF-58	prospect shaft	7.7	38	20.8	2,460	1.9	25.8	15.3	1.48	0.04
BF-68	prospect pit	14.8	44	13.65	291	2.2	37.2	11.9	2.45	0.02
BF-70	prospect pit	19.0	33	5.03	1,075	53.0	45.3	96.5	0.09	0.40

Sample No.	Mine/Claim/Prospect	W ppm	Zn ppm
BF-1	Big Four	0.3	91,200
BF-7	Ajax	4.7	18,850
BF-13	Attowa	65.1	4,300
BF-15	Blue Jay	1.4	152
BF-18	Mountain Queen	17.1	4,300
BF-23	Mountain Queen	14.7	3,570
BF-24	Mountain Queen	3.3	1,920
BF-25	State	2.0	58
BF-26	State	2.7	60
BF-31	Big Major	0.7	70
BF-36	State	14.8	227
BF-40	State	0.3	117
BF-47	Attowa	8.8	20,300
BF-53	St. Anthony	1.0	84,600
BF-54	St. Anthony	1.2	31,400
BF-58	prospect shaft	0.8	199
BF-68	prospect pit	2.3	83
BF-70	prospect pit	15.1	240

Dump samples of vein sections with potential ore grade analysis. Gold and silver ICP-AES and ICP-MS ppm results calculated to troy oz/t. Conversion facture one troy oz/t = 34.3 ppm used in calculations. Ore grade % determined by four acid digestion and ICP-AES methods. AN, anomalous concentration but is not considered to be ore grade.

Sample No.	Mine/Claim/Prospect	Au oz/t	Ag oz/t	Cu %	Pb %	Zn %
BF-1	Big Four	AN	AN	AN	6.4	9.12
BF-7	Ajax	AN	18.6	0.5	17.9	1.88
BF-13	Attowa	AN	AN	AN	2.67	AN
BF-18	Mountain Queen	AN	AN	0.2	2.58	AN
BF-23	Mountain Queen	0.3	7.1	0.2	7.8	AN
BF-24	Mountain Queen	AN	4.6	0.7	6.1	AN
BF-25	State	0.4	8.2	0.2	AN	AN
BF-26	State	0.3	5.8	0.9	2.3	AN
BF-31	Big Major	AN	3.9	2.1	AN	AN
BF-40	State	0.2	AN	0.3	AN	AN
BF-47	Attowa	AN	15.9	0.4	>20	2.03
BF-53	St Anthony	AN	3.7	0.6	>20	8.46
BF-54	St Anthony	AN	AN	AN	3.8	3.14

APPENDIX E

Appendix E

Fluid inclusion data summary, Tm_{halite}, average melting temperature for halite daughter mineral; $Tm_{clathrate}$, average melting temperature for clathrate; Tm_{ice}, average melting temperature for ice; salinity given as wt% NaCl equivalent; Th, vapor to liquid homogenization temperature. Th_{CO2},CO_2 vapor to liquid homogenization temperature. All temperatures given in °C.

Sample No.	Location	Tm_{halite}	Th_{CO2}	$Tm_{clathrate}$	Tm_{ice}	salinity	Th
BF-2	Big Four mine				-0.7	1.2	312.2
BF-2	Big Four mine				-1.5	2.6	314.8
BF-2	Big Four mine				-1.6	2.7	328.5
BF-2	Big Four mine				-1.3	2.2	312.2
BF-2	Big Four mine				-1.6	2.7	297.6
BF-2	Big Four mine				-0.9	1.6	330.5
BF-2	Big Four mine				-0.7	1.2	289.3
BF-2	Big Four mine				-0.7	1.2	297.8
BF-2	Big Four mine				-0.9	1.6	301.7
BF-2	Big Four mine				-0.6	1.1	328.4
BF-2	Big Four mine				-0.5	0.9	299.9
BF-2	Big Four mine				-0.5	0.9	235.4
BF-2	Big Four mine				-0.8	1.4	279.2
BF-2	Big Four mine				-0.9	1.6	237.9
BF-4	Big Four mine				-0.9	1.6	228.9
BF-4	Big Four mine				-1.2	2.1	241.1
BF-4	Big Four mine				-0.3	0.5	245.1
BF-4	Big Four mine				-1.2	2.1	286.9
BF-4	Big Four mine	234.6				33.7	247.4
BF-4	Big Four mine				-0.8	1.4	276.1
BF-4	Big Four mine				-0.2	0.4	317.2
BF-4	Big Four mine				-1.0	1.7	313.9
BF-4	Big Four mine				-0.4	0.7	296.9
BF-4	Big Four mine				-0.8	1.4	301.8
BF-8	Ajax mine				-1.2	2.1	327.8
BF-8	Ajax mine				-1.9	3.2	330.0
BF-8	Ajax mine				-1.4	2.4	328.3
BF-8	Ajax mine				-1.6	2.7	325.8
BF-8	Ajax mine				-1.2	2.1	328.1
BF-8	Ajax mine				-1.1	1.9	295.5
BF-8	Ajax mine				-0.9	1.6	298.5
BF-8	Ajax mine				-1.8	3.1	285.6
BF-8	Ajax mine				-0.8	1.4	329.3
BF-8	Ajax mine				-0.5	0.9	174.6
BF-8	Ajax mine				-0.5	0.9	318.4
BF-8	Ajax mine				-0.4	0.7	327.1
BF-8	Ajax mine				-0.3	0.5	319.5
BF-8	Ajax mine				-0.4	0.7	320.7
BF-8	Ajax mine				-0.8	1.4	309.9
BF-8	Ajax mine				-0.9	1.6	328.7
BF-8	Ajax mine				-1.9	3.2	169.4
BF-8	Ajax mine				-0.8	1.4	326.1
BF-8	Ajax mine				-1.1	1.9	329.1
BF-8	Ajax mine				-0.3	0.5	328.9
BF-8	Ajax mine				-0.8	1.4	279.2
BF-8	Ajax mine				-0.5	0.9	293.8
BF-9	Attowa mine				-1.1	1.9	312.6

Sample No.	Location	Tm_{halite}	Th_{CO2}	$Tm_{clathrate}$	Tm_{ice}	salinity	Th
BF-9	Attowa mine				-0.4	0.7	261.6
BF-9	Attowa mine				-0.9	1.6	278.5
BF-9	Attowa mine				-0.8	1.4	301.5
BF-9	Attowa mine				-0.6	1.1	295.1
BF-9	Attowa mine				-0.4	0.7	257.9
BF-9	Attowa mine		30.2	8.9		1.3	287.2
BF-9	Attowa mine				-0.5	0.9	289.5
BF-9	Attowa mine				-0.9	1.6	298.5
BF-9	Attowa mine				-0.7	1.2	236.3
BF-9	Attowa mine	298.9				38.1	269.5
BF-9	Attowa mine				-1.1	1.9	304.7
BF-9	Attowa mine				-0.5	0.9	246.2
BF-9	Attowa mine				-0.9	1.6	280.1
BF-9	Attowa mine			8.7		1.3	306.9
BF-10	Nickel Plate mine			7.4		1.5	312.3
BF-10	Nickel Plate mine				-3.8	6.1	309.4
BF-10	Nickel Plate mine				-4.1	6.6	300.9
BF-10	Nickel Plate mine				-3.9	6.3	296.7
BF-10	Nickel Plate mine				-3.8	6.1	311.5
BF-10	Nickel Plate mine				-3.2	5.2	347.5
BF-10	Nickel Plate mine				-4.3	6.9	312.6
BF-10	Nickel Plate mine				-4.0	6.4	168.7
BF-15	Blue Jay prospect				-0.4	0.7	242.7
BF-15	Blue Jay prospect				-0.5	0.9	242.9
BF-15	Blue Jay prospect				-1.1	1.9	268.5
BF-15	Blue Jay prospect				-0.9	1.6	241.1
BF-15	Blue Jay prospect				-0.9	1.6	257.7
BF-15	Blue Jay prospect				-0.4	0.7	246.6
BF-15	Blue Jay prospect				-0.6	1.0	284.5
BF-15	Blue Jay prospect				-1.2	2.1	218.9
BF-15	Blue Jay prospect				-0.7	1.2	289.4
BF-15	Blue Jay prospect			7.4		1.5	247.0
BF-15	Blue Jay prospect				-0.9	1.6	255.4
BF-15	Blue Jay prospect				-0.2	0.4	235.7
BF-15	Blue Jay prospect				-0.3	0.5	236.1
BF-15	Blue Jay prospect				-0.4	0.7	235.8
BF-15	Blue Jay prospect				-0.9	1.6	255.4
BF-15	Blue Jay prospect				-0.3	0.5	236.8
BF-15	Blue Jay prospect				-0.4	0.7	246.5
BF-15	Blue Jay prospect				-0.6	1.0	262.1
BF-19	Mountain Queen mine				-0.4	0.7	278.5
BF-19	Mountain Queen mine				-0.2	0.4	272.8
BF-19	Mountain Queen mine				-0.4	0.7	261.1
BF-19	Mountain Queen mine				-0.2	0.4	266.5
BF-19	Mountain Queen mine				-0.9	1.6	296.3
BF-19	Mountain Queen mine				-0.3	0.5	286.9
BF-19	Mountain Queen mine				-0.1	0.2	289.1
BF-19	Mountain Queen mine				-0.3	0.5	289.9
BF-19	Mountain Queen mine				-0.8	1.4	287.4
BF-19	Mountain Queen mine				-0.3	0.5	276.4
BF-19	Mountain Queen mine	209.8				32.4	290.4
BF-19	Mountain Queen mine				-0.9	1.6	308.9
BF-19	Mountain Queen mine				-0.1	0.2	297.2
BF-19	Mountain Queen mine				-0.6	1.0	299.4

Sample No.	Location	Tm_{halite}	Th_{CO2}	$Tm_{clathrate}$	Tm_{ice}	salinity	Th
BF-19	Mountain Queen mine				-0.3	0.5	294.7
BF-19	Mountain Queen mine				-0.5	0.9	315.6
BF-25	State Mine				-4.4	7.0	264.2
BF-25	State Mine				-4.8	7.6	270.3
BF-25	State Mine				-5.2	8.1	267.8
BF-25	State Mine				-4.6	7.3	278.0
BF-25	State Mine				-4.7	7.4	261.7
BF-25	State Mine				-4.1	6.6	250.0
BF-25	State Mine				-4.4	7.0	330.5
BF-25	State Mine						250.0
BF-25	State Mine				-4.3	6.9	297.4
BF-25	State Mine				-4.0	6.4	264.9
BF-25	State Mine				-3.7	6.0	264.8
BF-41	State Mine				-4.9	7.7	255.0
BF-41	State Mine				-4.8	7.6	293.7
BF-41	State Mine				-5.4	8.4	279.2
BF-41	State Mine				-4.9	7.7	257.9
BF-41	State Mine				-5.1	8.0	269.0
BF-41	State Mine				-4.3	6.9	260.0
BF-41	State Mine				-4.5	7.2	272.1
BF-41	State Mine				-5.0	7.9	261.3
BF-41	State Mine				-4.5	7.2	273.8
BF-41	State Mine				-4.0	6.4	281.8
BF-41	State Mine				-4.7	7.4	284.3
BF-41	State Mine				-4.3	6.9	269.6
BF-48	Attowa mine				-1.8	3.1	294.1
BF-48	Attowa mine				-1.3	2.2	245.6
BF-48	Attowa mine				-1.4	2.4	292.8
BF-48	Attowa mine				-1.7	2.9	284.0
BF-48	Attowa mine				-1.1	1.9	227.3
BF-48	Attowa mine				-1.5	2.6	264.2
BF-48	Attowa mine				-1.9	3.2	247.0
BF-48	Attowa mine				-1.4	2.4	239.2
BF-48	Attowa mine			6.9		1.6	294.7
BF-48	Attowa mine				-2.0	3.4	247.9
BF-48	Attowa mine				-2.9	4.8	261.8
BF-48	Attowa mine				-2.3	3.9	247.6
BF-48	Attowa mine				-2.7	4.5	217.4
BF-48	Attowa mine				-2.3	3.9	174.9
BF-48	Attowa mine				-2.4	4.0	157.4
BF-54	St. Anthony mine			8.7		1.3	292.3
BF-54	St. Anthony mine				-0.5	0.9	279.7
BF-54	St. Anthony mine			8.6		1.3	292.3
BF-54	St. Anthony mine			8.1		1.4	294.6
BF-54	St. Anthony mine				-0.6	1.1	309.7
BF-54	St. Anthony mine			8.1		1.4	308.3
BF-54	St. Anthony mine		30.7	9.0		1.3	300.9
BF-54	St. Anthony mine			9.5		1.2	284.8
BF-54	St. Anthony mine				-0.9	1.6	274.7
BF-54	St. Anthony mine				-0.7	1.2	294.3
BF-54	St. Anthony mine				-0.8	1.4	285.4
BF-54	St. Anthony mine	216.1				32.7	307.3
BF-54	St. Anthony mine				-0.9	1.6	292.3

Sample No.	Location	Tm_{halite}	Th_{CO2}	$Tm_{clathrate}$	Tm_{ice}	salinity	Th
BF-54	St. Anthony mine				-0.9	1.6	327.0
BF-54	St. Anthony mine				-1.1	1.9	290.9
BF-63	Whitetail prospect pit				-0.3	0.5	312.9
BF-63	Whitetail prospect pit				-0.9	1.6	253.8
BF-63	Whitetail prospect pit				-0.3	0.5	287.9
BF-63	Whitetail prospect pit				-0.7	1.2	327.8
BF-63	Whitetail prospect pit				-0.6	1.1	172.3
BF-63	Whitetail prospect pit				-0.8	1.4	198.7
BF-63	Whitetail prospect pit				-1.3	2.2	247.6
BF-63	Whitetail prospect pit				-1.4	2.4	169.7
BF-63	Whitetail prospect pit				-1.2	2.1	157.3
BF-63	Whitetail prospect pit				-0.1	0.2	297.0
BF-63	Whitetail prospect pit				-0.3	0.5	337.4
BF-63	Whitetail prospect pit	226.3				33.3	314.0
BF-63	Whitetail prospect pit				-0.6	1.1	337.6
BF-63	Whitetail prospect pit				-0.9	1.6	159.2
BF-63	Whitetail prospect pit				-0.7	1.2	314.7
BF-63	Whitetail prospect pit	216.4				32.7	294.3
BF-63	Whitetail prospect pit	226.5				33.3	307.6
BF-67	Whitetail prospect pit				-1.4	2.4	172.3
BF-67	Whitetail prospect pit				-1.7	2.9	148.9
BF-67	Whitetail prospect pit				-1.9	3.2	159.3
BF-67	Whitetail prospect pit	214.1				32.6	239.4
BF-67	Whitetail prospect pit	229.9				33.5	216.5
BF-67	Whitetail prospect pit				-1.4	2.4	149.1
BF-67	Whitetail prospect pit				-1.1	1.9	172.4
BF-67	Whitetail prospect pit				-1.3	2.2	189.6

APPENDIX F

Appendix F
Summary of sulfur isotope data

Results are reported in standard notation $\delta^{34}S‰$ relative to the Canyon Diablo Troilite standard.

Sample No.	Location	Mineral	Sample Description	$\delta^{34}S‰$
BF-1PY	Big Four mine	pyrite	Massive sulfides with quartz stringers	3.4
BF-1GL	Big Four mine	galena	Massive sulfides with quartz stringers	-0.7
BF-4PY	Big Four mine	pyrite	Silicified granite with disseminated sulfides	2.0
BF-4SP	Big Four mine	sphalerite	Silicified granite with disseminated sulfides	2.2
BF-4GL	Big Four mine	galena	Silicified granite with disseminated sulfides	0.4
BF-7PY	Ajax mine	pyrite	Quartz vein with disseminated sulfides	2.4
BF-7GL	Ajax mine	galena	Quartz vein with disseminated sulfides	1.8
BF-8PY	Ajax mine	pyrite	Quartz vein with disseminated sulfides	3.2
BF-8GL	Ajax mine	galena	Quartz vein with disseminated sulfides	1.4
BF-8CPY	Ajax mine	chalcopyrite	Quartz vein with disseminated sulfides	3.4
BF-9SP	Attowa mine	sphalerite	Quartz vein with disseminated sulfides	3.0
BF-9GL	Attowa mine	galena	Quartz vein with disseminated sulfides	1.9
BF-10GL	Nickel Plate mine	galena	Altered granite with disseminated sulfides	-0.8
BF-10SP	Nickel Plate mine	sphalerite	Altered granite with disseminated sulfides	1.0
BF-11PY	Nickel Plate mine	pyrite	Altered granite with disseminated sulfides	0.7
BF-12GL	Nickel Plate mine	galena	Quartz vein with disseminated sulfides	-0.8
BF-12SP	Nickel Plate mine	sphalerite	Quartz vein with disseminated sulfides	1.5
BF-26PY	State mine	pyrite	Quartz vein with disseminated sulfides	2.8
BF-27CPY	State mine	chalcopyrite	Quartz vein with disseminated sulfides	2.8
BF-31PY	Big Major mine	pyrite	Massive pyrite in altered granite	4.9
BF-39CPY	State mine	pyrite	Quartz vein with disseminated sulfides	2.9
BF-39CPY	State mine	chalcopyrite	Quartz vein with disseminated sulfides	3.1
BF-40PY	State mine	pyrite	Quartz vein with disseminated sulfides	2.6
BF-41PY	State mine	pyrite	Quartz vein with disseminated sulfides	4.7
BF-46PY	State mine	pyrite	Quartz vein with disseminated sulfides	2.4
BF-46GL	State mine	galena	Quartz vein with disseminated sulfides	16.6
BF-47PY	Attowa mine	pyrite	Quartz vein with disseminated sulfides	3.4
BF-47GL	Attowa mine	galena	Quartz vein with disseminated sulfides	1.8
BF-47SP	Attowa mine	sphalerite	Quartz vein with disseminated sulfides	3.4
BF-48PY	Attowa mine	pyrite	Quartz vein with disseminated sulfides	2.8
BF-48GL	Attowa mine	galena	Quartz vein with disseminated sulfides	1.6
BF-48SP	Attowa mine	sphalerite	Quartz vein with disseminated sulfides	3.0
BF-48CPY	Attowa mine	chalcopyrite	Quartz vein with disseminated sulfides	3.1
BF-48-2SP	Attowa mine	sphalerite	Quartz vein with disseminated sulfides	3.4
BF-48-2GL	Attowa mine	galena	Quartz vein with disseminated sulfides	1.9
BF-53PY	St. Anthony mine	pyrite	Quartz vein with disseminated sulfides	5.2
BF-53GL	St. Anthony mine	galena	Quartz vein with disseminated sulfides	3.3
BF-53SP	St. Anthony mine	sphalerite	Quartz vein with disseminated sulfides	4.7
BF-53-2GL	St. Anthony mine	galena	Quartz vein with disseminated sulfides	2.9
BF-53-2SP	St. Anthony mine	sphalerite	Quartz vein with disseminated sulfides	5.0
BF-54PY	St. Anthony mine	pyrite	Quartz vein with disseminated sulfides	4.9

Sample No.	Location	Mineral	Sample Description	$\delta^{34}S‰$
BF-54GL	St. Anthony mine	galena	Quartz vein with disseminated sulfides	2.8
BF-54-2SP	St. Anthony mine	sphalerite	Quartz vein with disseminated sulfides	3.8
BF-54-2PY	St. Anthony mine	pyrite	Quartz vein with disseminated sulfides	4.4
BF-54-2GL	St. Anthony mine	galena	Quartz vein with disseminated sulfides	2.0
BF-55GL	St. Anthony mine	galena	Altered granite with disseminated sulfides	3.6
BF-55SP	St. Anthony mine	sphalerite	Altered granite with disseminated sulfides	4.8
BF-55CPY	St. Anthony mine	chalcopyrite	Altered granite with disseminated sulfides	3.9

APPENDIX G

Appendix G

Isotope equilibrium temperatures calculated from isotope pairs using methods described by Ding and others (2003).

Sample No.	Location	Mineral Pair	$\delta^{34}S‰$	Temperature °C
BF-4	Big Four mine	galena	0.4	382.8
		sphalerite	2.2	
BF-9	Attowa mine	galena	1.9	578.6
		sphalerite	3.0	
BF-10	Nickle Plate mine	galena	-0.8	382.8
		sphalerite	1.0	
BF-12	Nickle Plate mine	galena	-0.8	304.2
		sphalerite	1.5	
BF-47	Attowa mine	galena	1.8	424.6
		sphalerite	3.4	
BF-48	Attowa mine	galena	1.6	475.6
		sphalerite	3.0	
BF-48-2	Attowa mine	galena	1.9	448.7
		sphalerite	3.4	
BF-53	St. Anthony mine	galena	3.3	475.6
		sphalerite	4.7	
BF-53-2	St. Anthony mine	galena	2.9	332.1
		sphalerite	5.0	
BF-54-2	St. Anthony mine	galena	2.0	382.8
		sphalerite	3.8	
BF-55	St. Anthony mine	galena	3.6	539.6
		sphalerite	4.8	